3

Remote Sensing of Evapotranspiration from Cropland

Trent W. Biggs
San Diego State University

George P. Petropoulos
Aberystwyth University

Naga Manohar Velpuri
U.S. Geological Survey

Michael Marshall
World Agroforestry Centre

Edward P. Glenn
University of Arizona

Pamela Nagler
U.S. Geological Survey

Alex Messina
San Diego State University

Acronyms and Definitions

a	Intercept in linear model relating T_R to T_1–T_2 (SEBAL, METRIC)
a_{ds}	Empirical coefficient in downscaling model (Kustas et al., 2003)
a_k	Coefficient in empirical coefficient method (Equation 3.8)
$a_{p,q}$	Coefficients in the T_R-VI-SVAT model (Carlson, 2007)
α	Broadband, blue-sky albedo
α_{PT}	Priestley–Taylor coefficient
b	Slope of linear model relating T_R to T_1–T_2 (SEBAL, METRIC)
b_{ds}	Empirical coefficient in downscaling model (Kustas et al., 2003)
b_k	Coefficient in empirical coefficient method (Equation 3.8)
c	Temperature correction factor (SSEBop)
c_{ds}	Empirical coefficient in downscaling model (Kustas et al., 2003)
c_k	Coefficient in empirical coefficient method (Equation 3.8)
c_L	Mean potential stomatal conductance per unit leaf area (Mu et al., 2011)
C_p	Specific heat capacity of air
C_{rad}	Adjustment factor for sloped surfaces (Allen et al., 2007)
CWSI	Crop water stress index = 1–ET_f
D	Vapor pressure deficit
d	Zero-plane displacement height ~ 2/3 h
dT	T_h–T_c (SSEBop)
e	Vapor pressure
e_{sat}	Saturated vapor pressure
ET	Actual evapotranspiration
ET_f	Reference ET fraction
ET_o	Potential evapotranspiration of a reference crop
ET_{o24}	ET_o for a 24 h period

EVI	Enhanced vegetation index
ε_o	Broadband surface emissivity
f_c	Vegetation cover fraction
f_g	Green canopy fraction (Fisher et al., 2008)
f_M	Plant moisture constraint (Fisher et al., 2008)
FPAR	Photosynthetically active radiation
f_{SM}	Soil moisture constraint (Fisher et al., 2008)
f_T	Temperature constraint to ET (Fisher et al., 2008)
f_{wet}	Relative surface wetness (Fisher et al., 2008)
F_{wet}	Water cover fraction (Mu et al., 2011)
G	Ground heat flux
γ	Psychometric constant
H	Sensible heat flux
h	Vegetation height
η	Coefficient in empirical crop coefficient method
K_c	Crop coefficient in FAO-56 method
K_s	Soil moisture stress coefficient in FAO-56 method
LAI	Leaf area index
LST	Land surface temperature, equivalent to T_R
LW↑	Upwelling longwave radiation
LW↓	Downwelling longwave radiation
Λ	Evaporative fraction
Λ_{24}	Λ for 24 h period
Λ_d	Λ for daylight hours
Λ_{op}	Λ at time of overpass
λ	Latent heat of vaporization
λE_I	Latent heat flux from evaporation from wet canopy leaf surfaces
λE_s	Latent heat flux from evaporation from the soil surface
λE_{SP}	Potential latent heat flux from soil evaporation (Mu et al., 2011)
λET	Latent heat flux
λET_c	Latent heat flux from transpiration
m(D)	Multiplier limiting stomatal conductance by D (Mu et al., 2007)
m(Tmin)	Multiplier limiting stomatal conductance by minimum air temperature (Mu et al., 2007)
Mo	Soil moisture
N*	NDVI
NDVI	Normalized difference vegetation index
$NDVI_o$	NDVI for bare soil
$NDVI_s$	NDVI for dense vegetation
Ω	Index of degree of clumping (ALEXI)
σ	Stefan–Boltzmann constant
r_a	Aerodynamic surface resistance
r_{a_s}	Aerodynamic resistance at the soil surface (Mu et al., 2011)
R_{ah}	Aerodynamic resistance to turbulent heat transport between z_1 and z_2
RH	Relative humidity
RMSE	Root-mean-square error
R_n	Net radiation
R_{n24}	Net radiation over 24 h period

AQ1 (margin note next to NDVI row)

R_{ns}	Net radiation at the soil surface
Rs	sensible heat exchange resistance of the soil surface
r_s	Resistance of the land surface or plant canopy to ET
r_{s_c}	Dry canopy resistance to transpiration (Mu et al., 2011)
r_{s_wetC}	Wet canopy resistance to evaporation
Rx	total boundary layer resistance of the canopy
ρ	Air density
s	Slope of the saturation vapor pressure versus temperature curve
SAVI	Soil-adjusted vegetation index
SW↓	Incoming shortwave radiation
T_1	Aerodynamic temperature of the evaporating surface at height z_1
T_{1c}	Vegetation canopy temperature (ALEXI)
T_{1s}	Soil temperature (ALEXI)
T_2	Air temperature at height z_2
T_c	Theoretical temperature under cool/moist conditions (SSEBop)
T_h	Theoretical temperature under hot/dry conditions (SSEBop)
T_R	Radiometric surface temperature, equivalent to LST
$\hat{T}_{Rhi}$	Predicted T_R at high spatial resolution (Kustas et al., 2003)
$\hat{T}_{Rlow}(NDVI_{low})$	Predicted radiometric temperature using low resolution NDVI
$\hat{T}_{Rlow}(NDVI_{hi})$	Predicted radiometric temperature using high-resolution NDVI (Kustas et al., 2003)
T_{Rmax}	Minimum T_R over vegetation
T_{Rmin}	Maximum T_R over bare soil
T_{scaled}	Scaled T_R
θ	View angle
VI	Vegetation index
VI_{max}	VI value when ET is maximum
VI_{min}	VI value for bare soil
z_1	Height above the ground surface of the evaporating surface, $= d + z_{0m}$
z_2	Height at which air temperature is measured (often 2 or 3 m)
z_{om}	Surface roughness for momentum transport, ~0.03–0.123 h

Organizations, Satellite, and Model Acronyms

ABL	Atmospheric boundary layer
AGRIMET	Agricultural meteorological modeling system
ALEXI	Atmosphere–land exchange inverse model (Anderson et al., 1997)
ASTER	Advanced spaceborne thermal emission and reflection radiometer
AVHRR	Advanced very high resolution radiometer

CERES	Clouds and Earth's Radiant Energy System
CONUS	Conterminous United States
DAIS	Digital airborne imaging spectrometer
DisALEXI	Disaggregation ALEXI model (Norman et al., 2003)
DSTV	diurnal surface temperature variation
DTD	Dual-temperature-difference
ECMWF	European Centre for Medium-Range Weather Forecasts
EO	Earth observation
FIFE	First ISLSCP (International Satellite Land Surface Climatology Project) Field Experiment
FLUXNET	Global network of micrometeorological flux tower sites
GDAS	Global Data Assimilation System
GG model	Granger and Gray (GG) model (Granger and Gray, 1989)
GLDAS	Global Land Data Assimilation System
LSA-SAF	Land Surface Analysis Satellite Applications Facility
MERRA	Modern ERA-Retrospective Analysis for Research and Applications
METRIC	Mapping Evapotranspiration at high Resolution with Internalized Calibration
MMR	Modular multispectral radiometer
MOD16	MODIS ET product, also called PM-Mu (Mu et al., 2011)
MOD43B3	MODIS albedo product
MODIS	
MSG	Meteosat second generation satellite
NCEP-NCAR	National Centers for Environmental Prediction–National Center for Atmospheric Research
NWS-NOAH	National Weather Service
PoLDER	Polarization and directionality of Earth reflectance instrument
PT-JPL	Priestley–Taylor jet propulsion laboratory model (Fisher et al., 2008)
RMSD	Root-mean-square difference
SEBAL	Surface energy balance algorithm (Bastiaanssen et al., 1998)
SEBS	Surface Energy Balance System (Su, 2002)
SEVIRI	Spinning enhanced visible and infrared imager
SGP	Southern Great Plains
Sim-ReSET	Simple remote sensing evapotranspiration model
SMACEX	Soil Moisture–Atmosphere Coupling Experiment
SMACEX	Soil Moisture–Atmosphere Coupling Experiment
SRB	Surface radiation budget
SSEB	Simplified surface energy balance
S-SEBI	Simplified surface energy balance index
SSEBop	Operational simplified surface energy balance
STARFM	Spatial and temporal adaptive reflectance fusion model
SVAT	Soil vegetation atmosphere transfer model
TRMM	Tropical Rainfall Measurement Mission
TSM	Two source model
VMC	Vegetation and moisture coefficient, equivalent to ET_f

AQ2

3.1 Introduction

Agriculture accounted for the majority of human water use and for more than 90% of global fresh water consumption during the twentieth century (Hoekstra and Mekonnen, 2012; Shiklomanov, 2000). Streamflow depletion due to enhanced evapotranspiration (ET) from irrigated crops impacts freshwater ecosystems globally (Foley et al., 2005). Water scarcity limits crop production in many arid and semiarid regions, and water is likely to be a key resource limiting food production and food security in the twenty-first century (Foley et al., 2011; Vorosmarty et al., 2000). Despite this, estimates of the location and temporal dynamics of ET from croplands are often uncertain at a variety of spatial and temporal scales. Better information on ET can be useful in several applications at a range of spatial scales, including water resources, agronomy, and meteorology (e.g., Rivas and Caselles, 2004). At the scale of irrigation projects, maps of ET can assist with irrigation scheduling and demand assessment. Measurements of ET are required for monitoring plant water requirements, plant growth, and productivity, as well as for irrigation management and deciding when to carry out cultivation procedures (e.g., Consolli et al., 2006; Glenn et al., 2007; Yang et al., 2010).

At regional and river basin scales, ET estimates can assist with water allocation decisions to support agriculture and ecosystems, including strategies for drought management. Global ET assessments can help understand, for example, how the global food production system may respond to global climate change. Data on the energy equivalent of ET (latent heat flux, λET) are also of key significance in the numerical modeling and prediction of atmospheric and hydrological cycles and in improving the accuracy of weather forecasting models (Jacob et al., 2002). ET is the single most important mechanism of mass and energy exchange between the hydrosphere, biosphere, and atmosphere, playing a critical role in both water cycle and energy balance (Sellers et al., 1996) and regional circulation patterns (Lee et al., 2009, 2011). Quantitative information on ET is also important for understanding the processes that control ecosystem CO_2 exchange (Scott et al., 2006) as well as the interactions between parameters in different ecosystem processes (Wever et al., 2002).

ET can be measured in the field with different types of instruments including lysimeters and eddy covariance, surface renewal, or flux variance systems (French et al., 2012; Petropoulos et al., 2013; Swinbank, 1951). Field methods estimate ET over a range of spatial scales, from ~1 m for lysimeters and up to ~100–1000 m for eddy covariance towers. While field data are the most direct way to measure ET, their use for the measurement of ET over large areas is limited due to the expense of maintaining the field equipment and to the large spatial variability in ET, particularly in agricultural settings (Ershadi et al., 2013; McCabe and Wood, 2006).

For example, the global inventory of eddy flux towers (FLUXNET) (Baldocchi et al., 2001) reports data for fewer than 500 active towers with most towers concentrated in the United States and Europe and no towers in some countries where knowledge of ET is critical to water management (Jung et al., 2009).

In the absence of in situ data on ET, crop models are often used to estimate ET under different crop and soil moisture conditions (Allen, 2000). Application of crop models to a new location and at regional scales suffers from several difficulties. Required input data, including crop growth stage and cropping calendars, may be difficult to determine in large areas with heterogeneous cover and intraseasonal or interannual variability in cropping patterns. The model parameters are often functions of relative humidity (RH) and wind speed, resulting in corrections of up to 30% for tall crops (2–3 m) growing in conditions of low humidity and high wind speeds compared to the same tall crop in a humid climate with low wind speeds due to its large aerodynamic roughness (Allen et al., 1998, p. 93). Crop models of ET may be difficult to parameterize during the initial growth stages, which are particularly sensitive to environmental conditions like wetting frequency and soil texture, which introduces uncertainty where soil evaporation is an important component of total ET.

Given the limitations of field measurements and the difficulty of estimating the parameters in crop models without additional data on crop calendars and condition, Earth observation (EO) technology provides an opportunity to estimate ET at a variety of spatial and temporal scales. EO is defined here as the collection of imagery from aerial and satellite platforms. EO technology is recognized as the only viable solution for obtaining estimates of ET at the spatiotemporal scales and accuracy levels required by many applications (Glenn et al., 2007; Melesse et al., 2008). Previous reviews of the use of EO data for ET estimation are available (Courault et al., 2005; Gonzalez-Dugo et al., 2009; Kalma et al., 2008; Kustas and Norman, 1996; Petropoulos, 2013; Verstraeten et al., 2008). Gowda et al. (2008) provided an overview of ET estimation in agriculture but focused on energy-based methods, which is one of several methods available (Table 3.1).

The present chapter provides a critical and systematic overview of different modeling approaches to estimate ET from EO data, with a focus on applications in agriculture. The chapter is structured as follows: First, we review methods for estimating net radiation (R_n), which is required by all ET modeling techniques described in the chapter. Descriptions of R_n calculations are also included because, in agricultural applications, special adaptations are often required to calculate outgoing radiation at sufficiently high spatial resolution to capture spatial variability in radiation caused by the heterogeneous land surface. We then discuss three major families of methods used to calculate ET using EO data, with a focus on methods that use vegetation indices and/or radiometric land surface temperature (T_R). T_R is often called the land surface temperature or the surface temperature measured by the

satellite (T_s); here, we use the term radiometric land surface temperature and the symbol T_R to emphasize that it is the temperature estimated from thermal radiation detected at the satellite sensor. While microwave (MW)-based methods have been developed and could be particularly useful for areas with cloud cover; the spatial resolution of MW imagery, at 35–65 km², is deemed too coarse for application to agricultural areas (Petropoulos, 2013).

We use common mathematical symbols for each method to facilitate intercomparison, and highlight similarities in the conceptual foundations of the various methods. Sufficient detail is provided to implement and compare some of the most commonly used algorithms and recommendations for the application of each method are also given, discussing any special issues related to estimating ET in agricultural landscapes. The accuracy of the methods is then compared, special problems in application of the methods to crops are discussed, and future research directions are highlighted.

3.2 Overview of Methods for ET Calculation Using Remote Sensing

EO sensors do not directly measure ET or λET. The spectral radiance measures they provide have to be combined in some form of retrieval algorithm or model in order to estimate ET. Several algorithms have been developed in the last four decades for estimating ET using either space- or airborne systems. The available EO-based methods can be broadly grouped into three basic families: (1) vegetation-based methods, (2) radiometric land surface temperature–based methods, and (3) triangle/trapezoid or scatterplot inversion methods.

Several different terms are used to describe the water demand of the atmosphere and the actual use of water by crops (Allen et al., 1998). Potential evapotranspiration is the amount of water lost to both evaporation from the soil surface, wet canopy, and open water surfaces and to transpiration through the leaves of vegetation not experiencing soil moisture stress. Potential ET is a function of climatic variables like net radiation, temperature, and humidity and of vegetation characteristics. For a well-watered crop grown under optimal conditions, potential ET can vary with leaf area, stage of development, photosynthetic pathway, and rooting depth, so a second term, reference ET (ET_o) is defined as the amount of water used by a specific reference crop, usually a well-watered grass with specific characteristics (see Section 3.2.2). Crop ET for a given vegetation or crop type without soil moisture limitation is indicated by the variable ET_c (Allen et al., 1998). Finally, actual ET is the amount of water that is lost via both evaporation from the soil surface and transpiration from a specific vegetation cover under actual field conditions, including limitations to ET caused by soil moisture stress, nutrient limitation, and pathogens. In this chapter, we use the symbol ET and the term evapotranspiration to represent actual evapotranspiration of a given land surface (Glenn et al., 2011). λET is simply the product of ET and the latent heat of

TABLE 3.1 Three families of methods to estimate evapotranspiration (ET) from Earth Observation data, and their advantages, disadvantages, error, and recommended uses.

Method of ET estimation	Advantages	Disadvantages	Recommended for	Not recommended or untested for	Error	Reference
1. Vegetation-based models						
Empirical	Ease of implementation	Requires ground data for calibration; does not directly estimate soil evaporation	Small geographic regions with ground reference data, riparian and agricultural vegetation, desert, semi-arid rangelands, vegetated wetlands	Regional or Global application without reference data for calibration	Mean error 0.12 for ETf and 5% error for annual ET from flux towers and soil moisture balance (Nagler et al., 2013) RSMD 10–30% compared to mean ET (Glenn et al., 2010) Mean error 4% compared with daily ET from eddy covariance towers (Samani et al., 2009); Mean error 15% compared with daily ET (Duchemin et al., 2006); RMSE 15% compared with daily ET (Hunsaker et al., 2007a, 2007b);	Power function: Nagler et al. (2013); Extreme VI values: Glenn et al. (2010); Beer-Lambert Law: Nagler et al., 2013; CropCoeff-VI: Bausch and Neale, 1987, Neale, 1989, Choudhury et al., 1994; Linear regression on NDVI, SAVI: Samani et al. 2009, Campos et al. 2010; Desert: Glenn, Morino, et al, 2008; Wetlands: Glenn, Mexicano, et al, 2013
PT-JPL	Relative ease of implementation; Minimal ground data requirements; Operational globally; Does not require calibration	May underestimate soil evaporation from irrigated areas in dry climates	Global and regional rainfed systems	Needs further testing in irrigated agriculture with high soil evaporation	Mean error 13% compared with of mean annual ET from eddy covariance towers (Fisher et al, 2008)	Fisher et al., 2008; Alternate formulation: Marshall et al., 2013
MOD16	Minimal ground data requirements; Operational globally; Does not require calibration	May underestimate soil evaporation from irrigated areas in dry climates	Global and regional rainfed systems	Needs further testing in irrigated agriculture with high soil evaporation	RMSE ~20%, MAB 24–25%, compared with daily ET from eddy covariance towers (Mu et al., 2011); ~50% compared with ET at regional or national scale (Velpuri et al., 2013)	Leuning et al., 2008; Mu et al., 2011, 2007, 2013; Nishida and Nemani, 2003
2. Radiometric land surface temperature based models						
Overall					RMSD <50 W/m² and <33 W/m² compared with instantaneous λET and H fluxes respectively (Gonzalez-Dugo et al.,2009)	Gonzalez-Dugo et al. (2009)
SEBAL, METRIC	Minimal ground data; Accurate in semi-arid environments with irrigation; Accurate for wet soil and inundated surfaces	Moderate complexity; Requires extremes of wet and dry to be present in a scene, and calibration for each image; Issues in merging across scenes	Routine application in irrigated agriculture in semi-arid and arid climates; Single scenes	Humid environments; Global applications; Data scarce regions	RMSE 15–20% compared to daily ET from eddy covariance towers (Allen et al., 2011); RMSE ~5% compared to seasonal ET estimates (Bastiaanssen et al., 2005)	Bastiaanssen et al., 2002, 1998; Allen et al., 2007

(Continued)

Remote Sensing of Water Resources, Disasters, and Urban Studies

TABLE 3.1 (*Continued*) Three families of methods to estimate evapotranspiration (ET) from Earth Observation data, and their advantages, disadvantages, error, and recommended uses.

Method of ET estimation	Advantages	Disadvantages	Recommended for	Not recommended or untested for	Error	Reference
ALEXI, DisALEXI	Minimal ground data; Accurate in a variety of vegetation types and climates; Accurate for wet soil and inundated surfaces	High complexity of implementation; Requires two images for each daily ET estimate; Coarse resolution before downscaling	Regional and global applications, operational data product	Routine application for applied irrigation systems or management; Data scarce regions	RMSD 40 W/m^2, MAD 30 W/m^2, R^2 0.77 (Anderson et al., 1997) RMSD 40–50 W/m^2 (Norman et al., 2003) MAD 15–20% for 30min avg, 10% daily, and ~5% seasonal (Anderson et al., 2013)	ALEXI: Anderson et al., 1997; DisALEXI: Norman et al., 2003;
SSEB, SSEBop	Minimal ground data; Ease of implementation; Operational application over large areas	Potentially inaccurate in regions with high spatial variability in albedo or elevation; Requires in-situ meteorological data; Does not solve energy balance completely; Physical processes of ET are not fully represented	Regional and global applications, irrigated agriculture	Heterogeneous vegetation, mountainous regions; Regions with high albedo and high emissivity; Data scarce regions	Mean error <30% (Senay et al., 2007); Mean error ~60% on regional or national scale (Velpuri et al., 2013)	SSEB: Senay et al., 2007; SSEBop: Senay et al., 2013;
3. Scatterplot or triangle methods						
Overall	Ease of implementation, few parameters (except SVAT method)	Require extremes of wet and dry to be present in a scene; subjectivity in selecting wet/dry pixels; issues in merging across scenes for large areas	Routine application in irrigated agriculture in semi-arid and arid climates	Humid environments; Global applications		Petropoulos et al. 2009
T_R–VI methods	Computationally straightforward; Relative independence from site specific tuning of model-parameters	Assumes linear relationships between location in T_R–VI space and ET; Clouds, standing water, and sloping terrain need to be masked	Local to regional scale sites	Homogenous land cover	RSMD ~30% compared to daily ET (Jiang and Islam, 2001); RMSD 45 Wm^{-2}, R^2 = 0.86, bias of 5.6 Wm^{-2} compared to daily λET from eddy covariance towers (Nishida et al., 2003a, 2003b);	Jiang and Islam, 2001; Nishida et al. 2003a, 2003b; Tang et al 2010; Zhang et al., 2006

(*Continued*)

TABLE 3.1 (*Continued*)   Three families of methods to estimate evapotranspiration (ET) from Earth Observation data, and their advantages, disadvantages, error, and recommended uses.

Method of ET estimation	Advantages	Disadvantages	Recommended for	Not recommended or untested for	Error	Reference
T_R-T_2 difference and VI scatterplot	Insensitive to absolute accuracy of T_R; Requires small number of in-situ observations	Often applicable for homogenous areas (Moran et al. 1994)	Areas of partial vegetation cover		RMSD 29 Wm⁻² compared to instantaneous λET (Moran 1996); RMSD 59 Wm⁻², bias −42 Wm⁻² compared to λET from eddy covariance towers (Jiang and Islam, 2003) RMSD 0.08 to 0.19 and R² 0.4–0.7 in Λ from MODIS and AVHRR (Venturini et al., 2004);	Moran et al., 1994
T_R-albedo scatterplot (moved up in table because it is above Day-Night Tr in text)	Requires small number of in-situ observations; Realistic assumption (extreme T for the wet and dry conditions vary with changing surface reflectance)	Requirement to identify extreme points in the scatterplot domain	Operational products in small geographic areas		Error 90 Wm-2 for instantaneous ET and 1mm/d daily ET compared to lysimeters (Gomez, et al., 2005, Sobrino, et al., 2005) RMSD 64 Wm⁻², R² 0.85 compared to daily ET (Zahira et al. (2009); RMSE 25–32% compared to mean daily ET from Bowen ratio tower (Bhattacharya et al., 2010);	S-SEBI: Roerink et al., 2000
Day-night T_R difference and VI scatterplot	Requires small number of in-situ observations	Assumes three dominant land cover types; Requires both day and night time observations	Areas with three dominant land cover types	Areas with mixed land cover types	Errors 2.8%–3.9% compared to daily ET from lysimeters (Chen et al 2002); RMSD 0.106, bias −0.002, R² 0.61 in Λ (Wang et al 2006)	Chen et al., 2002; Wang et al., 2006
Triangle-SVAT model	Non-linear interpretation of T_R/VI feature space; Potential for deriving additional parameters (soil surface moisture, daytime mean λET and H fluxes)	Large number of input parameters; Requires user expertise	Operational products; Global and regional scale sites	Homogenous land cover	RMSD ±10% for daily ET from FIFE/MONSOON (Gillies et al., 1997); Error ~15–50% for λET from in situ and airborne measurements (Brunsell and Gillies, 2003); RMSD 40 Wm⁻² compared to λET from CarboEurope (Petropoulos et al., 2010, and Petropoulos and Carlson, 2011)	Carlson, 2007; Petropoulos and Carlson, 2011

vaporization of water at a given temperature (λ). It is sometimes used instead of ET because it is a rate that can be expressed for a given instant in time and is also the variable measured by several field techniques. We use ET and λET interchangeably depending on the method being described.

3.2.1 Net Radiation

EO-based methods for estimating ET, including all methods reviewed in this chapter, depend on accurate determination of R_n, (in units of W/m^2) which is calculated as

$$R_n = (1-\alpha)SW\downarrow + (LW\downarrow - LW\uparrow) \qquad (3.1)$$

where
  α is broadband blue-sky albedo (dimensionless)
  SW↓ is incoming shortwave radiation (W/m^2)
  LW↓ is downwelling longwave radiation
  LW↑ is upwelling longwave radiation (W/m^2)

For field-scale applications, R_n is often estimated with meteorological data alone using a variety of methods reviewed in several publications (e.g., Allen et al., 1998).

For large regions or areas without adequate meteorological data, R_n can be calculated from well-established approaches based on primarily EO data. An excellent review of the different methods for the estimation of the different components of the radiation budget from EO sensors, including the operationally distributed products available, was provided recently by Liang et al. (2013). SW↓ and LW↓ depend on atmospheric properties that can be estimated accurately with coarse-resolution datasets (1 degree). α and LW↑ depend on surface conditions, including reflectivity and temperature, which are more spatially variable. In the following text, we review global datasets for SW↓ and LW↓ and other methods to estimate α and LW↑.

3.2.1.1 Regional and Global Datasets for Net Radiation

At regional and global scales, R_n can be estimated with gridded data from surface climate reanalysis that assimilate remote sensing data or from EO data alone, with errors of ±10%–20% compared to ground measurements (Bisht et al., 2005). Gridded datasets used for regional to global scale R_n estimation can be separated into two spatiotemporal categories: 1979–present (1° spatial resolution) and 2000–present (0.25° spatial resolution). The higher spatial resolution post-2000 is due to the launch of the moderate resolution imaging spectroradiometer (MODIS) satellites and other EO systems that facilitate the downscaling of the surface energy budget (Gottschalck et al., 2005). Liang et al. (2010, 2013) provide good introductions to commonly used R_n datasets and associated uncertainties. For 1979–present, several coarse resolution and downscaled sources exist. The most commonly used is the global energy and water cycle experiment surface radiation budget (Gupta et al., 1999), which provides three hourly shortwave and longwave radiation

fluxes at one degree resolution. These data are generated primarily from the International Satellite Cloud Climatology Project (Rossow and Schiffer, 1991, 1999; Schiffer and Rossow, 1983) and Global Modeling and Assimilation Office (http://gmao.gsfc.nasa.gov/) meteorology. The original dataset covering 1983–2007 has been expanded to cover from 1979 to present, as part of the Modern ERA-Retrospective Analysis for Research and Applications (MERRA) (Rienecker et al., 2011) dataset. MERRA is updated regularly with remote sensing and observed data and fed through a land surface catchment hydrology model, which provides additional outputs and further reduces inconsistencies. Another one degree resolution surface reanalysis dataset is the Global Land Data Assimilation System (GLDAS) (Rodell et al., 2004) product. GLDAS assimilates NOAA/Global Data Assimilation System atmospheric fields, Climate Prediction Center merged analysis of precipitation fields, and observation-driven shortwave and longwave radiation using the Air Force Weather Agency's agricultural meteorological modeling system (Idso, 1981; Shapiro, 1987) to parameterize four land surface realizations: (1) Noah land surface model (Chen et al., 1996, 1997), (2) community land model (Bonan, 1998), (3) mosaic (Koster and Suarez, 1996), and (4) variable infiltration capacity model (Liang et al., 1994). The forcing data for GLDAS, like MERRA, is produced at three hourly intervals at one degree resolution from 1948 to present (Bosilovich, 2008). Although at much coarser spatial resolution, two other datasets are commonly used: National Centers for Environmental Prediction–National Center for Atmospheric Research (NCEP-NCAR) (Kalnay et al., 1996) and European Centre for Medium-Range Weather Forecasts (ECMWF) interim reanalysis (Morcrette, 1991, 2002). NCEP-NCAR shortwave and longwave fluxes are available at six hourly intervals from 1948–present at 2.5 degree resolution, while the ECMWF interim shortwave and longwave flux is available at six hourly intervals spanning1979–present at 1.5 degree resolution. Sheffield et al. (2006) uses surface elevation to downscale the NCEP-NCAR to one degree resolution. Other downscaled R_n products can be found on the corresponding Princeton University Terrestrial Hydrology Research Group webpage (http://hydrology.princeton.edu/data.php).

For regional estimation of R_n after 2000, EO data are incorporated directly or indirectly into one of the aforementioned reanalysis datasets. These methods involve several assumptions or ground-based estimates of α, T_R, and emissivity for model calibration (Bisht et al., 2005). Since 2000, MODIS products, including aerosol depth, temperature, emissivity, air temperature, dew point temperature, and α, have been combined and extrapolated from once-a-day measurements to daily flux at a quasi-1 km resolution. The Clouds and Earth's Radiant Energy System initially aboard NASA's Tropical Rainfall Measurement Mission platform and later placed on NASA's Terra and Aqua platforms is a radiometer that collects solar-reflected, Earth-emitted, and total radiation to determine Earth's radiation budget. Data is available from 2000–present at three hourly, monthly average, or monthly average by hour at 1 degree resolution. The Land Surface Analysis Satellite Applications Facility

AQ3

(http://landsaf.meteo.pt/) has also developed a radiation budget for the Africa and Europe using the spinning enhanced visible and infrared imager (SEVIRI) radiometer onboard the Meteosat Second Generation (MSG) satellite. The MSG/SEVIRI platform provides 30 min 3-km resolution α, land surface temperature, emissivity, SW↓, and LW↓ information from 2004 to present.

Satellite methods to estimate components of R_n are continually evolving and being evaluated against each other, including for shortwave (Ma and Pinker, 2012), longwave (Gui et al., 2010), and R_n (Bisht and Bras, 2010), and it can be anticipated that reanalysis datasets that incorporate satellite imagery will continue to be improved.

ET mapping often uses vegetation indices or T_R data that has a higher spatial resolution (e.g., 30 m, 250 m, 1 km) than is available from the global grids of radiation, but not all parts of the radiation budget need to be downscaled in detail. Incoming shortwave (SW↓) and incoming longwave (LW↓) are determined primarily by atmospheric properties and are therefore often assumed homogeneous over a given cell in the global gridded products, so they can be taken directly from the gridded data, though some applications (e.g., MOD16) interpolate to the resolution of the other satellite imagery used to map vegetation indices or radiometric surface temperature in order to avoid abrupt changes at cell boundaries (Mu et al., 2011). MOD16 calculates net longwave as a function of grid-cell average air temperature, which is in turn taken from the global gridded dataset (MERRA) and interpolated to 1 km using nonlinear interpolation on the four nearest neighbors (Mu et al., 2007).

3.2.1.2 Outgoing Shortwave and Longwave at High Spatial Resolution

In contrast to incoming radiation, SW↑ and LW↑ depend strongly on land surface properties and so may exhibit significant spatial variation over short distances, particularly in agricultural areas with sharp boundaries in vegetation with different levels of soil moisture stress. Algorithms for calculating albedo from Landsat imagery are included in several ET estimation models, including mapping evapotranspiration at high resolution with internalized calibration (METRIC) (Allen et al., 2007), and an albedo product is directly available for MODIS (MOD43B3). A review of the methods is also presented in Liang et al. (2013). Outgoing longwave radiation can be calculated at high spatial resolution using surface radiometric temperature from satellite imagery and an estimate of the surface emissivity. This approach is used in the METRIC and surface energy balance algorithm (SEBAL) models (Allen et al., 2007) and in many other applications (Bisht et al., 2005; Tang and Li, 2008):

$$LW\uparrow = \varepsilon_o \sigma T_R^4 \qquad (3.2)$$

where

ε_o is the broadband surface emissivity

σ is the Stefan–Boltzmann constant (5.67×10^{-8} W/m^2 K)

T_R is the radiometric surface temperature, which is often assumed equal to the surface temperature

Some remote sensing products include estimates of ε_o, including MODIS and advanced spaceborne thermal emission and reflection radiometer (ASTER), though there may be significant errors over heterogeneous landscapes (Liang et al., 2013).

3.2.1.3 Available Energy and the Ground Heat Flux

Available energy is the amount of R_n left over after accounting for the ground heat flux (G; W/m^2) and is calculated as R_n–G. G is usually close to zero over 24 h, weekly, or 10 day periods and is assumed to be zero in several methods (e.g., Table 3.2), but G can be significant at the instant of satellite overpass and is particularly important for energy-based methods. Instantaneous G can account for up to 50% of R_n for sparse vegetation and can average 20%–30% for normalized difference vegetation index (NDVI) values up to around 0.6 (Bastiaanssen et al., 1998), so it cannot be neglected unless there is a high canopy cover fraction. Instantaneous G can be calculated with a variety of algorithms (Murray and Verhoef, 2007), the simplest of which is to assume that G is a constant fraction of R_n, usually between 0.2 and 0.5 at midday (Choudhury, 1989), with specific model applications using constant values of, for example, 0.35 (Norman et al., 1995) or 0.31 (Anderson et al., 1997). Other models include those where G/R_n is a function of NDVI, which is applicable over vegetated areas but not water (Morse et al., 2000):

$$G = 0.30*\left(1 - 0.98\text{NDVI}^4\right)R_n \qquad (3.3)$$

G can also be estimated by a more complicated empirical equation (Table 3.3) that describes heat transfer using T_R, α and an extinction factor that describes attenuation of radiation through canopies using NDVI (Clothier et al., 1986; Choudhury, 1989; Kustas and Daughtry, 1990; Van Oevelen, 1991). More detailed approaches incorporate soil properties (Murray and Verhoef, 2007). Using empirical equations, the error in G is often around 20%–30% (Petropoulos, 2013). Over water bodies, G is usually larger and requires a different equation, often calibrated to local measurements (Morse et al., 2000). The user is recommended to try a few different equations for G to test its sensitivity to the equation used.

3.2.2 Vegetation-Based Methods for ET Estimation

Vegetation-based methods to estimate ET use an index of vegetation biomass or leaf area index (LAI) to calculate crop ET. One of the most widely available global ET datasets, MOD16, uses a variant of the Penman–Monteith (PM) equation to estimate ET (Leuning et al., 2008; Mu et al., 2007, 2011; Nishida and Nemani, 2003). MOD16 is also referred to as PM-Mu in the literature. MOD16 and several other vegetation-based methods use the PM

TABLE 3.2   Inputs and Calculation Steps for the PT-JPL Model

Inputs	Units	Description	Source or Equation
1. R_n	W/m²	24 h mean net radiation	Equation 3.1
2. r_{NIR}		Near-infrared spectrum reflectance	Imagery
3. r_{VIS}		Visible spectrum reflectance	Imagery
4. T_{max}	°C	Maximum temperature	Meteorological data
5. e_a or RH	kPa	Water vapor pressure	Meteorological data
	—	Relative humidity	Meteorological data
Derived Variables			
1. G	W/m²	Ground heat flux	Assumed zero
2. SAVI	—	Soil-adjusted vegetation index	$1.5(r_{NIR} - r_{VIS})/(r_{NIR} + r_{VIS} + 0.5)$
3. NDVI	—	Normalized difference vegetation index	$(r_{NIR} - r_{VIS})/(r_{NIR} + r_{VIS})$
4. f_{APAR}	—	Fraction of PAR absorbed by green vegetation	$m_1 SAVI + b_1$ $m_1 = 1.2 \times 1.136$ $b_1 = 1.2 \times -0.04$
5. f_{IPAR}	—	Fraction of PAR intercepted by all vegetation cover	$m_2 NDVI + b_2$ $m_2 = 1, b_2 = -0.05$
6. LAI	—	Leaf area index	$-\ln(1 - f_{IPAR})/k_{PAR}$ $k_{PAR} = 0.5$
7. R_{ns}	W/m²	Net radiation to the soil	$R_{ns} = R_n(\exp(-k_{Rn}LAI))$ $k_{Rn} = 0.6$
8. f_{wet}	—	Relative surface wetness	RH^4
9. f_g	—	Green canopy fraction	f_{APAR}/f_{IPAR}
10. T_{opt}	°C	Optimum plant growth temperature	T_{max} at $max(PARf_{APAR}T_{max}/VPD)$
11. f_T	—	Plant temperature constraint	$\exp\left(-\left(\dfrac{T_{max} - T_{opt}}{T_{opt}}\right)^2\right)$
12. f_{SM}	—	Soil moisture constraint	$RH^{VPD/\beta}$ $\beta = 1.0$ kPa
13. λET_c	W/m²	Transpiration from dry canopy	Equation 3.9
14. λET_I	W/m²	ET from wet canopy	Equation 3.10
15. λET_s	W/m²	Soil evaporation	Equation 3.11

Source: Fisher, J.B. et al., *Remote Sens. Environ.*, 112, 901, 2008. With Permission.

equation to calculate ET from crop canopies and soil surfaces (Mu et al., 2011):

$$\lambda ET = \frac{s(R_n - G) + \rho C_p D/r_a}{s + \gamma(1 + r_s/r_a)} \qquad (3.4)$$

where

λET is latent heat flux (W/m²)

ET is mean daily evapotranspiration (mm/s, converted to mm/day by multiplying by 86,400 s/day)

λ is the latent heat of vaporization (~2.26×10^6 J/kg)

s (Pa/K) is the slope of the curve relating saturated vapor pressure (e_{sat} in Pa) to air temperature

ρ is air density (kg/m³)

C_p is the specific heat capacity of air (J/kg K)

D is the vapor pressure deficit ($e_{sat} - e$, where e is actual vapor pressure in Pa)

r_a is the aerodynamic surface resistance (s/m)

γ is the psychometric constant (~0.066 kPa/K or as calculated in Mu et al., 2007)

r_s is the resistance of the land surface or plant canopy to ET (s/m)

$R_n - G$ is for the 24 h period, so G is usually close to zero

Several of these parameters (s, γ, ρ, C_p, e, e_{sat}) are determined from meteorological data or elevation and do not depend on satellite-derived vegetation characteristics. The meteorological inputs are taken from either local meteorological stations or gridded global meteorological datasets and include air temperature, which is used to calculate e_{sat}, wind speed, and RH, which is used to calculate e. The two main parameters that control ET for different vegetation types and different levels of soil moisture stress are r_a and, often more importantly, r_s. Reference ET (ET_o) is calculated with r_a and r_s parameters for a reference surface, for example, a grass 12 cm tall with an r_s of 70 s/m and albedo 0.23 (Allen et al., 1998).

Alternatively, the Priestley–Taylor equation has been used in global models, particularly the Priestly–Taylor jet propulsion laboratory (PT-JPL) model (Fisher et al., 2008) and in several scatterplot methods (Jiang and Islam, 2001):

$$\lambda ET = \alpha_{PT} \frac{s}{s + \gamma}(R_n - G) \qquad (3.5)$$

where

α_{PT} (unitless) is an empirical coefficient

TABLE 3.3 Inputs and Calculation Steps for the SEBAL Model

Inputs	Description	Data Source
6. R_n	Instantaneous net radiation	Equation 3.1
7. R_{n24}	24 h mean net radiation	Equation 3.1
8. NDVI	Normalized difference vegetation index	Imagery
9. T_R	Radiometric land surface temperature (K)	Imagery
10. U	Wind speed (m/s)	Wind speed at meteorological station
11. z_0m	Surface roughness (dimensionless)	Land use map, literature values[a]
12. Elevation	Surface elevation(m)	Digital elevation model (DEM)

Derived Variables	Description	Equation
16. G	Ground heat flux (W/m²)	$G = Rn \times (T_R - 273.15/\alpha) \times (0.0032 \times C1 \times \alpha + 0.0062 \times (C1 \times \alpha)^2) \times (1 - 0.978NDVI^4))$ where C1 is a correction coefficient (= 1.1)[b]
17. U_x^*	Friction velocity at meteorological station	$U_x^* = \dfrac{(0.41U)}{\ln(\text{station height}/z_0m \text{ at station})}i$
18. U_{200}	Wind speed at blending height (200 m) above the meteorological station (m/s)	$U_{200} = U_x^* \times \dfrac{(\ln(200/z_0m \text{ at station}))}{0.41}i$
19. U_*	Friction velocity	$U^* = \dfrac{(0.41U_{200})}{(\ln(200/z_0m \text{ at pixel}))}i$
20 rAH	Aerodynamic resistance to heat transport	$rAH = \dfrac{\ln(2/0.01)}{(U_* \times 0.41)}$ where 2 and 0.01 are the heights that dT is measured (z_1 and z_2) i
21. Select dry pixel	Dry pixel for calibration	The Dry Pixel is selected from the image by selecting e.g., the pixel with the lowest NDVI from the subset of pixels with highest T_R[c]
22. Select wet pixel	Wet pixel for calibration	The Wet Pixel is selected from the image by selecting e.g., the pixel with the highest NDVI from the subset of pixels with lowest T_R[c]
23. $T_{R\,Dry}$, $T_{R\,Wet}$	Land surface temperature at the dry pixel, and wet pixel	Imagery
24. a	Calibration coefficient a	$a = \dfrac{dT_{Dry}}{(T_{R\,Dry} - T_{R\,Wet})}i$
25. b	Calibration coefficient b	$b = a \times T_{R\,Wet}$ i
26. dT	Temperature difference between z_1 and z_2 (K)	$dT = a \times (T_{R\,pixel}) - b$
27. T_2	Air temperature at dry pixel	T_R at Dry Pixel for initial value of T_2
28. Air pressure dry (P_a)	Air pressure at dry pixel (hPa); use	$Pa = 101.3 \times \left(\dfrac{T_2 - 0.0065 \times Z_{DryPixel}}{T_2}\right)^{5.26}$ where $Z_{DryPixel}$ is the elevation of the DryPixel; T_2, Air Pressure, and Air Density are iteratively updated in the Monin–Obhukov Iteration, see below[1]
29. ρ_{air}	Air density (kg/m³)	$\rho_{air} = \dfrac{1000 \times Pa}{1.01 \times T_2 \times 287}i$
30. H	Sensible heat flux (W/m²)	$H = \dfrac{(\rho air \times Cp \times dT)}{(rAH)}i$
31. L	Monin–Obhukov length (dimensionless)	$L = \dfrac{-U_*^3 \times T_R}{(0.41 \times g \times H)}i$
32. ψH	Monin–Obhukov correction for heat transport for unstable and neutral atmospheric conditions (L < 0)	$\psi H = 2 \times \dfrac{\ln(1 + x^2)}{2}i$
33. ψM	Monin–Obhukov correction for momentum transport for unstable and neutral atmospheric conditions (L < 0)	$\psi M = 2\ln\left(\dfrac{(1+x)}{2}\right) + \ln\left(\dfrac{(1+x^2)}{2}\right) - \text{ArcTAN}(x) + \dfrac{\pi}{2}$ where $x = \left(1 - 16\left(\dfrac{z}{L}\right)\right)^{1/4}$ i

(*Continued*)

TABLE 3.3 (*Continued*)   Inputs and Calculation Steps for the SEBAL Model

Inputs	Description	Data Source
34. ψH	Monin–Obhukov correction for heat transport for stable atmospheric conditions (L > 0)	$\psi H = -5\left(\dfrac{z}{L}\right)i$
35. ψM	Monin–Obhukov correction for heat transport for stable atmospheric conditions (L > 0)	$\psi M = -5\left(\dfrac{z}{L}\right)i$
36. $U_{\star}$	Friction velocity, corrected with Monin–Obhukov correction	$U_{\star} = \dfrac{\left(U_{200} \times 0.41\right)}{\left(\ln\left(\text{station height}\,/\,z_0 m\right) - \psi M\right)}i$
37. rAH	Aerodynamic resistance to heat transport, corrected with Monin–Obhukov correction	$rAH = \left(\dfrac{\ln\left(\text{station height}\,/\,0.01\right) - \psi H}{\left(U_{\star} \times 0.41\right)}\right)i$
Iteration: Repeat steps 13 through 22 until changes in H are <5%		
38. Λ_{op}	Evaporative fraction at overpass (dimensionless)	$\psi_{op} = \dfrac{\left(Rn - G - H\right)}{Rn - G}i$
39. ET_{24}	24 h evapotranspiration (mm/day)	$ET = \left(\dfrac{86{,}400 \times \Lambda_{op} \times Rn_{24}}{\rho_w \times \lambda}\right)i$
		where ρ_w is density of water (kg/m³), λ is latent heat of vaporization (J/kg).

Source: Bastiaanssen, W.G.M. et al., *J. Hydrol.*, 212, 198, 1998. With permission.

[a] Tasumi (2003).
[b] Gieske (2001).
[c] Messina (2012).

For open water and vegetation without soil moisture limitation, α_{PT} is 1.26, though adjustments may be applied in different environments. λET can be converted to ET in mm by dividing by the latent head of vaporization (λ = 2.45 MJ/kg) (Allen et al., 1998) and an appropriate time constant (e.g., to convert from mm/s to mm/day, κ below).

Three basic approaches are used in the application of (3.4) or (3.5) to estimate actual ET: (1) empirical crop coefficient methods, (2) physically based coefficient methods, and (3) canopy resistance methods. Each of these three methods is reviewed in the following text.

3.2.2.1 Empirical Vegetation Methods: Crop Coefficients

3.2.2.1.1 Calibration Methods

Crop coefficient methods calculate ET as the product of ET_o and a crop coefficient. In the original FAO-56 model of crop ET (Allen et al., 1998), under conditions of soil moisture limitation, the coefficient describing the effect of crop type and growth stage (K_c) is multiplied by a coefficient quantifying the effect of soil moisture stress (K_s) (Allen et al., 1998, Equation 3.81). Most satellite methods estimate the product ($K_c K_s$), which is also sometimes called the reference evapotranspiration fraction (ET_f). In order to simplify notation, and because the method is often used for other vegetation types besides crops; here, we use the term "reference ET fraction" and the symbol ET_f to represent $K_c K_s$ throughout the chapter. Some references refer to the crop coefficient derived from EO data as K_c or K_{c-VI} (Glenn et al., 2011); here, we call it ET_f to be consistent with recent publications (Nagler et al., 2013), to highlight similarities with other methods that use ET_f (Allen et al., 2007) and reduce confusion

of K_c in the original FAO-56 method, which is for conditions of no water stress and estimates potential ET for a given crop, and $ET_f = K_c K_s$, which estimates actual ET and is what EO-based crop coefficient methods determine.

In EO-based method, the crop coefficient is modeled as a function of a vegetation index (VI) using several possible empirical equations (Equations 3.6 through 3.8), including as a power function (Nagler et al., 2013):

$$ET_f = a_K VI^{\eta} \tag{3.6}$$

where
a_K is an empirical coefficient determined by regression
η is a coefficient that varies by the VI

Alternatively, ET_f can be modeled by first normalizing by extreme VI values in the image (Glenn et al., 2010):

$$ET_f = \left[1 - (VI_{max} - VI)\,/\,(VI_{max} - VI_{min})\right]^{\eta} \tag{3.7}$$

where
VI_{max} is the VI value when ET is at a maximum
VI_{min} is the VI of bare soil (VI=0)
η is often close to 1 for some vegetation indices (enhanced vegetation index [EVI], soil-adjusted vegetation index [SAVI]) but may be less than 1 for NDVI due to NDVI's lack of sensitivity for leaf area indices greater than ~3 (Glenn et al., 2011).

Note that this equation assumes evaporation is zero when VI equals VI_{min}, which may not be the case for wet soil, including
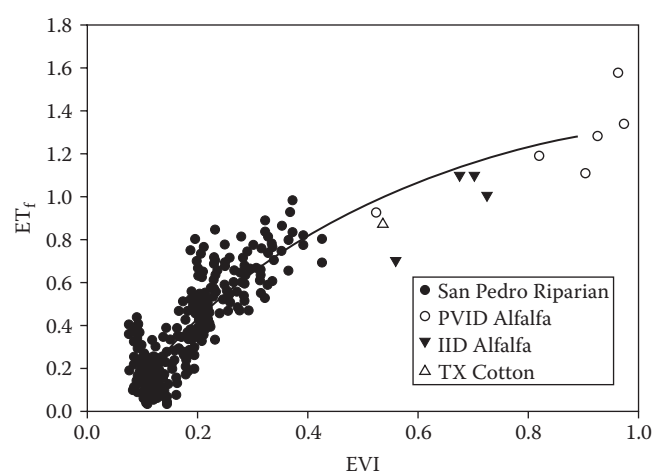
FIGURE 3.1 Reference evapotranspiration fraction from field measurements versus the enhanced vegetation index. The sites span a range of geographic locations (San Pedro River, AZ; Imperial Irrigation district, CA; Palo Verde irrigation district, CA; Texas). The line is the best fit regression line. (Reprinted from Nagler, P.L. et al., *Remote Sens.*, 5, 3849, 2013. With permission from MDPI.)

irrigated fields at initial growth stages. Soil evaporation can be included by introducing a second coefficient K_e that is determined by modeling the soil drying curve after precipitation or irrigation events, which is independent of remote sensing data (Glenn et al., 2010).

Other formulations of the ET_f–VI relationship include those derived from Beer–Lambert law of absorption of light by a canopy, assuming a linear relationship between EVI and LAI (Nagler et al., 2013) (Figure 3.1):

$$ET_f = a_K\left(1 - \exp\left(-b_K EVI\right)\right) - c_K \tag{3.8}$$

where a_K, b_K and c_K the coefficients determined by regression of EVI against observed ET_f in pixels that have ground-level measurements of ET.

The coefficients in Equations 3.6 through 3.8 may vary by crop type, climate, or soil type, so implementation depends on availability of ground data of ET from lysimeters, eddy flux correlation towers, sap flow measurements, or other methods to calibrate the ET_f–VI relationship. If data from lysimeters or towers are used for calibration, the equation estimates ET, and if data from sap flow measurements are used, the equation estimates transpiration only. The method assumes that all crops with identical VI have the same ET_f values. While the coefficients in the ET_f–VI relationship may be constant over several vegetation types (Nagler et al., 2009, 2013), they may vary under different climates, soil types, or soil moisture stress conditions, so the method is typically used to estimate ET over relatively small areas with available data. Regional ET_f–VI curves have been constructed for various locations in the western United States, Spain, and Australia with an accuracy of within 5% of measured values on an annual basis (Nagler

et al., 2013), suggesting the possibility of monitoring ET without field-by-field knowledge of cropping patterns. The spatial and temporal variability in the ET_f–VI relationships and the size region that can be applied with a given accuracy need further documentation.

The accuracy of empirical crop coefficient methods has been assessed using flux towers, soil water balances, and annual water balances. Nagler et al. (2013) reported a standard mean error in ET_f of 0.12 in the application of Equation 3.8 to MODIS EVI data compared to flux towers (riparian areas and irrigated alfalfa) and soil moisture balance (cotton). Glenn et al. (2010), in a review of numerous applications of empirical ET_f methods, report that the empirical methods have root-mean-square deviation (RMSD) in the range of 10%–30% of mean ET across several different biomes. The main disadvantage of the method is the requirement of meteorological data required to estimate ET_o and some ground-level measurements of ET to calibrate the ET_f–VI equation.

3.2.2.1.2 Application of the Crop Coefficient Approach to Agricultural Crops

Bausch and Neale (1987) and Neale et al. (1989) first established the validity of the empirical crop coefficient (ET_f) method at two experimental farm sites in Colorado. They grew irrigated corn in fields equipped with weighing lysimeters, and ET_f was calculated with alfalfa grown at the same facility as the reference crop (i.e., $ET_f = ET_{corn}/ET_{alfalfa}$). NDVI was measured with radiometers suspended over corn canopies. NDVI was strongly correlated with LAI and fractional vegetation cover, and ET_f derived from radiometric measurements closely tracked measured ET_f over the crop cycle. Choudhury et al. (1994) used a modeling approach to show the theoretical justification for replacing ET_f from ground-based measurements with ET_f estimated from a VI, with ET_f from the VI replacing canopy resistance terms in the PM equation. The ET_f method has since been successfully applied to a wide variety of crops as outlined in the following examples.

Vineyards and orchards are difficult to model with normal crop coefficients due to differences in plant spacing and other crop variables among plantings. By using NDVI and SAVI from satellite images, Campos et al. (2010) accurately predicted actual ET by simple linear regression equations in grape orchards in Spain. Samani et al. (2009) used NDVI from Landsat imagery to develop field-scale ET_f values for pecan orchards in the lower Rio Grande Valley, New Mexico, Unites States. Their estimates of ET were within 4% of values measured at an eddy covariance flux tower. Only 5% of fields were within the range of ET and ET_f set by expert opinion, indicating the potential for significant water savings.

Wheat has been extensively studied due to its importance as an irrigated or dryland crop around the world. Duchemin et al. (2006) used NDVI from Landsat images to map LAI and ET in irrigated wheat fields in Morocco and reproduced ground measurements of ET within 15%. Wheat fields varied widely in ET, opening up the possibility of improving irrigation efficiency by

tailoring water applications to actual crop needs determined by satellite imagery. Gontia and Tiwari (2010) developed field-specific crop coefficients for wheat field in West Bengal, India, using ET_f values determined from NDVI and SAVI from satellite sensors.

Extensive work on wheat has been conducted by the USDA Agricultural Research Service in a desert irrigation district in Maricopa, Arizona, United States (Hunsaker et al., 2005, 2007a,b). They developed NDVI-derived ET_f values that tracked within 5% of measured ET_f for wheat grown in weighing lysimeters. Wheat was then grown in field plots for two seasons under stress and nonstress conditions. The NDVI method gave more accurate predictions of actual irrigation demands than the FAO-56 method under all treatment conditions with a root-mean-square error (RMSE) of about 15% of measured water use with no bias toward under or overestimation across treatment.

Similar studies have been conducted with cotton in the southwestern Unites States (Hunsaker et al., 2003, 2005, 2009) and Spain (González-Dugo and Mateos, 2008). The latter study was conducted in a large irrigation district and the results showed that considerable water savings could be achieved by scheduling irrigations based on NDVI-derived crop models rather than ET_f values determined for crops grown under optimal conditions. ET_f methods have been developed for other crops, including potato (Jayanthi et al., 2007), broccoli (El-Shikha et al., 2007), sugar beet (González-Dugo and Mateos, 2008), soybean (Gonzalez-Dugo et al., 2009), the oilseed crop camelina (Hunsaker et al., 2011), sorghum (Singh and Irmak, 2009), and alfalfa (Singh and Irmak, 2009). All these studies reported positive results and pointed to the possibility of considerable water savings by replacing static FAO-56 crop coefficients with locally derived ET_f values.

Often, the main interest is determining district-wide water demand or consumptive use, which requires estimating ET over mixed crop areas. Choudhury et al. (1994) pointed out that the ET_f–VI relationship was not necessarily crop specific and that the ET_f approach might be used over mixed crops without a serious loss of accuracy. Allen and Pereira (2009) found a reasonable agreement between measured ET_f and vegetation cover fraction (f_c) over a wide range of tree crops, and the relationship was improved by including plant height in the regression. Similar findings were reported by Trout et al. (2008) for tree and vegetable crops, and a close correlation was noted between Landsat-derived f_c based on NDVI and f_c measured on the ground over 30 fields with crops ranging from trees (almonds, pistachios), to vines (grapes), and row crops (onions, tomatoes, cantaloupes, watermelon, beans, pepper, garlic, and lettuce. The only aberrant crop was red lettuce, which has a low NDVI due to reflection of red light. They developed an operational ET-monitoring program for California's irrigation districts based on Landsat-derived NDVI and ET_o from the California Irrigation Management Information System's network of micrometeorological stations (Johnson and Trout, 2012).

3.2.2.2 Physically Based Coefficient Methods: PT-JPL Model

For regional or global application, ground reference data are often not available at sufficient spatial density to support local calibration of the ET_f–VI relationship, so more physically based models that require minimum calibration have been developed for large geographic scales. The PT-JPL model of Fisher et al. (2008) estimates ET directly from satellite imagery with minimal ground data requirements. It is a coefficient method in that it estimates coefficients that are multiplied by ET_o to estimate ET, similar to the empirical ET_f method, but using physically based models to estimate the coefficients from satellite imagery and meteorological data. In the PT-JPL algorithm, λET is calculated as the sum of evaporation of water intercepted by the canopy (λE_I), evaporation from the soil surface (λE_s), and transpiration from the dry canopy (λE_c) (Table 3.2), where a "dry canopy" has no liquid water on the surface of the leaves. ET_f for transpiring vegetation is assumed to be the product of four coefficients that account for variations in surface wetness (f_{wet}), green canopy fraction (f_g), a plant temperature constraint (f_T), and a plant moisture constraint (f_M):

$$\lambda ET_c = \left(1 - f_{wet}\right) f_g f_T f_M \alpha_{PT} \frac{s}{s + \gamma}(R_n - R_{ns}) \qquad (3.9)$$

where
  R_{ns} is R_n at the soil surface and is a function of vegetation cover (Table 3.2)

Alternate formulations are available that use fractional vegetation cover without calculating R_{ns} separately (Marshall et al., 2013). The variable descriptions and their equations are listed in Table 3.2. λE_I is calculated as

$$\lambda E_I = f_{wet} \alpha_{PT} \frac{s}{s + \gamma}(R_n - R_{ns}) \qquad (3.10)$$

Soil evaporation (λE_s) is calculated separately but also has coefficients related to surface wetness and soil moisture:

$$\lambda E_s = \left(f_{wet} + f_{SM}\left(1 - f_{wet}\right)\right) \alpha_{PT} \frac{s}{s + \gamma}(R_{ns} - G) \qquad (3.11)$$

Several of the parameters in Table 3.2 may be adjusted according to local conditions. See Fisher et al. (2008) for more detail.

Fisher et al. (2008) compared the PT-JPL model predictions to measurements at FLUXNET eddy covariance towers, and report an RMSE of 16 mm/month and an error in annual ET of 12 mm/yr or 13% of the observed mean. The flux sites covered a range of biomes, including temperate C3/C4 crops but did not include irrigated cropland, which might be expected to have higher error due to high evaporation from inundated and wet soil at the beginning of the growing season (Yilmaz et al., 2014).

3.2.2.3 Physically Based Vegetation Methods: Canopy Resistance and MOD16

Canopy resistance methods predict the resistance parameters in the PM equation (r_a, r_s in Equation 3.4) directly from satellite imagery. Several resistance methods, including MOD16, are based on the model of Cleugh et al. (2007). MOD16 is vegetation based in that the primary inputs driving ET for a given amount of R_n are derived from VI. The fraction of photosynthetically active radiation is used to determine the fraction of the surface covered by crop canopy (f_c) and soil ($1-f_c$). The LAI is used to determine the dry canopy resistance to transpiration (r_{s_c}), the aerodynamic resistance (r_a), and wet canopy resistance to evaporation (r_{s_wetC}).

Dry canopy resistance to transpiration (r_{s_c}) is calculated using LAI, minimum air temperature and vapor pressure deficit:

$$r_{s\_c} = \frac{1}{LAI c_L m(Tmin) m(D)} \qquad (3.12)$$

where

c_L is the mean potential stomatal conductance per unit leaf area

m(Tmin) and m(D) are multipliers (range 0.1–1) that limit stomatal conductance by minimum air temperature (Tmin) and D.

The specific equations for m(Tmin) and m(D) are given in Mu et al. (2007).

3.2.2.4 Vegetation-Based Methods and Soil Evaporation

In both the PT-JPL and MOD16 methods, ET increases with VI. Soil evaporation, including from both saturated and unsaturated surfaces, is assumed to increase with the fourth power of RH (see Table 3.2 and Figure 3.2). In MOD16, evaporation from saturated and unsaturated soils is calculated separately. The water cover fraction or fraction of the soil that is saturated at the

FIGURE 3.2 Soil moisture function.

surface (F_{wet}) is assumed zero in grid cells where RH is less than 70% (0.7) (Mu et al., 2011 Equation 3.15):

$$F_{wet} = \begin{cases} 0.0 & \mid \quad RH < 0.7 \\ RH^4 & \mid \quad RH \geq 0.7 \end{cases} \qquad (3.13)$$

In MOD16, potential evaporation from soils, both saturated and unsaturated, is

$$\lambda E_{SP} = \frac{\left(s(R_n - G) + \left(\rho C_p D / r_s\right)\right)}{s + \gamma \left(1 + r_{tot}/r_s\right)} \qquad (3.14)$$

where

r_{tot} is the total aerodynamic resistance to vapor transport
r_{a_s} is the aerodynamic resistance at the soil surface (Mu et al., 2011)

Total evaporation from both saturated and unsaturated soils, based on a rearrangement of Equation 3.27 in Mu et al. (2011), is

$$\lambda E_s = \lambda E_{SP} \left(F_{wet} + \left(1 - F_{wet}\right) f_{SM}\right) \qquad (3.15)$$

where

f_{SM} is the same as f_{SM} in the PT-JPL method (Table 3.2)

A sample plot for a range of air temperatures shows that soil evaporation as a fraction of potential soil evaporation is very small (<0.2) for RH less than 0.4, particularly at high temperatures (Figure 3.2). At 40°C and RH = 0.5, for example, soil evaporation is less than 0.1 of the potential. The plot highlights the assumption that soil evaporation is predicted to be very low in arid and semiarid environments with low RH and high daytime temperature, since the model assumes that soil evaporation is a function of the regional climate, with more soil evaporation in humid regions. While this assumption may be accurate in rainfed systems, it may be problematic in irrigated areas in arid and semiarid climates, because soil moisture may be high due to irrigation, even if the grid-cell average RH is low. This could be a problem in particular for ET estimation in areas cultivated in rice or other crops that have a significant period of inundation or wet, bare soil.

The authors of the MOD16 algorithm have recognized problems with its performance in irrigated areas and wetland and have updated the algorithm in an application in the Nile River Delta. The revised MOD16 uses radiometric land surface temperature (T_R) to calculate a revised surface resistance to ET (Mu, 2013). In early 2014, NASA has officially approved this as the revised MOD16 product (Mu, 2013), and future evaluations of the algorithm should include irrigated areas and wetlands.

Mu et al. (2011) validated MOD16 against eddy flux covariance towers and report mean absolute bias in daily ET of 0.31–0.40 mm/day, or 24%–25% of observed daily ET when using
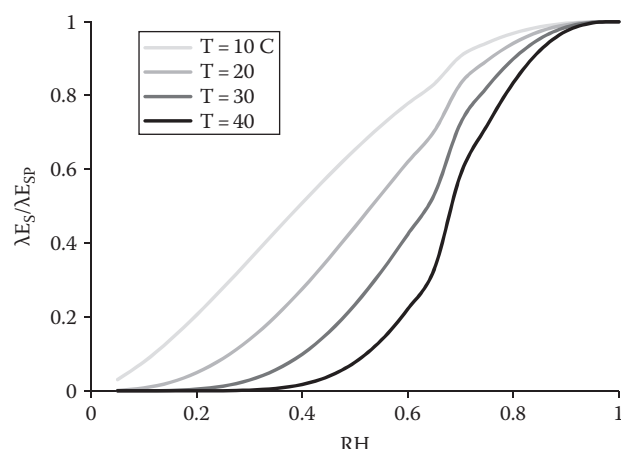
GMAO MERRA for meteorological input. Their flux towers were located in a range of biomes in the United States and at several sites in the Brazilian Amazon. The validation included two irrigated sites, both of which had higher error (1.2 mm/day, 72%–76% of the observed mean) compared to the mean RMSE for all sites with flux tower data.

3.2.2.5 Comparison of Vegetation-Based Methods

Vegetation-based methods have gained great appeal, because they can be run globally and continuously with remote sensing and surface climate reanalysis at low computational cost. The PT-JPL model was evaluated against several other vegetation-based approaches in the humid tropics, given its simplicity and strong dependence on R_n. In regions where light limits carbon assimilation, such as the humid tropics, R_n is the dominant control on λET (Fisher et al., 2009). The PT-JPL model performed best overall, as PM (resistance based) methods include more parameters and therefore may be inherently more uncertain and more strongly coupled to the atmosphere. A comparison of PT-JPL and MOD16 show that PT-JPL overpredicted ET, while MOD16 had lower bias but higher overall error (Chen et al., 2014). Vinukollu et al. (2011a) and Marshall et al. (2013) point out that the performance of these models has been evaluated primarily with eddy covariance flux tower data and their performance can significantly degrade at larger spatial scales, due to the large uncertainties in surface climate reanalysis products, in particular RH.

3.2.3 Radiometric Land Surface Temperature Methods for ET Estimation

Radiometric land surface temperature (T_R) approaches are based on the fact that ET is a change of state of water that uses energy in the environment for vaporization and reduces surface temperature (Su et al., 2005). A subset of these methods is often called energy balance methods, since they solve the energy balance equation using T_R to partition between the sensible and latent heat fluxes; here, we use the more generic term radiometric land surface temperature (T_R) method.

T_R methods have been used as early as the 1970s, when Stone and Horton (Stone and Horton, 1974) used a thermal scanner to estimate ET, and Verma et al. (1976) developed a resistance model with thermal imagery inputs. Since then, a variety of methods has been developed, including SEBAL (Bastiaanssen et al., 1998, 2002), METRIC™, the Surface Energy Balance System (SEBS) (Su, 2002), Atmosphere–Land Exchange Inverse (ALEXI) (Anderson et al., 1997), Disaggregation ALEXI (DisALEXI) (Norman et al., 2003), and operational simplified surface energy balance (SSEBop) (Senay et al., 2013). Most methods in this category use T_R to estimate components of the energy balance, though some simplified methods (e.g., simplified surface energy balance [SSEB]) use temperature directly without solving for the energy balance. In the following text, we summarize the theoretical foundations of the energy balance methods, describe simplified approaches based on T_R, and highlight key differences in the most used algorithms.

In energy balance methods that use T_R, λET is computed as a residual of the energy balance equation:

$$\lambda ET = R_n - G - H \tag{3.16}$$

where
   G is soil heat flux
   H is the sensible heat flux (all in W/m^2)

While there may be some energy exchange from photosynthesis, it is usually a small fraction of R_n, is not easily measured even by ground instrumentation (Wilson et al., 2001), and is assumed to be zero (Meyers and Hollinger, 2004). In vegetation having significant amount of canopy, such as forests, energy exchange from photosynthesis can become high (7%–15%), particularly over short time intervals (Meyers and Hollinger, 2004).

The most important term in the energy balance equation after R_n–G is H, which can be estimated using either one- or two-source models (TSM) (Figure 3.3). One-source models, including SEBAL (Bastiaanssen et al., 1998), METRIC (Allen et al., 2007), and SEBS (Su, 2002), estimate evapotranspiration from the surface as a whole. TSM (ALEXI/DisALEXI) (Anderson et al., 1997) separate ET into E from soil and ET from the vegetation canopy, which is sometimes further separated into evaporation of intercepted water from a wet canopy and transpiration from a dry canopy as in the PT-JPL and MOD16 models. The separation into two sources results in two additional resistance variables that need to be estimated: Rx, the total boundary layer resistance of the canopy, and Rs, the sensible heat exchange resistance of the soil surface (Figure 3.3).
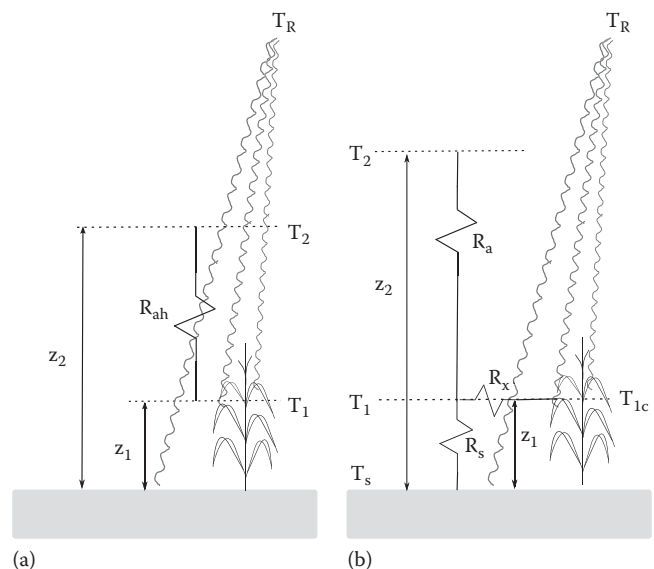

FIGURE 3.3 Schematic of one (a) and two-source (b) models for temperature-based ET calculations. T_R is the radiometric surface temperature detected at the satellite, and the grey lines indicate thermal radiation emission from the soil and canopy.

3.2.3.1 One-Source Models: SEBAL, METRIC, and SEBS

In one-source models (Figure 3.3) H is calculated as

$$H = \frac{\rho_{air} C_p \left(T_1 - T_2 \right)}{R_{ah}} \qquad (3.17)$$

where

ρ_{air} is the density of air (kg/m^3)
C_p is the specific heat of air (J/kg/K)
T_1 is the aerodynamic temperature (K) of the evaporating surface at height z_1

which is the height of the zero-plane displacement (d) plus the surface roughness for momentum transport (z_{0m}), T_2 is the air temperature at height z_2, which is usually the height where air temperature is measured (2 or 3 m above the evaporating surface), and R_{ah} is the aerodynamic resistance to turbulent heat transport from z_1 to z_2 (Figure 3.3). The model assumes that evaporating surfaces have a temperature equal to or hotter than the air above ($T_1 \geq T_2$), resulting in a nonnegative sensible heat flux. The zero-plane displacement height (d) is the mean height where momentum is absorbed by the canopy, typically around 2/3 of the vegetation height (h), and z_{0m} is a relatively small fraction of the height of vegetation (0.03–0.1 h, or 0.123 h in Morse et al., 2000), and so is around 0.03 m over grassland, 0.10–0.25 m over cropland, and 0.5–1.0 m over forest or shrubland. In practice, z_{0m} is estimated as a function of NDVI or with a land cover map (see Table 3.3).

There are two main uncertain variables in the calculation of H in Equation 3.17. First, the radiometric surface temperature (T_R) may differ from the actual aerodynamic temperature (T_1). Note that neither of the air temperatures in Equation 3.17 are directly sensed by the satellite, which estimates the radiometric surface temperature (T_R) based on thermal radiation reaching the sensor from the combined soil and canopy surfaces. The correspondence between T_R and air temperatures at either z_1 or z_2 varies by surface type, roughness, and crop canopy structure. Different one-source models have different strategies for estimating the temperature difference between z_1 and z_2. Some models include an extra term in R_{ah}, while others (e.g., SEBAL, METRIC) calibrate an empirical linear model relating T_1–T_2 to T_R. Second, R_{ah} has high spatial variability and may be difficult to predict.

In one-source models (SEBAL, METRIC, SEBS), a linear equation predicts the difference between T_1 and T_2 as a function of the radiometric surface temperature (Figure 3.4 and Table 3.3):

$$T_1 - T_2 = a + bT_R \qquad (3.18)$$

where a and b are empirical parameters determined from the imagery in a process called "internalized calibration" (Allen et al., 2007).

Field investigations suggest that Equation 3.18 holds under a variety of conditions (Figure 3.4). Note that in applications of
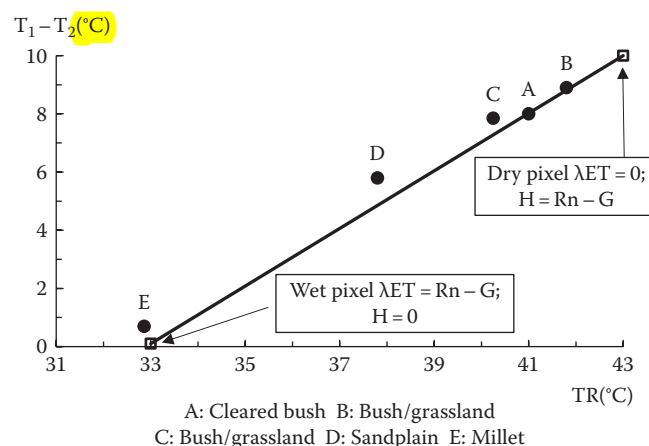

A: Cleared bush B: Bush/grassland
C: Bush/grassland D: Sandplain E: Millet

FIGURE 3.4 Example of the assumption of the linear relationship between radiometric temperature (T_R) and the temperature difference between heights z_1 and z_2. Data are from Bastiaanssen (1998), and dry and wet pixels are added for illustration. (Reprinted from *J. Hydrol.*, 212–213, Bastiaanssen, W.G.M., Menenti, M., Feddes, R.A., and Holtslag, A.A.M., A remote sensing surface energy balance algorithm for land (SEBAL) 1. Formulation, 198–212, Copyright (1998) with permission from Elsevier.)

the method, a and b are determined from the wet and dry pixels only, with no field data of air temperatures for calibration and therefore no estimate of error of Equation 3.18.

Combining Equation 3.17 with Equation 3.18 gives

$$H = \frac{\rho_{air} C_p \left(a + bT_R \right)}{R_{ah}} \qquad (3.19)$$

Identifying the parameters a, b, and R_{ah} requires calculating ρ_{air} and C_p (Table 3.3) and identifying some pixels where H and T_R are known. First, one pixel is selected that is "wet," where H is assumed to be 0 and λE is assumed R_n–G, and another that is "dry," where H is assumed to be R_n–G and λE is assumed to be 0 (Figure 3.4). An initial guess of R_{ah} is made for the image based on literature values by land cover type. An initial guess of T_1–T_2 is made at the dry pixel by solving for it in Equation 3.17, using the assumption H = R_n–G. Coefficients a and b in (3.18) are then determined from the observed T_R and estimated T_1–T_2 at the wet and dry pixels (Table 3.3). H is then calculated again using (3.19), this time accounting for unstable atmospheric conditions using the Monin–Obukhov equations (Table 3.3) (Allen et al., 2011; Bastiaanssen et al., 1998, 2002). The values of a, b, and R_{ah} are then solved iteratively by updating the values of each until the result converges on H = 0 for the wet pixel and H = R_n–G for the dry pixel. The internal calibration of SEBAL and METRIC allows estimation of ET without knowing either T_1 or T_2, which is an advantage in data-scarce regions.

Sensitivity analysis suggests that T_R at the hot and cold pixels are the most important controls on H and λET estimates for a given image, followed by R_n at the hot pixel (Long et al., 2011). Since H is assumed to be zero at the cold pixel, R_n at the cold pixel does not influence the resulting model parameters and

calculated H. The criteria for pixel selection are important, but there is no generally agreed method for selecting them (Long et al., 2011). Past applications of SEBAL and METRIC have used manual pixel selection, since user experience in the study area helps select the appropriate pixels that represent typical field conditions in the image, but manual pixel selection can add significantly to the processing time. The selection procedure can be automated, which reduces variability among users and allows for more rapid implementation (Kjaersgaard et al., 2009; Messina, 2012). In the automation algorithm of Long et al. (2011), the dry pixel is the pixel with the highest T_R in the subset of pixels with specified land use (bare, urban, or dry cropland), and the wet pixel is the pixel with the lowest T_R, after screening for cloud contamination. Automation of pixel selection in METRIC (Allen et al., 2013) uses a combination of NDVI, T_R, and α. Other semiautomated approaches simply select the highest and lowest T_R in a given image, using masks to exclude either clouds or nonrepresentative land covers. The reasons for excluding certain land covers for the wet and dry pixel selection are often not explicit and vary by application. For the wet pixel, some studies advocate excluding water bodies since they have different aerodynamic properties than agricultural fields where ET is being estimated (Conrad et al., 2007; Morse et al., 2000), while others include water bodies, particularly if vegetated pixels have much higher temperatures than open water bodies. For dry pixels, some studies exclude urban environments (Conrad et al., 2007), while others include them (Long et al., 2011). The impact of different selection rules, including which surfaces should or should not be included, has not been determined for a range of surface types and geographic regions.

One-source models have the convenience of being relatively simple to use and are calibrated to wet and dry pixels, reducing the need for meteorological data. However, the calibration is performed on a single image, and the a and b parameters from Equation 3.19 may only be valid for that image. While this may not be a problem for study areas, the size of a single scene, areas that cover multiple scenes may suffer from problems of merging along scene boundaries. To the authors' knowledge, at the date of publication, there have not been any efforts to determine the spatial and temporal variability in the a and b parameters or evaluations of the extent and magnitude of scene boundary problems. The SSEBop model (Section 3.2.3.1.1) was designed to address scene boundary problems by estimating T_1–T_2 for each pixel under dry and wet conditions.

AQ4

Summaries of the accuracies of SEBAL are available in Bastiaanssen et al. (2005) and Kalma et al. (2008), with numerous case studies (Teixeira et al., 2009). In general, the reported errors are higher for smaller spatial scales and small time intervals and are within the errors of measurements of the device used for validation, which is typically 10%–15%. Reported accuracies from numerous validation exercises using point- and field-scale instruments suggest that one-source models have errors around 50 W/m², or a maximum error of around 15%–30% for daily estimates (Kalma et al., 2008), though the errors may vary with the spatial resolution of the input data. Errors over long time scales,

including the seasonal estimates of importance to water managers and assessments of water productivity, are typically lower (RMSE ~5%) due to cancelling out of daily errors (Bastiaanssen et al., 2005).

Most validation sites, both for SEBAL/METRIC and for EO-based ET methods in general, are located in relatively large plots of homogeneous vegetation, which facilitates comparison with satellite imagery but may not assess accuracy well over heterogeneous landscapes. SEBAL, for example, assumes minimal advection of energy among pixels, which is likely valid over large homogenous vegetation but may not be valid in heterogeneous irrigated landscapes in semiarid and arid climates. Advection may double the amount of ET in situations of extreme humidity gradients and high winds (Allen et al., 2011), which motivated the use of ET_o and ET_f in METRIC in place of R_n–G as used in SEBAL. For small irrigated plots in semiarid or arid climates, the assumption of no advection may be especially problematic, though this has not been systematically quantified using one-source models.

Water balance measurements have also been used to validate remotely sensed ET at the scales of individual fields, watersheds, or irrigation projects (Bastiaanssen et al., 2002, 2005). Validation using water balances at the watershed scale is difficult in rainfed systems in arid and semiarid environments, since streamflow as a percentage of precipitation is often within the error of ET estimated by any method. Water balance validation is more feasible in surface irrigated systems, where inflows and outflows are large relative to ET (Bastiaanssen et al., 2002).

3.2.3.2　Two-Source Models: ALEXI and DisALEXI

TSMs account for the differences in aerodynamic resistance between soil and vegetation, which are lumped into a single resistance parameter in single-source models. TSMs require estimation of the energy balance and therefore of T_1 and T_2 over vegetation and soil separately and so cannot use internal calibration to wet and dry pixels. One popular TSM, the ALEXI model uses the two-source energy balance model (TSEB) of Norman et al. (1995). In ALEXI, T_1 of the soil (T_{1s}) and canopy (T_{1c}) are estimated by separating radiometric temperature (T_R) by the vegetation cover fraction:

$$T_R = \left[f_c T_{1c}^{\,4} + (1 - f_c T_{1s}^{\,4}) \right]^{1/4} \qquad (3.20)$$

where f_c is the fractional vegetation cover at a given view angle, calculated as

$$f_c = 1 - \exp\left(\frac{-0.5\Omega LAI}{\cos(\theta)} \right) \qquad (3.21)$$

where

  Ω is an index of the degree of clumping from the given view angle
  θ is the view angle

T_2 is estimated using an atmospheric boundary layer (ABL) model (Anderson et al., 2013) calibrated to the observed increase in temperature during the morning hours (from 1 to 1.5 h after sunrise to before local noon), which is obtained from geostationary satellites such as the geostationary operational environmental satellite (GOES) (Anderson et al., 2013). Like SEBAL, the use of temperature difference instead of absolute temperature avoids the need for in situ measurements of air temperatures or estimates of atmospheric corrections and is a significant advantage in data-scarce regions. The ABL model used in ALEXI is a relatively simple one that can be programmed as a system of equations.

The spatial resolution of the ALEXI model is constrained by the resolution of geostationary satellites (5–10 km), so a different algorithm, DisALEXI, uses higher-resolution imagery from MODIS (1 km) or Landsat (30 m) to generate high-resolution ET estimates using ALEXI results (Norman et al., 2003). DisALEXI utilizes the temperature and wind speed at the blending height (~50 m above the land surface) and downwelling short- and longwave radiation from ALEXI as input, assuming those four variables are spatially uniform over the resolution of the ALEXI model (usually 5–10 km). The high-resolution thermal imagery is then adjusted to the view angle of the GOES satellite to ensure consistency in the radiometric temperature. The angle-adjusted radiometric temperature, vegetation cover, and land use maps from the high-resolution imagery are then used to calculate R_n at high resolution, and the TSM run on each high-resolution pixel with the ALEXI-derived temperature at 50 m as the upper boundary condition (Norman et al., 2003). The DisALEXI values are adjusted to match the mean ALEXI values by iteratively altering the air temperature map (T_2) until the aggregated DisALEXI values match the ALEXI ET values, ensuring consistency across scales.

Methods for fusing DisALEXI results with MODIS for daily resolution and with Landsat for high spatial resolution have been developed and tested over rainfed (Cammalleri et al., 2013) and irrigated areas (Cammalleri et al., 2014), based on a data fusion strategy for MODIS and Landsat (Gao et al., 2006). The spatial and temporal adaptive reflectance fusion model finds the date with the highest correlation between Landsat- and MODIS-derived ET and uses that correlation structure to predict Landsat-scale ET on dates with only MODIS data available (Figure 3.5). The use of MODIS improves the estimation of ET over the use of a simple spline function on ET using available Landsat dates. The results highlight the importance of having daily MODIS estimates for some locations where vegetation responds to changes in moisture (Figure 3.6). At some sites (162), little difference was observed between the interpolated Landsat ET and the MODIS–Landsat fusion product, but at other sites (161), ET increased rapidly and was higher than the interpolated Landsat values for a 15–20 day period following a rainfall event, showing the importance of high-temporal-resolution data in certain parts of the time series.

3.2.3.2.1 Other TSM Models

Another TSM model, the dual-temperature-difference (DTD) model (Norman et al., 2003) was based on the time rate of change in T_R and T_2, where the equations in ALEXI model
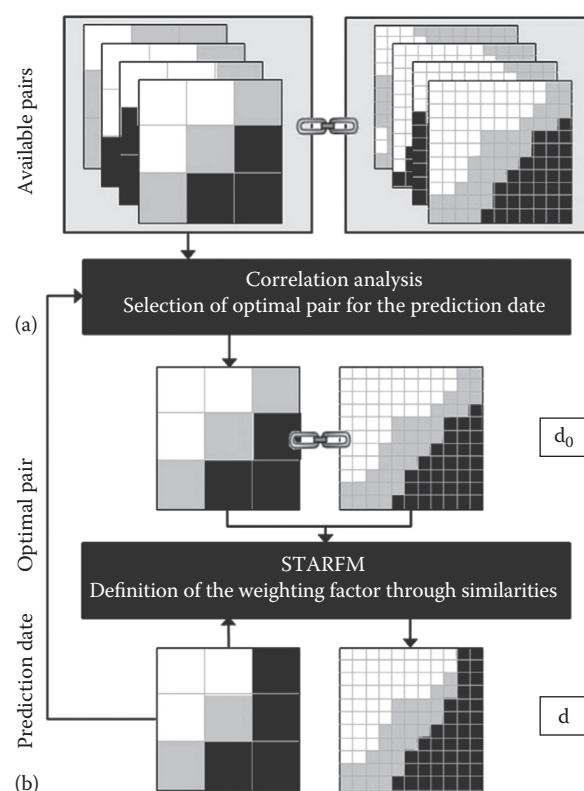

FIGURE 3.5 Schematic of the STARFM method for fusing MODIS and Landsat imagery for high spatial and temporal resolution of ET. (Reprinted from *Agric. Forest Meteorol.*, **186,** Cammalleri, C., Anderson, M.C., Gao, F., Hain, C.R., and Kustas, W.P., Mapping daily evapotranspiration at field scales over rainfed and irrigated agricultural areas using remote sensing data fusion, 1–11, Copyright (2014), with permission from Elsevier.)

(Anderson et al., 1997) were used to form a dual-difference ratio of radiometric and air temperatures. The H flux is then calculated from temporal measurements of T_2, T_R, and wind speed. An ABL model was not required in implementing the model, so the calculations can be made efficiently with minimal ground-based data. Various studies have evaluated the ability of DTD TSM for deriving surface heat fluxes over dissimilar testing conditions. Generally, those studies have indicated an agreement between the model-predicted λET and corresponding ground observations in the order of ~50 W/m^2 (Gowda et al., 2008).

Sun et al. (2009) proposed another TSM energy balance model, the simple remote sensing evapotranspiration model (Sim-ReSET). The major difference in their model compared to other TSMs was that the aerodynamic resistance (R_{ah}) was calculated using a reference dry bare soil and canopy height, assuming homogeneous wind speed in the upper boundary layer. Unlike ALEXI, Sim-ReSET is based on a single image, and, like SEBAL and METRIC, is based on internal calibration to dry soil and wet vegetated pixels. Evaluation of Sim-ReSET was performed for a region in north China using MODIS data. Comparisons of the predicted λET fluxes by Sim-ReSET versus concurrent ground
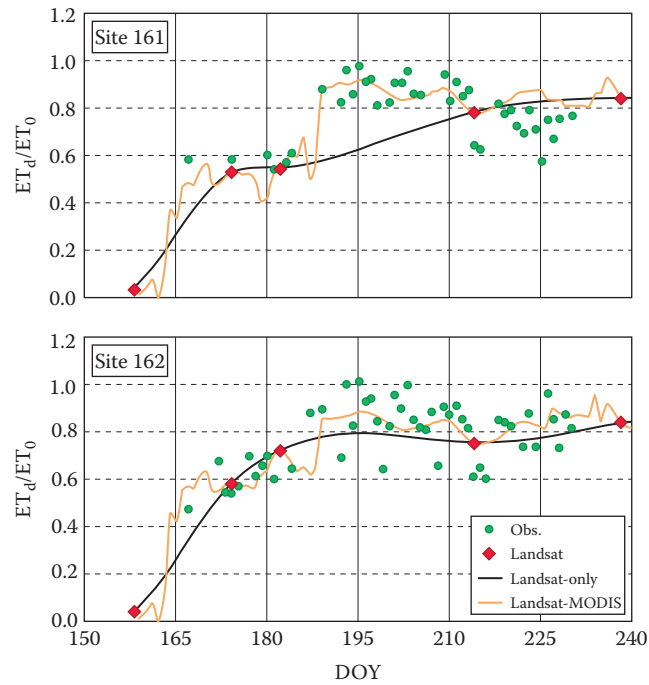
FIGURE 3.6 Time series of ET/ET_o estimated using Landsat alone and using MODIS downscaled to Landsat resolution using the STARFM algorithm over rainfed soybeans in Iowa. (Reprinted from Cammalleri, C., Anderson, M.C., Gao, F., Hain, C.R., and Kustas, W.P., A data fusion approach for mapping daily evapotranspiration at field scale, *Water Resour. Res.*, 49, 4672–4686, 2013. With permission from American Geophysical Union.)

measurements from 12 experimental days showed a RMSD for instantaneous values of ~42 W/m² and a MAE of 34 W/m². Error in the mean daily ET over a 6 day period was lower (MAD = 0.26 mm/day, RMSD = 0.30 mm/day) as observed in other applications. Two of the key advantages of Sim-ReSET were that it avoids the direct computation of the aerodynamic resistance and that all the model inputs required can be estimated from remote sensing data alone.

3.2.3.3 Simplified T_R-Based Approaches: SSEB and SSEBop

Several other T_R-based methods have been developed, including the SSEB model (Senay et al., 2007). Similar to the crop coefficient methods in Section 3.2.2.1., SSEB calculates ET as the product of ET_o (Equations 3.4 or 3.5 and ET_f. The SSEB model assumes that ET_f for a given pixel can be estimated from the radiometric temperatures at the hot, cold, and observed pixels alone, without explicitly solving the energy balance equation:

$$\text{ETf} = \frac{(T_h - T_R)}{(T_h - T_c)} \tag{3.22}$$

where

T_h is the radiometric temperature of the hot pixel
T_c is the radiometric temperature of the cold pixel

Since the maximum ET of a crop with a high LAI may be higher than that of the reference grass, the ET_o parameterized for the reference grass is multiplied by a correction factor, usually 1.2 (Senay et al., 2007). Similar to other energy balance methods, the temperatures at the hot and cold pixel are derived from the image, assuming that pixels where ET = 0 and ET = 1.2ET_o exist in the image.

While the original formulation of SSEB is easy to implement and produces estimates for regions with a uniform hydroclimate such as irrigated districts, an improvement was necessary to account for land surface temperature differences caused by spatial variation in elevation and albedo. An enhanced version of SSEB was introduced by Senay et al. (2011) to adjust the radiometric temperature using a lapse-rate correction before using it in Equation 3.22. A similar lapse-rate adjustment is also performed in other temperature-based methods, including SEBAL and METRIC. A comparison between the enhanced SSEB and METRIC showed a strong relationship at elevations below 2000 m (R^2 = 0.91) compared to elevations lower than 2000 m (R^2 = 0.52) in Central Idaho (Senay et al., 2011). The original SSEB model also calculates ET_o using a fixed value for α (0.23). While SW↓, LW↓, and LW↑ can vary by pixel under the original SSEB method, using the fixed α ignores the impact of spatial variability in α and G on ET, which could result in overestimation of ET at pixels with high albedo and overestimation of ET at pixels with high and positive G. An improved version of SSEB (Senay et al., 2011) adjusts ET_f by a factor that varies with NDVI, and ranges from 0.65 to 1.0 (Equation 3.6 in Senay et al., 2011). The adjustment is designed to account for generally higher albedo and greater ground heat flux for in pixels with low NDVI, though the relationship between the adjustment factor and NDVI may vary geographically and is not derivable from other measurements.

The SSEB model requires the selection of hot and cold pixels in the image, as in the SEBAL and METRIC models. This selection process generally inhibits operational application of such models over large areas and introduces problems along scene boundaries. The SSEBop ET algorithm is an operational parameterization of the SSEB model (Senay et al., 2007), renamed SSEBop because of its operational capability (Senay et al., 2013) (Table 3.4). SSEBop proposes that the hot and cold temperatures can be determined separately for each pixel, rather than for each image. The dry-minus-wet temperature difference (T_h–T_c = dT) is calculated for each day and pixel by assuming G is zero for a dry surface (R_n = H, ET = 0) and solving the Equation 3.17 for dT for dry conditions:

$$T_h - T_c = dT = \frac{R_n \times R_{ah}}{\rho_{air} \times C_p} \tag{3.23}$$

where the variable definitions are the same as those in Equation 3.19. R_{ah} is assumed to have a constant value of 110 s/m, which corresponds to a bare, dry soil based on model inversion to field data in the western United States (Senay et al., 2013).

TABLE 3.4 Inputs, Parameters, Steps, and Equations Used in the SSEBop Model

No	Inputs	Units	Description	Data Source
1.	T_R	K	Radiometric surface temperature	Satellite imagery (Landsat, MODIS)
2.	T_2	K	Air temperature	PRISM
3.	R_n	W/m^2	Clear-sky net radiation	Allen et al. (1998)
4.	R_{ah}	s/m	Aerodynamic resistance	Constant value (110)
5.	R	J/kg K	Specific gas constant	Constant value (287)
6.	C_p	J/kg K	Specific heat of air at constant pressure	Constant value (1013)
7.	ET_o	mm/day	Reference evapotranspiration	Penman–Monteith Equation
8.	NDVI	—	Normalized difference vegetation index	Satellite imagery (Landsat, MODIS)
9.	Z	m	Surface elevation	Digital elevation model (DEM)
10.	T_{R_cold}	K	T_R at a cold pixel	Satellite imagery (Landsat, MODIS)

Steps	Parameters	Units	Description	Equation
1.	c	—	Temperature correction coefficient	$c = \dfrac{T_{R\_cold}}{T_2}$
2.	P	kPa	Atmospheric pressure	$P = 101.3\left(\dfrac{293 - 0.0065 \times Z}{293}\right)^{5.26}$
3.	T_{kv}	K	Virtual temperature	$T_{kv} = 1.01(T_2 + 273)$
4.	ρ_{air}	kg/m^3	Density of air	$\rho_{air} = \dfrac{1000P}{T_{kv}R}$
5.	dT	K	Temperature difference	$dT = \dfrac{R_n R_{ah}}{\rho_a C_p}$
6.	T_c	K	Cold reference temperature	$T_c = cT_2$
7.	T_h	K	Hot reference temperature	$T_h = T_c + dT$
8.	ET_f	—	Reference ET fraction	$ET_f = \dfrac{(T_h - T_R)}{dT}$
9.	ET	mm	Actual evapotranspiration	$ET = ET_f \times ET_o$

Source: Senay, G.B. et al., *JAWRA J. Am. Water Res. Assoc.*, 49, 577, 2013. With permission.

The constant value of R_{ah} is used for all pixels regardless of actual cover, because dT represents the temperature difference between a hypothetical bare, dry soil surface, and a well-vegetated surface at each pixel. dT generally ranges between 5 and 25 K depending on location and season.

SSEBop assumes that the theoretical cold–wet surface temperature of a given pixel can be estimated using the air temperature, T_2 as

$$T_c = c \times T_2 \tag{3.24}$$

where
   T_2 is the air temperature obtained from a meteorological station or gridded meteorological data
   c is a temperature correction factor estimated as the ratio of T_R to T_2 at the time of overpass for a well-vegetated wet surface (high *NDVI*; the specific threshold will depend on the NDVI used).

In previous applications of SSEBop, c is close to 1 (Senay et al., 2013). Equation 3.24 is based on the same premise as the SEBAL and METRIC algorithms, where H = 0 at a cold pixel. When the air temperature corresponding to the satellite overpass is not available, daily maximum air temperature can be used, and c

calculated as the ratio of daily maximum air temperature and daily temperature. The use of daily maximum air temperature offers an advantage when modeling over large areas (such as regional to global modeling) as exact time of satellite overpass could be different for different locations.

Once dT and T_c are calculated, the theoretical surface temperature under hot and dry conditions can be estimated for each pixel as $T_h = T_c + dT$. This simplification permits the estimation of ET_f as

$$ET_f = \frac{(T_h - T_R)}{dT} \tag{3.25}$$

Evapotranspiration at a given pixel λET is calculated by multiplying ET_f by ET_o. The advantage of this approach is the simplification of the model that enables operational application over large areas and limited data requirements. SSEBop relies on the accuracy of the T_R and dT estimation, so it can produce inaccurate ET estimates on surfaces with high albedo and emissivity values that are different from the soil-vegetation complexes found in agricultural settings. To improve the accuracy of ET estimates, please refer to Senay et al. (2013) for suggested methods to condition T_R over surfaces with high albedo and emissivity.

3.2.3.4 From Instantaneous to Daily ET

Temperature- and energy-based methods provide instantaneous estimates of ET, but instantaneous estimates may be of little use for mapping seasonal crop water use (Petropoulos, 2013). Several approaches may be used to calculate daily total ET from the instantaneous imagery (Crago, 1996; Chávez et al., 2008; Kalma et al., 2008; Petropoulos, 2013), though two types of methods are most commonly applied: the evaporative fraction method and the crop coefficient method. The evaporative fraction (Λ) approach uses the satellite-derived ET to calculate ET as a fraction of available energy (R_n–G):

$$\Lambda_{op} = \frac{\lambda E}{Rn - G} \qquad (3.26)$$

The evaporative fraction at the time of overpass (Λ_{op}) is assumed equal to Λ for the daytime (Λ_d) or during a 24 h period (Λ_{24}). Either daytime or 24 h total ET is calculated as the product of Λ_{op} and the daytime net available energy (R_n–G) or 24 h net radiation (Rn_{24}), since G is assumed to be zero over 24 h. The assumption that Λ_{op} equals Λ_d or Λ_{24} is justified by some field measurements (Hall et al., 1992; Jackson et al., 1983), though clouds can change the temporal stability of Λ (Crago, 1996), and modeling studies suggest there may be diurnal variation in Λ, with minimum values during midday that can result in underestimation of the daily mean Λ of up to 20%–40% when using overpass times between 11 am and 3 pm (Gentine et al., 2007; Lhomme and Elguero, 1999). Clouds reduce R_n–G, but typically, H decreases more than λE, resulting in an increase in Λ during cloudy periods, though this difference was not statistically significant in field studies, and the assumption of constant Λ over daytime hours is "surprisingly robust" (Crago, 1996). Other studies suggest that a correction factor should be applied that varies with time of overpass and soil moisture (Gentine et al., 2007), though in practice, a constant Λ is often assumed.

Either daytime available energy (R_n–G) or 24 h total net radiation (R_{n24}) is used as the multiplier to calculate total ET from Λ_{op}. R_{n24} is most commonly used to estimate ET_{24} given the (near) zero G term, though Van Niel et al. (2011) caution that, in addition to the assumption that the evaporative fraction is constant over a 24 h period, the use of R_{n24} also assumes that net available energy (R_n–G) and latent heat flux (λET) are zero or near zero at night (Van Niel et al., 2011). R_n–G is commonly negative at night due to longwave emission from the surface. While the latent heat flux can also be negative at night, corresponding to condensation or dew formation, much of the negative available energy changes the sensible heat flux rather than the latent heat flux. The latent heat flux can also be positive at night if sensible heat is advected onto a given location, which can occur where irrigated vegetation may have heat advected to it from surrounding hotter rainfed vegetation. In an irrigated alfalfa plot, nighttime ET was >7% of total daily ET (Tolk et al., 2006). This zero or positive nighttime latent heat flux can result in significant underestimation of daily ET when using R_{n24}, of up to –24% to –38% when using the midmorning value of Λ_{op} and lower errors when

using midafternoon values (–5% to –21%). The main contributor to the error of using R_{n24} was the nonzero nighttime available energy flux, which was sometimes nearly equal to the daytime available energy in a wet forest site (Van Niel et al., 2011). The error was smaller at a drier savanna site. More documentation is needed about how the magnitude of errors incurred by using R_{n24} instead of (R_n–G)d to calculate daily ET depends on season, climate, and vegetation.

Other methods, including the original METRIC model (Allen et al., 2007), use the crop coefficient approach, which calculates the ratio of actual to reference ET at the time of satellite overpass, then multiplies that fraction by reference ET for the day:

$$ET_{24} = C_{rad} \times ETf \times ET_{o24} \qquad (3.27)$$

where ET_{24} is ET over the 24 h period, C_{rad} is an adjustment applied to sloped surfaces, ET_f is the ratio of actual to reference ET at the time of satellite overpass, and ET_{o24} is reference ET for the 24 h period. C_{rad} is likely to be close to 1 for most crops, which are mostly grown on flat surfaces, but there may be local exceptions for agroforestry crops in mountainous terrain.

The crop coefficient method was advocated over the Λ method by Allen et al. (2007) who suggested that advection, which is not included in the Λ method, is important for heterogeneous irrigated landscapes and is accounted for by the PM equation. A review of field studies suggested that ET_f is relatively constant over a 24 h period in irrigated plots (Romero, 2004, cited in Allen et al., 2007). In one comparison study, the evaporative fraction method had a lower RMSE (7.0%) than the crop coefficient method (16.6%) (Chávez et al., 2008), but the accuracies of each method likely change with meteorological conditions, vegetation, and soil moisture.

3.2.3.5 Comparison of Temperature-Based Methods

As energy balance methods gained popularity for their simplicity and accuracy in measuring energy fluxes across landscapes, the merits of one-source and two-source approaches were scrutinized. Timmermans et al. (2007) compared two common energy-based methods: one-source (SEBAL) and TSM (ALEXI). SEBAL accuracy declined over hot, dry, heterogeneous terrain, because of the difficulty in selecting a dry end member pixel within the boundaries of the remote sensing image, which is then used to calibrate Equation 3.18. TSM, on the other hand, which rely heavily on vegetation fraction, tended to be less accurate in densely vegetated areas, where small changes in vegetation cover can have significant impact on canopy temperature estimation. Other studies suggest that TSM may perform better in conditions of either dense or sparse vegetation, or extremes of soil moisture (Anderson et al., 2013, p. 212), and field-scale comparisons suggest that TSM outperforms single-source models (Gonzalez-Dugo et al., 2009), though both were found to produce acceptable results.

Gonzalez-Dugo et al. (2009) used data collected during the SMACEX/SMEX02 field experiments (Kustas et al., 2005) to evaluate instantaneous λET fluxes derived from an empirical one-layer energy balance model (Chávez et al., 2005), METRIC

(Allen et al., 2007), and the TSM of Kustas and Norman (1999), the latter being an updated version of the Norman et al. (1995) TSM model that forms the basis of ALEXI. The authors reported a RMSD of less than 50 W/m² and less than 33 W/m² in the estimation of the instantaneous λET and H fluxes, respectively, by all methods. The fluxes predicted by the TSM of Kustas and Norman (1999) had the closest agreement to the ground observations (RMSD of 30 W/m², R² = 0.83), followed by METRIC (RMSD of 42 W/m², R² = 0.70), and last by the empirical one-layer model (RMSD of 50 W/m², R² = 0.70). Gonzalez-Dugo et al. (2009) underlined as a major disadvantage of both the TSM and the empirical one layer model the requirement of both models for accurate emissivity and atmospheric correction of the thermal-infrared (TIR) imagery used subsequently for computing the land surface temperature. METRIC had a very important disadvantage in the requirement for scene internal calibration each time, which, although it reduces the need for accurate temperature retrieval, significantly diminishes the use of this model for operational application and introduces subjectivity in the pixel selection, though recent advances at automated pixel selection may reduce problems with application and subjectivity. Gonzalez-Dugo et al. (2009) also evaluated the performances of three modeling schemes for interpolating instantaneous to daily fluxes. The schemes evaluated included the Λ method (Crago, 1996), the adjusted Λ method (Anderson et al., 1997), and the reference evapotranspiration fraction (Doorembos and Pruitt, 1977—in Gonzalez-Dugo et al., 2009). Authors reported similar accuracy among the three models. The daily λET fluxes by the adjusted Λ method returned the closest agreement to the reference measurements (RMSD = 0.74 mm/day, R² = 0.76). The daily λET fluxes predicted by the reference evapotranspiration method were found to be overestimated during conditions of prolonged dry down period.

Senay et al. (2011) compared λET fractions derived from SSEB and METRIC models. The comparison study was carried out using Landsat images acquired for South Central Idaho during the 2003 growing season. Results indicated that SSEB model compared well with METRIC model output. However, SSEB model was more reliable over wide range of elevation (especially >2000 m) to detect anomalies in space and time for water resources management and monitoring such as for drought early warning systems in data scarce regions.

3.2.4 Scatterplot-Based Methods for ET Estimation

Scatterplot methods, also called triangle methods (Gillies et al., 1997) or trapezoidal methods (Moran and Jackson, 1991), combine features of the vegetation-based and energy-based methods. Like the vegetation-based methods, they use a VI but also incorporate T_R to account for spatial variability in soil evaporation and in evaporation from vegetation experiencing different levels of soil moisture stress. They are based on the relationships between T_R and some other satellite-derived variable, often a VI
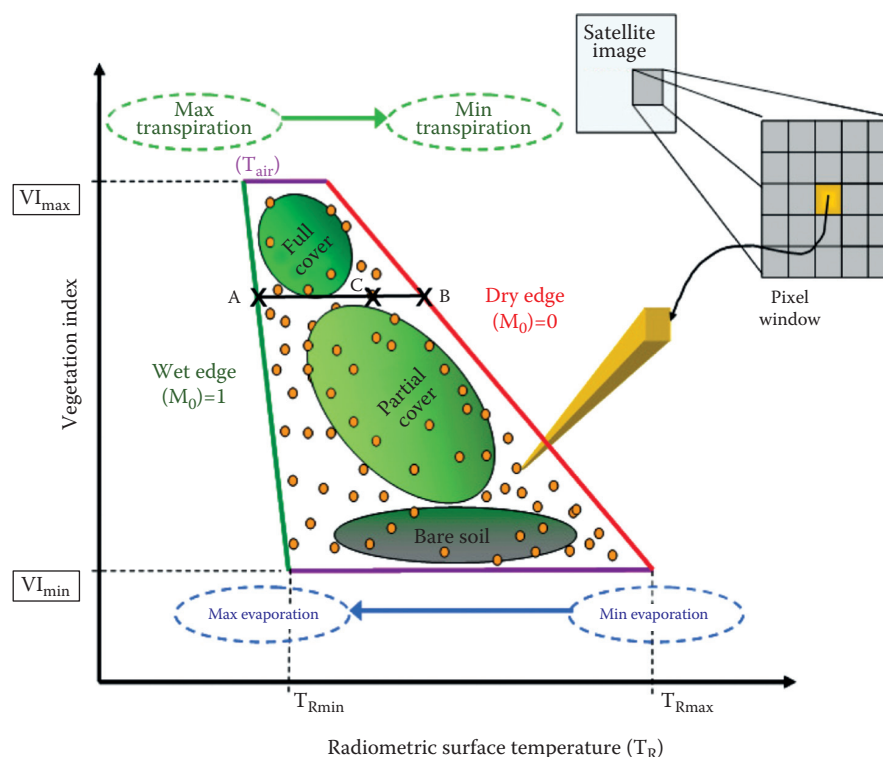
FIGURE 3.7 Example of a scatterplot of T_R versus VI, indicating wet and dry edges. (Reprinted from Petropoulos (2009) with permission from SAGE Publications Ltd.)

AQ6

or albedo, when these are plotted in a scatterplot (Figure 3.7). The method places theoretical boundary lines on the observed inverse relationship between T_R and VI or albedo and uses the position of a pixel in the T_R–VI or T_R–α space relative to those boundary lines to calculate either the evaporative fraction (Λ) as in the energy-based methods ("Radiometric Land Surface Temperature Methods for ET Estimation") or the reference evapotranspiration fraction (ET_f) as in the empirical VI methods (Section 3.2.2.1). A review of these methods including the theoretical basis of the principles underlying the scatterplot methods can be found in Petropoulos et al. (2009).

Briefly, assuming that cloud-contaminated pixels and pixels containing standing water have been masked, per pixel-level values of T_R and VI usually fall within a triangular (or trapezoidal) shape in the T_R–VI feature space (Figure 3.7). In Figure 3.7, each yellow circle represents the measurements from a single image pixel and includes the main properties believed to be represented by the T_R–VI pixel envelope. The triangular or trapezoidal shape in T_R–VI feature space is the result of the low variability of T_R and its relative insensitivity to soil water content variations over areas covered by dense vegetation and its increased sensitivity to soil moisture and larger spatial variation over areas of bare soil. The right-hand side border, the "dry edge" or "warm edge" is defined by the image pixels of highest temperature for the differing amounts of bare soil and vegetation and is assumed to represent conditions of limited surface soil water content and near-zero evaporative flux from the soil. The left-hand border, the so-called "wet edge" or "cold edge," corresponds to cooler pixels with varying amounts of vegetation cover and represents the limit of maximum surface soil water content. Variation along the triangle's base represents pixels of bare soil and is assumed to reflect the combined effects of soil water content variations and topography. The triangle apex equates to full vegetation cover. Similar to single-source temperature-based methods, pixels with minimum T_R represent the strongest evaporative cooling (point A in Figure 3.7), while those with maximum T_R represent the weakest evaporative cooling and low ET (point B in Figure 3.7). The triangle method defines vegetation cover directly from NDVI, whereas the trapezoid method uses fractional cover. Several methods then calculate ET_f as the ratio of distances CB and AB (Jiang and Islam, 2001; Moran et al., 1996), though a variety of methods is used to relate the position of a pixel in the scatterplot to ET.

Scatterplot methods for the estimation of ET can be divided into four groups based on the variables used in the scatterplot, namely, (1) T_R–VI scatterplots, (2) surface-to-air temperature difference and VI scatterplots, (3) T_R-albedo scatterplots, and (4) day–night temperature difference and VI scatterplots. A fifth method couples the T_R–VI scatterplot with a soil–vegetation–atmosphere transfer (SVAT) model. In the remainder of this section, each of the aforementioned groups of methods is reviewed, providing some information on the methods' principles and operation, as well as examples from its implementation in different ecosystems. A summary of the strengths and limitations of the different groups of approaches is also provided in Table 3.1.

3.2.4.1 T_R–VI Scatterplot Methods

A number of methods have been proposed to retrieve regional maps of ET from the T_R–VI triangular space over a number of different land cover types. Jiang and Islam (1999, 2001) suggested a technique based on an extension of the Priestley–Taylor equation and a relationship between remotely sensed T_R and VI. Jiang and Islam (2001) and Tang et al. (2010) use the T_R–VI graph to determine the $α_{PT}$ value from Equation 3.5 by assuming it is maximum on the wet edge and minimum on the dry edge, with global maxima at the minimum T_R and maximum T_R. $α_{PT}$ is calculated for a given pixel as 1.26 times the ratio of distance CB to AB in Figure 3.7. A key assumption in the method is that pixels with ET = 0 and ET = ET_o could be identified from the remotely sensed data. Jiang and Islam (2001) showed an RMSD in ET around 30% of the observed mean.

Jiang and Islam (2001) assume that dense vegetation transpires at the potential rate, which may not be the case for soil moisture stress. Nishida et al. (2003a,b) addressed this problem by estimating the evaporative fraction (Λ) with MODIS data for vegetation and soil separately, where ET from vegetation is calculated from a combination of the PM equation and the complementary relationship between potential ET and actual ET, and soil evaporation is calculated using the triangle method. Λ was computed every eight days for a range of climate and biome types, and validated at selected AmeriFlux sites, with good agreement (RMSD = 45.1 W/m², bias = 5.6 W/m², R^2 = 0.86).

AQ7

Critical to successful implementation of the T_R–VI methods is identification of the wet and dry edges. Zhang et al. (2006) proposed using the VI for estimating the dry and wet edges of the scatterplot. Tang et al. (2010) emphasized the importance of the accurate determination of the wet and dry edges in the accurate retrievals of the λET fluxes by the T_R–VI method of Jiang and Islam et al. (2001) and proposed a novel technique for determining quantitatively the dry and wet edges over a homogenous agricultural area.

3.2.4.2 Surface-to-Air Temperature Difference and VI Scatterplot Methods

Surface-to-air temperature difference methods are similar to T_R–VI methods but replace T_R with the difference between T_R and air temperature above the evaporating surface (z_2). Moran et al. (1994) introduced the "vegetation index–temperature trapezoid" for estimation of λET from the dT–VI domain in areas of partial vegetation cover, based on the PM Equation 3.4 and the crop water stress index (CWSI = 1–ET_f) (Jackson et al., 1981). The PM equation is inverted following Jackson et al. (1981) to estimate T_R at the four vertices of the dT–VI trapezoid, and 1–ET_f is calculated as ratio of the difference in temperature between a given pixel and the dry temperature (CB in Figure 3.7) to the difference in temperature between the dry edge and wet edge at the pixel's NDVI value (AB in Figure 3.7). Inversion of the PM equation to determine T_R at the four corners of the trapezoid avoids the requirement that there be a pixel in the image where ET = ET_o and another where ET = 0. Validation of the method was

carried out using a number of techniques over various land cover types. Moran et al. (1994) performed validation studies over both agricultural and semiarid grasslands in Arizona, United States, using model simulations and airborne data from the modular multispectral radiometer and ground-based measurements, respectively. Moran et al. (1996) used Landsat TM data to estimate ET for all grassland sites within their study region (Arizona, United States) and reported a RMSD of 29 W/m^2 in the estimation of the instantaneous λET and a consistent overestimation of λET in most sites.

Jiang and Islam (2003) modified the Jiang and Islam (1999) method, using T_R–T_2 in place of T_R and also by using the fractional vegetation cover (f_c) parameter, as a proxy for vegetation amount in place of the NDVI. In validation studies in the United States, λET flux estimates were predicted with a RMSD and bias of 58.6 and −42.4 W/m^2, respectively. Venturini et al. (2004) validated the method utilizing the same sensors for a region over South Florida, with RMSD in Λ prediction varying from 0.08 to 0.19, and a R^2 ranging from 0.4 to 0.7. Stisen et al. (2008) modified the method proposed by Jiang and Islam (2003) by combining it with thermal inertia information obtained from the geostationary SEVIRI sensor to estimate regional evaporative fraction (Λ) for a semiarid region in South Senegal in Africa. Comparisons performed by the authors showed a close agreement for both Λ (RMSD of 0.13 and R^2 of 0.63) and the instantaneous λET (RMSD of 41.45 W/m^2 and R^2 of 0.66). Shu et al. (2011) performed further validation of the Stisen et al. (2008) method using observations from the Fengyun-2C satellite in combination with the MODIS satellite products over a subtropical region in the North China Plain. Authors reported an R^2 equal to 0.73 and a RMSD of 0.92 mm/day for daily ET and R^2 = 0.55 and RMSE = 0.14 for Λ. A very important advantage of the Jiang and Islam (2003) method included its independence from absolute accuracy of the T_R measures, since T_R–T_2 equal to zero in their technique always represented the true cold edge of the triangle space where Λ equals zero. Nonetheless, this method also assumed a linear variation in Λ across the triangular/trapezoid domain of f_c–(T_R–T_2) feature space for each class of f_c, which might not be a realistic approximation, an issue that Stisen et al. (2008) tried to address by assuming nonlinear relationships between the biophysical properties encapsulated in the scatterplot.

3.2.4.3 T_R-albedo Scatterplot Methods

A different group of triangle methods is based on the correlation between T_R and α. Roerink et al. (2000) proposed the simplified surface energy balance index (S-SEBI) method for mapping ET based on the estimation of the evaporative fraction (Λ). S-SEBI calculates Λ using the same equation that SSEB uses to calculate ET$_f$ (3.22), but in S-SEBI, T_h and T_c are linear functions of albedo, where the linear function coefficients are determined from the boundaries of the T_R-albedo plot. Gómez et al. (2005) extended S-SEBI to the retrieval of daily evapotranspiration (λET) from high-spatial-resolution data (20 m) from polarization and directionality of Earth reflectance airborne instrument and a TIR camera (20 m), with an error of 90 W/m^2 and 1 mm/

day in the estimates of instantaneous and daily total λET, respectively. The method was evaluated further by Sobrino et al. (2005) using high-spatial-resolution airborne images from the digital airborne imaging spectrometer over agricultural areas in Spain. Authors reported accuracy in daily ET prediction better than 1 mm/day. Sobrino et al. (2007, 2008) subsequently adapted this methodology to the low-spatial-resolution data provided by the advanced very high resolution radiometer (AVHRR) and in the framework of the SEN2FLEX (field measurements, airborne data) project for similar sites in Spain. Authors reported a mean RMSD of ~1 mm/day in the estimation of daily λET by S-SEBI in comparison to ground λET measurements from lysimeters. Garcia et al. (2007) evaluated three operative models for estimating the nonevaporative fraction as an indicator of the surface water deficit in a semiarid area of southeast Spain. Other studies, such as by Zahira et al. (2009) monitored the drought status in Algerian forest covered areas with the combined use of S-SEBI with the visible, near-infrared (NIR) and TIR bands of Landsat enhanced thematic mapper plus (ETM+) imagery. Comparisons performed between the instantaneous λET fluxes predicted by S-SEBI and corresponding in situ data showed a R^2 of 0.85 and a RMSD of 64 W/m^2. Bhattacharya et al. (2010) calculated Λ from the T_R–α plot, validated over an agricultural region in India from the Indian geostationary meteorological satellite Kalapana-1. They reported an overall RMSE in the predicted daily ET estimates in the range of 25%–32% of measured mean. Comparisons of the 8 day ET product over agricultural land uses yielded RMSD of 26% (0.45 mm/day) with r = 0.8 (n = 52,853) as compared to daily ET. An important advantage of the technique of Bhattacharya et al. (2010) was that it could be implemented without the need of any ground observations, making it potentially a very good choice for operational use. Also, in contrast to some other methods discussed so far, their method avoided the H flux computation prior to ET flux estimation. A limitation is the assumption of uniform atmospheric conditions, and, like SEBAL and METRIC, the method cannot be implemented if wet and dry pixels are not present within the image.

3.2.4.4 Day–Night Temperature Difference and VI Scatterplot Methods

Another variant of the triangle method uses the difference between the day and night T_R (diurnal surface temperature variation or DSTV) versus the VI (Chen et al., 2002). The approach is based on the observed relationship between the difference between DSTV and soil moisture and thermal inertia (Engman and Gurney, 1991; Van de Griend et al., 1985). The technique first implements a simple linear mixture model to determine the fractional contribution of vegetation, dry soil surfaces, and wet soil surfaces to the observed values of NDVI and T_R. The vegetation and moisture coefficient (VMC), which is the same as ET$_f$ in the crop coefficient methods, was then expressed at each pixel as the sum of the VMC for each of the three surface types weighted by the fraction contribution at the given pixel. They implemented the algorithm with AVHRR data for a site in South Florida, United States, and showed percentage errors in the prediction of ET

compared to lysimeter measurements between 2.8% and 23.9% with RMSD's varying from 3.08 to 5.74 mm/day. An important advantage of the Chen et al. (2002) method was its requirement for only a small number of ground parameters. Limitations included the constraint to assume only three land cover types in the mixture modeling and the need for two T_R images to calculate the DSTV. Similar to Jiang and Islam (2001), this is required assuming that ET was the same for all dense vegetation. Also, the fact that the method required identification of areas of the three distinct land use/cover types that are required to be homogeneous and of sufficiently large spatial extend for the VMC to be estimated can be attributed as a limitation for its implementation.

Wang et al. (2006) proposed a modification to the method of Jiang and Islam (2003) using DSTV and NDVI in place of the daytime T_R. Wang et al. (2006) determined spatial variations of the DSTV–NDVI space using data from MODIS global 1 km daily products collected by the Aqua and Terra satellites, which were used to estimate Λ (parameterized as a function of air temperature and the Priestley–Taylor parameter α_{PT}), that was then compared to observations taken during 16 days in 2004, again at the Southern Great Plains (SGP) site, United States. The Λ retrievals from the DSTV–NDVI plot showed marked improvement compared to those retrieved from the daytime T_R alone. The DSTV method with Aqua day and nighttime images had an RMSD of 0.106, a bias of −0.002, and an R^2 of 0.61 for Λ, which was deemed satisfactory, especially after taking into account the simplicity of the approach and the requirement for only a small number of input parameters for its implementation.

3.2.4.5 Coupling T_R–VI Scatterplots with SVAT Models

The outputs from an SVAT model can be coupled with T_R and VI, where VI is replaced by the fractional vegetation cover (f_c). Overviews of this technique can be found in Carlson (2007) and Petropoulos and Carlson (2011). First, both NDVI and T_R are scaled to the maximum and minimum values in the image:

$$N^* = \frac{NDVI - NDVI}{NDVI_s - NDVI_o} \qquad (3.28)$$

where the subscripts s and o indicate dense vegetation and bare soil. Fractional vegetation cover (f_c) is calculated as the square of NDVI* following the methods of Gillies and Carlson (1995) and Choudhury et al. (1994). In an image with a full range of vegetation cover, N* and f_c will range from zero to one. Use of f_c allows us to plot both the SVAT-simulated and the measured surface radiant temperatures from the satellite sensor on the same scale. Scaled temperature is calculated as

$$T_{scaled} = \frac{T_R - T_{Rmin}}{T_{Rmax} - T_{Rmin}} \qquad (3.29)$$

where T_{Rmax} and T_{Rmin} are the maximum and minimum T_R for the dry, bare soil, and the wet vegetation, respectively, interpolated from the scatterplot bounds.

In the next step, the SVAT model is combined with T_{scaled} and f_c in order to derive the inversion equations that will provide the spatially explicit maps of ET. Initially, the SVAT model is parameterized using the time and geographic location and the site-specific atmospheric, biophysical and geophysical characteristics. Subsequently, the SVAT model is iterated until the simulated and observed extreme values of f_c and T_{scaled} in the T_{scaled}–f_c scatterplot are matched. Initial model simulations aim to align observed T_{scaled} with two end points (NDVIo, NDVIs) where they intersect the "dry" edge. This extrapolation to NDVIo and NDVIs guarantees that the implied temperatures along the "dry" edge for bare soil and full vegetation cover are consistent with simulations for soil moisture (Mo) of zero. Once the model tuning is completed, the simulation time corresponding to the satellite overpass is kept the same as the SVAT model is ran repeatedly, varying f_c and Mo over all possible values (0%–100% and 0–1, respectively), for all possible theoretical combinations of Mo and f_c. The result is a matrix of model outputs for a number of simulated parameters: Mo, f_c, T_{scaled}, λET, and H. Finally, this output matrix is used to derive a series of linear or quadratic equations, relating f_c and T_{scaled} to each of the other variables of interest: H, λET, and Λ. The SVAT model outputs are then used to derive a series of simple, empirical relations relating each of these parameters to f_c and T_{scaled} recorded at that location as quadratic polynomial equations:

$$ET = \sum_{p=0}^{3}\sum_{q=0}^{3} a_{p,q}\left(T_{scaled}\right)^p f_c^q \qquad (3.30)$$

where the coefficients $a_{p,q}$ are derived from nonlinear regression between the matrix values of f_c, T_{scaled}, and ET, and p and q vary from 0 to 3.

Gillies and Carlson (1995) first applied the technique using AVHRR images for a region in the United Kingdom. Carlson et al. (1995) then utilized the technique to derive daily estimates of ET for a site in Pennsylvania, United States, and validated the results using ground-based measurements from the push broom microwave radiometer and the NS001 instrument (30 m spatial resolution). Gillies et al. (1997) validated their method using high-resolution airborne data from the NS001 instrument and observations collected from the first International Satellite Land Surface Climatology Project (ISLSCP) field experiment (Vernekar et al., 2003) and MONSOON 90 (Kustas et al., 1991) field campaigns. The RMSD was ±10% for ET. Brunsell and Gillies (2003) implemented the method using data from the TMS/TIMS airborne (12 m) and coarse AVHRR (1 km) radiometers. Predicted fluxes from the implementation of the triangle method using the different remote sensing data were compared versus in situ observations from the SGP test site (United States). A close agreement for the high-resolution airborne data, within ~15% for λET, was reported, but results from the satellite data were in poor agreement with both the observations and the airborne data (50% difference for λET). Recently, Petropoulos et al. (2010) and Petropoulos and Carlson (2011) evaluated the triangle-SVAT

method at several CarboEurope sites using ASTER data. Closer agreements with the ground observations were generally found when comparisons were limited to cloud-free days at flat terrain sites. Under such conditions, the triangle-SVAT method estimated instantaneous λET with a mean RMSD of 27 W/m^2.

The triangle-SVAT method has several advantages over the other scatterplot methods. First, it provides a nonlinear interpretation of the T_R–VI space, which can be a more realistic assumption than the linear assumption in the empirical triangle methods. The triangle-SVAT method offers the potential for relatively easy transformation of the instantaneous-derived ET fluxes to daytime averages and allows regional estimates of the H flux and the surface soil moisture content together with the ET fluxes, potentially very useful parameters to have information for many practical applications. In addition, it offers the possibility to extrapolate the instantaneous measurements of the computed energy fluxes from one time of day to another (see Brunsell and Gillies, 2003) and to times with clouds. A disadvantage is that the SVAT requires a large number of input parameters and its parameterization also requires user expertise, complicating its implementation over large geographic areas.

3.2.5 Seasonal ET Estimates and Cloud Cover Issues

All three families of methods for estimating ET reviewed in this chapter (vegetation based, temperature or energy based, and scatterplot based) produce daily maps of ET that can be temporally interpolated to estimate seasonal ET, which is often the main output of concern to water managers and agriculturalists. Interpolation is necessary because the satellite platforms that generate high-resolution imagery often have long overpass return periods (e.g., Landsat at 2 weeks) and because of clouds, which compromise the generation of daily ET maps even when daily imagery are potentially available (MODIS). Cloud cover may be less of a problem in arid and some semiarid climates but is a significant obstacle for determining season-total ET in semihumid and humid climates. In regions with Mediterranean climates, the main growing season in summer corresponds to cloud-free conditions, and satellite methods work well for determining seasonal ET from daily values. In other locations, where the growing season coincides with the wet season, such as monsoon-dominated areas, cloud-free imagery is often not available during the main crop growing season, and EO-based methods for ET estimation may need to be supplemented with other modeling approaches like the FAO-56 method (Allen et al., 1998) or more complex SVAT models.

Three methods to interpolate ET maps for days without cloud-free imagery are (1) the evaporative fraction (Λ) method, (2) the crop coefficient (ET_f) method, and (3) the simulation model method (Long and Singh, 2010). The Λ and crop coefficient methods for estimating seasonal ET are very similar to the methods for generating daily estimates from instantaneous estimates, but there are special problems with cloud cover when interpolating over longer time scales that are discussed further in this section.

The Λ method, which is also used to calculate daily ET from instantaneous values of the evaporative fraction (Λ_{op}) (Section 3.2.3.5), calculates ET for a date without cloud-free imagery as the product of R_n for the day without cloud-free imagery and Λ_{op} from the date with cloud-free imagery. The Λ method assumes that Λ_{op} is constant between the dates of cloud-free imagery, which is more likely to be violated over several days than for a single day, especially if cloud cover changes significantly. Farah et al. (2004) found that Λ does not vary with cloud cover over short (weekly) time intervals over woodland and grassland in central Kenya, which encourages the use of the evaporative fraction method (Farah et al., 2004). The method may produce accurate ET values over periods of 5–10 days (Farah et al., 2004), but over many areas, cloudy conditions persist much longer. Others have found that Λ increases during cloudy periods due to a larger proportionate reduction in H than in λET (Van Niel et al., 2011).

The crop coefficient approach calculates the ratio of actual to reference ET (=ET_f) on the day of satellite imagery, then multiplies that fraction by reference ET for each day without imagery (Long and Singh, 2010):

$$ET_{period} = \sum_{i=d1}^{n} ET_f ET_{oi} \qquad (3.31)$$

where
  ET_f is for the 24 h period on the date with satellite-derived ET
  ET_{oi} is reference ET on day i, which does not have imagery
  d1 is the beginning day without ET data
  n is the number of consecutive days without image-derived ET estimates

The ET_f can be assumed constant between images, or could be linearly varied between available ET images. Allen et al. (2007) suggest that one ET image per month is sufficient to estimate seasonal total ET, though this may not be the case under conditions of rapidly varying soil moisture conditions or surface saturation, as might be expected in irrigated areas. The ET_f method has been applied using the METRIC model (Allen et al., 2007) and in northern China (Li et al., 2008).

The third approach to estimating ET on days without cloud-free imagery, the simulation model method, uses satellite-based ET on clear days to calibrate an SVAT model or some simplified version of an SVAT model, which is then run for all days including cloudy days. Simplified models of the relationship between meteorological conditions and ET, such as the Granger and Gray (GG) model (Granger and Gray, 1989), have been used in combination with SEBAL to estimate ET during cloudy periods (Long and Singh, 2010). The GG model uses the complementary relationship between actual and potential ET to estimate actual ET when imagery are not available. One major limitation of the GG model as currently applied is that the spatial resolution and accuracy of the ET estimates depend on the availability of meteorological data at a comparable resolution to the observed heterogeneity in ET. Other simple models of soil moisture stress

have been developed that use ET derived from remote sensing to estimate model states on clear days and extrapolate those state variable values to dates with clouds (Anderson et al., 2007).

3.3 ET Methods Intercomparison Studies

Each of the three families of methods used to estimate ET has different strengths and weaknesses (Table 3.1). Temperature-based methods were developed to estimate ET from irrigated agriculture and therefore are more likely to perform best there but are often sensitive to how they are calibrated and sometimes depend on the existence of extreme values of ET in the image. Vegetation-based methods were developed for global application, with a focus on rainfed systems, and may have lower accuracy in irrigated systems where ET may be decoupled from a VI, particularly on the shoulders of the growing season. Scatterplot methods incorporate both temperature and vegetation but usually require internal calibration and, like some one-source energy-based methods, often depend on extremes of ET to be present in the image. Studies that compare vegetation-, temperature-, and scatterplot-based methods together are not common, and here, we review some recent examples. Such intercomparisons are important, because vegetation- and temperature-based methods have strengths in different environments, and quantitative information on which does better under what climate and land use conditions can guide the user in method selection.

Rafn et al. (2008) compared an NDVI method for deriving ET_f with the energy balance METRIC method over mixed crops in an Idaho irrigation district. They concluded that the empirical coefficient method was a fully objective and repeatable process that was fast, easy, and less costly to employ than the METRIC method. Similarly, Gonzalez-Dugo et al. (2008) found that NDVI-derived ET_f combined with ET_o measurements predicted ET of corn and soybean crops as well as thermal-band methods in Central Iowa, although it over-estimated ET of corn during a dry-down period.

Vinukollu et al. (2011b) compared three different models: SEBS (Su, 2002), MOD16 (Mu et al., 2007), and PT-JPL (Fisher et al., 2008). The focus of their study was to compare the instantaneous (W/m^2) and daily (mm) ET fluxes predicted by the three models implemented with data from sensors on the MODIS–Aqua satellite augmented by AVHRR data for vegetation characterization. Vinukollu et al. (2011b) compared the three models at three spatial scales. At the first spatial scale, λET from the three models was compared to and parameterized by eddy covariance flux tower data. At the second scale, a basin-scale water balance validation was performed using the models parameterized by remote sensing data. Finally, the models were compared against a hydrologic model driven by surface climate reanalysis at a global scale and on a latitudinal basis. For towers where soil evaporation plays an important role following precipitation events, SEBS and PT-JPL showed the highest and similar correlations, though large differences occurred during the primary growing season. Correlations between λET measured at towers in densely vegetated areas, such

as evergreen and deciduous broadleaf forests, were highest for PT-JPL, reflecting again the importance of R_n in modulating λET in these areas. At the basin scale, however, the performance of each model was comparable. At the global scale, the vegetation- and energy-based ET methods tended to underestimate simulated soil moisture storage in water-limited (arid) regions of the world.

Ershadi et al. (2014) evaluated the PT-JPL model against SEBS, the 2011 updated MOD16 (Mu et al., 2011), and a complementary approach (advection–aridity model) against ET observed at FLUXNET towers. The PT-JPL model had the closest correlation with the FLUXNET-estimated ET but compared closely with SEBS. The PT-JPL model did particularly well in densely vegetated areas and was comparable to SEBS over croplands and grasslands. On a seasonal basis, all of the models, except the PT-JPL model, exhibited strong seasonality. The poor performance of MOD16 and SEBS in densely vegetated areas was attributed to the uncertainties that arise from a large number of model input requirements and complexity, including the sensitivity of their ET estimates to resistance parameters. All of the models did poorly over shrublands and evergreen needle leaf forests, reflecting the difficulty of NDVI in capturing vegetation dynamics for these land cover types. In conclusion, the authors suggested that, for regional to global studies, an ensemble of models, weighted by the success of contributing models for each land cover type be employed, given that no one single model performs consistently well across all land cover types. Such an approach could prove particularly useful in regional or global applications, where different model output could be used depending on land cover.

Velpuri et al. (2013) compared SSEBop ET (Senay et al., 2013) with point and gridded flux tower observations and water balance ET, gridded FLUXNET ET (Jung et al., 2011) and MOD16 ET (Mu et al., 2011) over the conterminous United States (CONUS). Point-scale validation using data from 60 FLUXNET tower locations against monthly SSEBop and MOD16 ET data aggregated by years revealed that both ET products showed overall comparable annual accuracies with mean errors in the order of 30%–60%. Although both ET products showed comparable results for most land cover types, SSEBop showed lower RMSE than MOD16 for grassland, irrigated cropland, and forest classes, while MOD16 performed better than SSEBop in rainfed croplands, shrublands, and woody savanna classes. Basin-scale validation of MOD16, SSEBop and gridded FLUXNET ET data against water balance ET indicated that both MOD16 and SSEBop ET matched the accuracies of the global gridded FLUXNET ET dataset at different scales. Both MODIS ET products effectively reproduced basin-scale ET response (up to 25% uncertainty) compared to CONUS-wide point-based ET response (up to 50%–60% uncertainty) illustrating the potential for MODIS ET products for basin-scale ET estimation. The apparent CONUS-wide uncertainties (up to 50%–60%) for monthly MODIS ET represented an overall error using data from several FLUXNET stations. The uncertainty for individual stations over time is much lower as shown from previous studies, including Mu et al. (2011) and Senay et al. (2013) who reported uncertainties up to 20% (MOD16) and 30% (SSEBop), on

individual station-based FLUXNET validation, and Singh et al. (2013) reported uncertainties as low as 10% for individual stations in the Colorado River basin. Thus, despite an apparent high level of uncertainty at the CONUS-scale, the spatially explicit monthly SSEBop ET products can be useful for localized applications.

Choi et al. (2009) compared three models for estimating spatially distributed λET fluxes over a region in Iowa, United States, using Landsat TM/ETM+ imagery and ancillary observations from the SMACEX 2002 field experiment: TSEB (based on ALEXI), METRIC, and the T_R/VI method of Jiang and Islam (2001). TSEB and METRIC yielded similar and reasonable agreement with measured λET and H fluxes, with RMSD of 50–75 W/m² whereas for the T_R–VI method RMSE was over 100 W/m² (3.8 mm/day). Although TSEB and METRIC were in good agreement at the point comparisons performed, a spatial intercomparison of their results of gridded model output (i.e., comparing output on a pixel-by-pixel basis) revealed significant discrepancies in modeled turbulent heat flux patterns that correlated with vegetation density, particularly for H fluxes.

3.4 Special Problems in Cropped Areas

3.4.1 Landscape Heterogeneity and Spatial Disaggregation

Estimation of ET from croplands using remote sensing is particularly challenging in heterogeneous landscapes where agricultural plots are s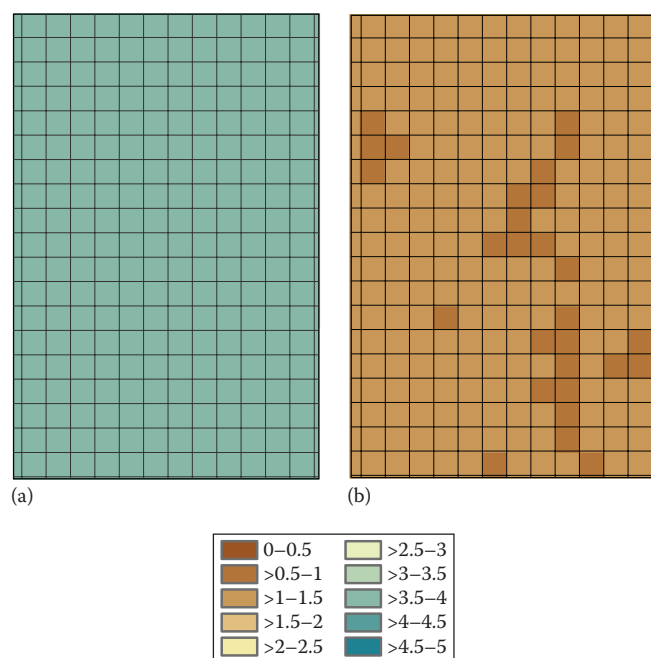mall (Figure 3.8). In India, for example, there are large areas of homogeneous irrigated cropping in canal-irrigated systems, but more than 50% of the irrigated area is supplied from groundwater wells, which are typically individually owned bore wells supplying small plots (<1 ha). The small groundwater-irrigated plots are often topographically organized, occurring mostly near stream channels where the water table is shallow, resulting in narrow bands of irrigation (Figure 3.8), which requires mapping irrigated areas as fractional cover of 1 km MODIS pixels (Biggs et al., 2006). Most globally available datasets are at a resolution of 1 km (MOD16) or coarser, which is significantly larger than irrigated patches in many areas. Even in the United States, where agricultural fields are large, 1 km resolution can be too coarse to resolve individual fields and to map ET differences by crop (Kustas et al., 2004). Kustas et al. (2004) documented that 250 m resolution was necessary to resolve differences in ET among agricultural fields in Iowa and that the variance in estimated ET decreases with increasing pixel size. Townshend and Justice (1988) estimated that land cover change mapping requires a spatial resolution of 250–500 m. Irrigated landscapes might be expected to require finer resolution than 250 m, especially in developing countries where plots are small.

Global methods (PT-JPL, MOD16) were designed to estimate ET over large spatial scales, often as input to community land surface models, rather than to assess crop-specific ET. In heterogeneous irrigated landscapes in semiarid climates, extreme spatial variability in soil moisture and ET means that extremes of low and high ET may occur in a single 1 km pixel, which significantly reduces ET estimates in the 1 km aggregated average. This could result in an underestimation of ET from irrigated cropland if no further disaggregation technique were applied. High-resolution imagery (<100 m, e.g., Landsat 30 m) is only available at 2 weeks or greater temporal resolution, which makes its application problematic in areas with high cloud cover and dynamic land cover. Some efforts have focused on combining imagery from different platforms to generate high-resolution maps of seasonal ET. Here, we review a few select studies to illustrate the potential for cross-platform downscaling.

Thermal imagery typically has a coarser resolution than visible and near-infrared (VNIR) bands for a given spectroradiometer. For the MODIS sensor, VNIR bands are available at 250 m resolution, while the thermal band is at 1 km. For Landsat, VNIR are at 30 m, while the TIR band is 120 m but has been resampled to either 60 m (before February 25, 2010) or 30 m (after February 25, 2010). The higher-resolution bands can be used to sharpen the coarse resolution thermal band using the inverse relationship between T_R and NDVI (Agam et al., 2007; Kustas et al., 2003). The first step is to coarsen the NDVI image to the resolution of the thermal image. Both the mean NDVI and the coefficient of variation (CV) of the high-resolution NDVI are calculated at the low resolution. Then, a percentage of pixels with the lowest CV with each of several bins of NDVI (e.g., 0–0.25, 0.2–0.5, >0.5) are selected to parameterize a function relating

0–0.5	>2.5–3
>0.5–1	>3–3.5
>1–1.5	>3.5–4
>1.5–2	>4–4.5
>2–2.5	>4.5–5

FIGURE 3.8 Maps of SEBAL ET (mm/day) in a groundwater irrigated area in southern India at 30 m (a) and aggregated to 1 km (b). The grid in both panels represents 1 km pixels. (Based on data from Ahmad, M. et al., *Water Sci. Technol.*, 53, 83, 2006.)

low-resolution T_R to low-resolution NDVI, which is used to predict T_R at low resolution:

$$\hat{T}_{R_{low}}\left(NDVI_{low}\right) = a_{ds} + b_{ds}NDVI_{low} + c_{ds}NDVI_{low}^2 \quad (3.32)$$

where

a_{ds}, b_{ds}, and c_{ds} are empirical coefficients determined through least squares regression

ds subscript designates downscaling to differentiate the coefficients from the a and b parameters of the SEBAL algorithm.

A linear equation could also be used, and the form of the equation depends on the observed T_R-NDVI relationship. While (3.32) can be used directly to predict T_R at high resolution using high-resolution NDVI, the correlation between T_R and NDVI may break down for pixels with low NDVI, including irrigated areas in either the beginning or end of the growing season, where high soil moisture or standing water and therefore low T_R can occur with low vegetation cover (Figure 3.7). Kustas et al. (2003) proposed an additional correction using the residual of (3.32):

AQ8

$$\hat{T}_{R_{hi}} = \hat{T}_{R_{low}}\left(NDVI_{hi}\right) + \left(T_{R_{low}} - \hat{T}_{R_{low}}(NDVI_{low})\right) \quad (3.33)$$

where

$\hat{T}_{R_{hi}}$ is the predicted radiometric temperature at high spatial resolution

$\hat{T}_{R_{low}}\left(NDVI_{hi}\right)$ is the predicted radiometric temperature using high-resolution NDVI and (3.32)

$T_{R_{low}}$ is the observed radiometric temperature at low resolution

$\hat{T}_{R_{low}}(NDVI_{low})$ is the predicted radiometric temperature using low-resolution NDVI (3.32).

Based on observed scatterplots of NDVI and T_R (Figure 3.7), this correction will be minimal for pixels with high NDVI and largest for pixels with low NDVI.

More complex algorithms that use all visible and NIR bands to model T_R in a moving window may be more successful in irrigated landscapes (Gao et al., 2012). Other algorithms have been developed to downscale T_R by fusing MODIS and Landsat, including those that use artificial neural network models (Bindhu et al., 2013).

One downscaling method specific to the ALEXI model, DisALEXI, was discussed in Section 3.2.3.2. DisALEXI ensures consistency in aggregated ET across scales by adjusting the high-resolution estimates to match the low-resolution average. Comparisons of ET estimated using algorithms forced by imagery with different resolutions have found disagreement. For example, SEBS-ET was calculated using Landsat, ASTER, and MODIS data (McCabe and Wood, 2006). SEBS-ET was similar for the high-resolution imagery (Landsat and ASTER) but SEBS-ET from Landsat or ASTER differed markedly from SEBS-ET derived from MODIS, even when the Landsat and
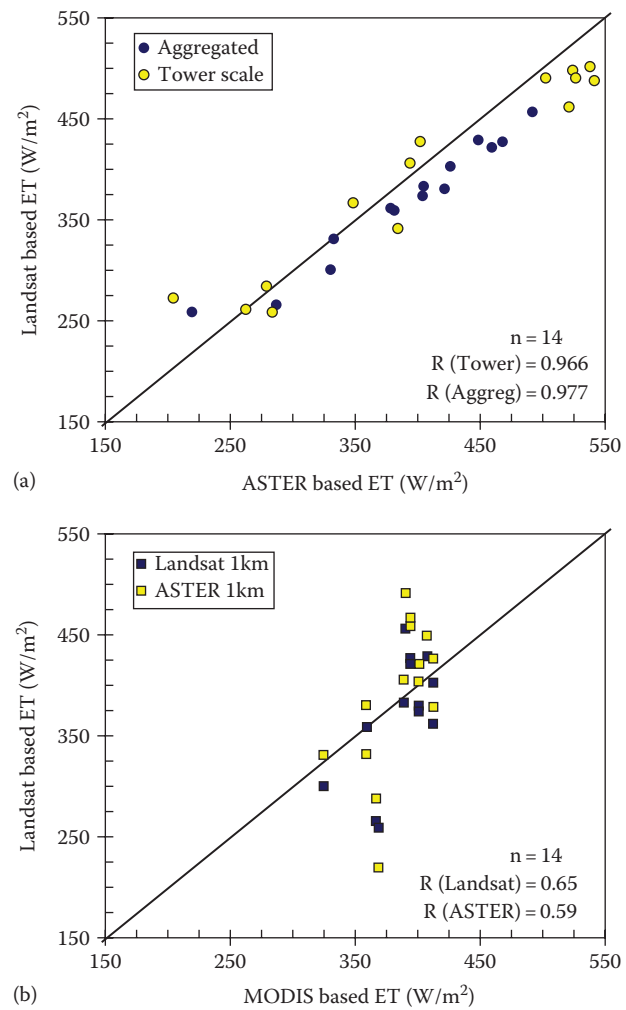

(a)

(b)

FIGURE 3.9 Comparison of SEBS-ET calculated using ASTER and Landsat data (a) and MODIS, ASTER, and Landsat (b). In the top panel, tower scale refers to individual pixels of Landsat or ASTER, while aggregated are the Landsat and ASTER SEBS-ET aggregated to MODIS resolution (1 km). (Reprinted from *Remote Sens. Environ.*, 105, McCabe, M.F. and Wood, E.F., Scale influences on the remote estimation of evapotranspiration using multiple satellite sensors, 271–285, Copyright (2006), with permission from Elsevier; Glenn, E.P. et al., *Ecohydrology*, 1, 316, 2008b; Glenn, E.P. et al., *Ecol. Eng.*, 59, 176, 2013.)

AQ9

ASTER ET were aggregated to MODIS resolution (McCabe and Wood, 2006) (Figure 3.9). This is likely due to nonlinear averaging of important inputs to the energy balance equations and needs to be acknowledged when using moderate resolution (1 km) data to estimate ET. The spatial average ET from all three image sources matched to within 10%–15%, suggesting that the low-resolution MODIS imagery were useful for watershed-scale estimates of ET (50 km²), but the MODIS data underestimated the variability present in the landscape. McCabe and Wood (2006) conclude that MODIS data are sufficient for estimating ET at watershed scales but are likely not accurate for estimating crop ET at resolutions that resolve ET from individual fields.

3.4.2 High-Resolution ET Mapping: New and Upcoming Platforms

There is a pressing need for datasets that allow mapping of ET at the spatial resolution of individual fields. In developing countries, field sizes may be very small (<1 ha), requiring high-resolution data for field-scale mapping (~10^1 m). While high-resolution data exist in historical archives (Landsat, 30 m) and contemporary datasets (Landsat 8, ASTER), the overpass frequency (~2 weeks for Landsat) may not be sufficient to capture high-quality data in areas with either dynamic land cover or cloud cover during the cropping season. Data from new remote sensing platforms could prove very useful for mapping ET at spatial and temporal resolutions that more closely approximate actual variability in agricultural landscapes. Satellites such as Sentinels 2 and 3, planned for launch in 2014 by the European Space Agency, and NASA's hyperspectral infrared imager (HyspIRI, launch date unknown at time of publication) (Hook and Green, 2013) hold promise for providing high-resolution data at high temporal frequency. Sentinel-2 will provide data on visible, NIR, and shortwave infrared wavelengths at 10 or 20 m with a revisit time of 5 days at the equator and 2–3 days at midlatitudes. This will provide unprecedented data for vegetation-based ET models, including NDVI and the LAI. Sentinel-3 will provide thermal imagery at 1 km resolution with revisit times of approximately 1 day at the equator. This temporal and spatial resolution is similar to existing MODIS data, so the additional gains for temperature-based methods may come in downscaling the 1 km data using Sentinel-2 data.

Other high-resolution datasets include the Landsat series (30 m), with the latest Landsat 8 data beginning in June 2013, with 14 day overpass. The Landsat archive can provide historical imagery to the late 1970s, and it has been used in many ET applications (Ahmad et al., 2006; Allen et al., 2013; Anderson et al., 2012; Glenn et al., 2011; Kjaersgaard et al., 2011; Norman et al., 2003) though problems with cloud cover may be encountered, particularly where the rainy season coincides with the cropping season. ASTER generates data with 15 m resolution in the visible and 90 m in the TIR bands, but the image footprints and times of acquisition are often irregular, complicating its use for seasonal ET estimation (Er-Raki et al., 2008; Galleguillos et al., 2011). NASA's HyspIRI mission will provide visible to shortwave infrared (VSWIR: 380–2500 nm) at 60 m resolution with a revisit time of 19 days, and mid-infrared and TIR (3–12 μm) at 60 m resolution and revisit time of 5 days (Hook and Green, 2013). The high-resolution TIR data, in particular, generated by HyspIRI will be valuable for mapping ET from irrigated croplands in heterogeneous landscapes.

3.4.3 Model Complexity, Equifinality, and Sources of Error in ET Models

The EO-based estimates of ET presented in this chapter all rely on models to predict ET from EO data, and so have problems similar to other applications of models to estimate hydrological processes, including equifinality and parameter uncertainty.

Equifinality arises in models that have many variables in the determining equations but few actual data to populate the equations (Beven, 2006a; Franks et al., 1997; Medlyn et al., 2005). These models are frequently calibrated using approximated or assumed values for unmeasured variables. As a result, different models with different assumptions and levels of complexity can converge on the same output values, despite different process representations. Equifinality in hydrological models complicates the choice of a model for a given application, makes the use of models for hypothesis testing difficult, and results in uncertain prediction for times or places that have not been used for calibration (Beven, 2006a).

In the case of remote sensing of ET, problems of equifinality can occur in process-based models for use over mixed landscapes of natural and agricultural areas, for which few spatially distributed ground data are available. Remote sensing data usually consists only of radiance values from two or three bands (VNIR), and an imperfect estimate of T_R from thermal bands. However, the determining equations generally have numerous variables, including fractional cover, LAI, roughness lengths for mass and momentum transfer, albedo, emissivity, net radiation and ground heat flux (e.g., Bastiaanssen et al., 1998; Kustas and Norman, 1999). All of these are related in some way to vegetation cover, so they are often estimated by ~~the use of~~ vegetation indices. However, this introduces the problem of collinearity among what are supposed to be independent variables. For example, Glenn et al. (2008a) gave examples where five different plant stands in a mixed agricultural and riparian environment had the same NDVI values but differed markedly in plant heights (and presumably therefore roughness lengths), fractional cover, and LAI. VIs cannot uniquely determine separate biophysical variables; rather, they give an integrated measure of canopy "greenness" (Baret and Buis, 2008; Glenn et al., 2008a). Equifinality can be suspected to apply to surface energy balance methods as well as to VI methods that attempt to parameterize numerous variables with limited remote sensing data. For example, the SEBAL algorithm depends on the calibration of resistance terms and of the coefficients in the T_R and air temperature (T_2) relationship at the wet and dry pixels, but other representations of the T_R–T_2 relationship may result in different predictions at other locations in the image. McCabe et al. (2005) explicitly include the impact of different model parameterizations on ET estimated by calibrating a hydrological model with remotely sensed data. Explicit treatments of uncertainty in ET estimation should be produced in future efforts.

A problem related to equifinality is parameter uncertainty. In the PT-JPL model, for example, several parameters are based on field studies in specific locations, with unknown applicability in other regions. On the other hand, oversimplification of the process representation may require additional ground-level data or calibration of the simplified model to a specific location, as in the empirical crop coefficient methods. This complicates the use of simplified methods in global applications or in other regions with limited ground-level data for input or calibration. Overall, a balance needs to be struck between model complexity

AQ10

and applicability to unmeasured locations; the ideal model is the simplest one that provides adequate fit to observed data given the limitations in input data availability. There is significant scope for future research in the level of complexity needed for different scales of application, particularly at regional and global scales.

Another problem with application of EO data to estimate ET is error and uncertainty in the ground data used for calibration and validation. Ground measurements usually come from eddy covariance flux tower measurements, and these have typical errors on the order of 15%–30% when compared to lysimeters or other highly accurate measurements of ET (Allen et al., 2011). A particular problem with eddy covariance data is the "energy closure" error, where the sum of measured λE + H does not equal measured Rn−G. λE and H are usually increased to force closure, preserving the λE/H ratio of the measured data (Twine et al., 2000), but usually, there is no way to check if this correction improves the ET estimates. Scott (2010) compared eddy covariance results at three flux tower sites in a semiarid rangeland, at which precipitation, infiltration, and runoff were also measured. Uncorrected eddy covariance data gave ET values close to precipitation minus runoff and infiltration, where data corrected to force closure overestimated ET at each site by 10%–20%.

A further problem is the mismatch between scales of measurement. Evett et al. (2012) compared surface energy balance components used to calculate ET at scales ranging from weighing lysimeters (4.7 m diameter), to small plots, to whole fields (several hundred ha) captured by aerial and satellite imagery. They concluded that even with the best equipment and expertise, it was difficult to measure ET accurately using flux towers. Advection led to underestimates of ET by tower sensor systems compared to lysimeters even after correcting for energy closure. This inaccuracy affected the interpretation of remote sensing results, which depended on flux tower data for validation. They urged caution in interpreting ET data from semiarid environments with advective conditions, especially those with mixes of irrigated and dryland crops and native vegetation. In dryland areas in Spain, Morillas et al. (2013) found that a TSEB model had errors of up to 90% in estimating λET compared to eddy covariance because latent heat flux is estimated as a residual and was a small component of the overall energy budget. Glenn et al. (2013) reported that both energy balance and vegetation-based remote sensing methods overestimated ET of salt-stressed shrubs by 50% or more in a riparian corridor.

As this review shows, there has been a proliferation of remote sensing ET methods, most of which have uncertainty or errors of 10%–30% compared to ground measurements on a monthly basis with lower error (e.g., 5%–10%) on a seasonal or annual basis (Table 3.1) (Allen et al., 2011). As also seen in this review chapter, comparison studies often do not point to a clear choice of methods due to the problem of equifinality and errors and uncertainties in ground data (e.g., Gonzalez-Dugo et al., 2009). Simple methods tend to perform as well as more complex methods (e.g., Jiang et al., 2004), but simple methods often depend on calibration to ground level data and may not be applicable

outside of the area of calibration. Reducing the error and uncertainty in remote sensing estimates of ET must depend in part on improving ground methods for measuring ET. Medlyn et al. (2005) and Beven (2006b) recommended more rigorous sensitivity analyses of ET models and explicit representation of uncertainty in model estimates. Medlyn et al. (2005) concluded that simplistic comparisons of ET models with eddy covariance data could lead to errors due to problems of equifinality, insensitivity, and uncertainty in both the models and the ground data. Their main concern was SVAT models but their conclusions can also be applied to remote sensing methods for estimating ET (Glenn et al., 2008a). A central goal of future research should be to calculate pixel-wise estimates of the uncertainty in ET estimated from satellite imagery that accompany any map of ET, calculated using either a range of plausible parameter values or an intercomparison of models with different assumptions.

3.5 Conclusions

This chapter provided an overview of methods for estimating ET from EO platforms, with a focus on croplands. The chapter used consistent mathematical symbols across all methods, facilitating intercomparison of multiple techniques. The hope in providing a single comparison of multiple methods in one text is that practitioners and researchers can see the similarities among different methods and potentially see how their particular model choice could be extended to include other methods, as well as to more clearly identify the assumptions, strengths, and weaknesses of each family of methods. There are many different methods that are available to use with different degrees of complexity, utilizing EO data acquired from different platforms at different regions of the electromagnetic spectrum. Techniques are also characterized by different strengths and limitations related to their practical implementation and have varying accuracy. Many validation studies have, however, confirmed at least the potential for regional- and global-scale mapping at 1 km spatial resolution, and in some cases, operational implementation. The global models are typically vegetation-based methods, and their ability to perform in irrigated areas, where soil evaporation may occur in dry environments, has not been extensively tested. By contrast, temperature-based methods, especially those requiring internal calibration, have been widely tested in irrigated environments but face challenges in application for geographic scales larger than a single satellite image. On this basis, we encourage further intercomparison of the different EO-based modeling schemes for deriving ET in croplands and, for operational purposes, EO-based model ensembles that integrate the spatiotemporal benefits of each method.

Most studies that evaluate the ability of different techniques to predict ET have been based on direct comparisons between predicted fluxes and corresponding in situ measurements. Other modeling approaches, such as uncertainty or sensitivity analysis, have so far been little incorporated in such studies, despite their importance for any all-inclusive model validation/verification (Petropoulos et al., 2013). Explicit estimation of uncertainty

in ET, including pixel-wise estimates of model error, would represent a significant advance.

More validation studies for operationally distributed products need to be conducted in different ecosystems globally. Such studies, if conducted in a systematic way following an acceptable protocol, will identify issues in the algorithmic design of these products, which will improve our capability to operationally estimate ET from EO sensors. More work should be directed toward the development of schemes for the temporal interpolation of the instantaneous ET estimates, as well as of downscaling approaches of ET to the resolution of individual fields where possible. Since no model performs optimally in all land covers, regional or global applications could consider using different models for different land cover types. We encourage further intercomparison of vegetation- and temperature-based methods, and further research on downscaling to the resolution of individual fields. We anticipate that EO data from new satellite platforms planned already to be launched in the next few years alone or in synergistic use to each other will help to meet some but not all of these needs.

Acknowledgments

References

Agam, N., Kustas, W.P., Anderson, M.C., Li, F., and Colaizzi, P.D. 2007. Utility of thermal sharpening over Texas high plains irrigated agricultural fields. *Journal of Geophysical Research* 112, D19110. doi:10.1029/2007JD008407.

Ahmad, M., Biggs, T.W., Turral, H., and Scott, C.A. 2006. Application of SEBAL approach to map the agricultural water use patterns in the data scarce Krishna River Basin of India. *Water Science and Technology* 53, 83–90.

Allen, R., Irmak, A., Trezza, R., Hendrickx, J.M.H., Bastiaanssen, W., and Kjaersgaard, J. 2011. Satellite-based ET estimation in agriculture using SEBAL and METRIC. *Hydrological Processes* 25, 4011–4027. doi:10.1002/hyp.8408.

Allen, R.G. 2000. Using the FAO-56 dual crop coefficient method over an irrigated region as part of an evapotranspiration intercomparison study. *Journal of Hydrology* 229, 27–41.

Allen, R.G., Burnett, B., Kramber, W., Huntington, J., Kjaersgaard, J., Kilic, A., Kelly, C., and Trezza, R. 2013. Automated calibration of the METRIC-landsat evapotranspiration process. *Journal of the American Water Resources Association* 49, 563–576. doi:10.1111/jawr.12056.

Allen, R.G. and Pereira, L.S. 2009. Estimating crop coefficients from fraction of ground cover and height. *Irrigation Science* 28, 17–34.

Allen, R.G., Pereira, L.S., Howell, T.A., and Jensen, M.E. 2011. Evapotranspiration information reporting: I. Factors governing measurement accuracy. *Agricultural Water Management* 98, 899–920.

Allen, R.G., Pereira, L.S., Raes, D., and Smith, M. 1998. Crop evapotranspiration-guidelines for computing crop water requirements-FAO, Irrigation and drainage paper 56. Rome.

Allen, R.G., Tasumi, M., and Trezza, R. 2007. Satellite-based energy balance for mapping evapotranspiration with internalized calibration (METRIC)—Model. *Journal of Irrigation and Drainage Engineering* 133, 380–394. doi:10.1061/(ASCE)0733-9437(2007)133:4(380).

Anderson, M.C., Allen, R.G., Morse, A., and Kustas, W.P. 2012. Use of Landsat thermal imagery in monitoring evapotranspiration and managing water resources. *Remote Sensing of Environment* 122, 50–65. doi:10.1016/j.rse.2011.08.025.

Anderson, M.C., Kustas, W.P., and Hain, C.R. 2013. Mapping surface fluxes and moisture conditions from field to global scales using ALEXI/DisALEXI. In: *Remote Sensing of Energy Fluxes and Soil Moisture Content*, Petropoulos, G.P. (ed.), pp. 207–232. Boca Raton, FL: Taylor and Francis.

Anderson, M.C., Norman, J.M., Diak, G.R., Kustas, W.P., and Mecikalski, J.R. 1997. A two-source time-integrated model for estimating surface fluxes using thermal infrared remote sensing. *Remote Sensing of Environment* 60, 195–216. doi:http://dx.doi.org/10.1016/S0034-4257(96)00215-5.

Anderson, M.C., Norman, J.M., Mecikalski, J.R., Otkin, J.A., and Kustas, W.P. 2007. A climatological study of evapotranspiration and moisture stress across the continental United States based on thermal remote sensing: 1. Model formulation. *Journal of Geophysical Research: Atmospheres* 112, D10117. doi:10.1029/2006JD007506.

Baldocchi, D., Falge, E., Gu, L., Olson, R., Hollinger, D., Running, S., Anthoni, P., Bernhofer, C., Davis, K., and Evans, R. 2001. FLUXNET: A new tool to study the temporal and spatial variability of ecosystem-scale carbon dioxide, water vapor, and energy flux densities. *Bulletin of the American Meteorological Society* 82, 2415–2434.

Baret, F. and Buis, S. 2008. Estimating canopy characteristics from remote sensing observations: Review of methods and associated problems. In: *Advances in Land Remote Sensing*, New York, USA, pp. 173–201.

Bastiaanssen, W.G.M., Ahmad, M.D., and Chemin, Y. 2002. Satellite surveillance of evaporative depletion across the Indus Basin. *Water Resources Research* 38, 1273. doi:10.1029/2001WR000386.

Bastiaanssen, W.G.M., Menenti, M., Feddes, R.A., and Holtslag, A.A.M. 1998. A remote sensing surface energy balance algorithm for land (SEBAL) 1. Formulation. *Journal of Hydrology* 212–213, 198–212.

Bastiaanssen, W.G.M., Noordman, E.J.M., Pelgrum, H., Davids, G., Thoreson, B.P., and Allen, R.G. 2005. SEBAL model with remotely sensed data to improve water-resources management under actual field conditions. *Journal of Irrigation and Drainage Engineering* 131, 85–93.

Bausch, W.C. and Neale, C.M.U. 1987. Crop coefficients derived from reflected canopy radiation: A Concept. *American Society of Agricultural Engineers* 30, 703–709.

Beven, K. 2006a. A manifesto for the equifinality thesis. *Journal of Hydrology* 320, 18–36.

Beven, K. 2006b. On undermining the science? *Hydrological Processes* 20, 3141–3146.

Bhattacharya, B.K., Mallick, K., Patel, N.K., and Parihar, J.S. 2010. Regional clear sky evapotranspiration over agricultural land using remote sensing data from Indian geostationary meteorological satellite. *Journal of Hydrology* 387, 65–80.

Biggs, T.W., Thenkabail, P.S., Gumma, M.K., Scott, C. a., Parthasaradhi, G.R., and Turral, H.N. 2006. Irrigated area mapping in heterogeneous landscapes with MODIS time series, ground truth and census data, Krishna Basin, India. *International Journal of Remote Sensing* 27, 4245–4266. doi:10.1080/01431160600851801.

Bindhu, V.M., Narasimhan, B., and Sudheer, K.P. 2013. Development and verification of a non-linear disaggregation method (NL-DisTrad) to downscale MODIS land surface temperature to the spatial scale of Landsat thermal data to estimate evapotranspiration. *Remote Sensing of Environment* 135, 118–129. doi:http://dx.doi.org/10.1016/j.rse.2013.03.023.

Bisht, G. and Bras, R.L. 2010. Estimation of net radiation from the MODIS data under all sky conditions: Southern Great Plains case study. *Remote Sensing of Environment* 114, 1522–1534. doi:http://dx.doi.org/10.1016/j.rse.2010.02.007.

Bisht, G., Venturini, V., Islam, S., and Jiang, L. 2005. Estimation of the net radiation using MODIS (Moderate Resolution Imaging Spectroradiometer) data for clear sky days. *Remote Sensing of Environment* 97, 52–67.

Bonan, G.B. 1998. The land surface climatology of the NCAR land surface model coupled to the NCAR community climate model. *Journal of Climate* 11, 1307–1326.

AQ11 Bosilovich, M. 2008. NASA's modern era retrospective-analysis for research and applications: Integrating Earth observations. *Earthzine* 26 [Online].

Brunsell, N.A. and Gillies, R.R. 2003. Scale issues in land–atmosphere interactions: implications for remote sensing of the surface energy balance. *Agricultural and Forest Meteorology* 117, 203–221.

Cammalleri, C., Anderson, M.C., Gao, F., Hain, C.R., and Kustas, W.P. 2013. A data fusion approach for mapping daily evapotranspiration at field scale. *Water Resources Research* 49, 4672–4686. doi:10.1002/wrcr.20349.

Cammalleri, C., Anderson, M.C., Gao, F., Hain, C.R., and Kustas, W.P. 2014. Mapping daily evapotranspiration at field scales over rainfed and irrigated agricultural areas using remote sensing data fusion. *Agricultural and Forest Meteorology* 186, 1–11. doi:http://dx.doi.org/10.1016/j.agrformet.2013.11.001.

Campos, I., Neale, C.M.U., Calera, A., Balbontín, C., and González-Piqueras, J. 2010. Assessing satellite-based basal crop coefficients for irrigated grapes (*Vitis vinifera* L.). *Agricultural Water Management* 98, 45–54. doi:http://dx.doi.org/10.1016/j.agwat.2010.07.011.

Carlson, T. 2007. An overview of the "triangle method" for estimating surface evapotranspiration and soil moisture from satellite imagery. *Sensors* 7, 1612–1629.

Carlson, T.N., Gillies, R.R., and Schmugge, T.J. 1995. An interpretation of methodologies for indirect measurement of soil water content. *Agricultural and Forest Meteorology* 77, 191–205. doi:http://dx.doi.org/10.1016/0168-1923(95)02261-U.

Chávez, J., Neale, C.U., Prueger, J., and Kustas, W. 2008. Daily evapotranspiration estimates from extrapolating instantaneous airborne remote sensing ET values. *Irrigation Science* 27, 67–81. doi:10.1007/s00271-008-0122-3.

Chávez, J.L., Neale, C.M.U., Hipps, L.E., Prueger, J.H., and Kustas, W.P. 2005. Comparing aircraft-based remotely sensed energy balance fluxes with eddy covariance tower data using heat flux source area functions. *Journal of Hydrometeorology* 6, 923–940.

Chen, F., Janjić, Z., and Mitchell, K. 1997. Impact of atmospheric surface-layer parameterizations in the new land-surface scheme of the NCEP mesoscale Eta model. *Boundary-Layer Meteorology* 85, 391–421.

Chen, F., Mitchell, K., Schaake, J., Xue, Y., Pan, H., Koren, V., Duan, Q.Y., Ek, M., and Betts, A. 1996. Modeling of land surface evaporation by four schemes and comparison with FIFE observations. *Journal of Geophysical Research: Atmospheres* (1984–2012) 101, 7251–7268.

Chen, J.-H., Kan, C.-E., Tan, C.-H., and Shih, S.-F. 2002. Use of spectral information for wetland evapotranspiration assessment. *Agricultural Water Management* 55, 239–248.

Chen, Y., Xia, J., Liang, S., Feng, J., Fisher, J.B., Li, X., Li, X. et al. 2014. Comparison of satellite-based evapotranspiration models over terrestrial ecosystems in China. *Remote Sensing of Environment* 140, 279–293. doi:http://dx.doi.org/10.1016/j.rse.2013.08.045.

Choi, M., Kustas, W.P., Anderson, M.C., Allen, R.G., Li, F., and Kjaersgaard, J.H. 2009. An intercomparison of three remote sensing-based surface energy balance algorithms over a corn and soybean production region (Iowa, US) during SMACEX. *Agricultural and Forest Meteorology* 149, 2082–2097.

Choudhury, B.J. 1989. Estimating evaporation and carbon assimilation using infrared temperature data. In: *Theory and Applications of Optical Remote Sensing*, Asrar, G. (ed.), pp. 628–690. New York: Wiley-Interscience.

Choudhury, B.J., Ahmed, N.U., Idso, S.B., Reginato, R.J., and Daughtry, C.S.T. 1994. Relations between evaporation coefficients and vegetation indices studied by model simulations. *Remote Sensing of Environment* 50, 1–17.

Cleugh, H.A., Leuning, R., Mu, Q., and Running, S.W. 2007. Regional evaporation estimates from flux tower and MODIS satellite data. *Remote Sensing of Environment* 106, 285–304.

Clothier, B.E., Clawson, K.L., Pinter, P.J., Moran, M.S., Reginato, R.J., and Jackson, R.D. 1986. Estimation of soil heat flux from net radiation during the growth of alfalfa. *Agricultural and Forest Meteorology* 37, 319–329. doi:10.1016/0168-1923(86)90069-9.

Conrad, C., Dech, S., Hafeez, M., Lamers, J., Martius, C., and Strunz, G. 2007. Mapping and assessing water use in a Central Asian irrigation system by utilizing MODIS remote sensing products. *Irrigation and Drainage Systems* 21, 197–218. doi:10.1007/s10795-007-9029-z.

Courault, D., Seguin, B., and Olioso, A. 2005. Review on estimation of evapotranspiration from remote sensing data: From empirical to numerical modeling approaches. *Irrigation and Drainage Systems* 19, 223–249.

Crago, R.D. 1996. Conservation and variability of the evaporative fraction during the daytime. *Journal of Hydrology* 180, 173–194. doi:http://dx.doi.org/10.1016/0022-1694(95)02903-6.

Duchemin, B., Hadria, R., Erraki, S., Boulet, G., Maisongrande, P., Chehbouni, A., Escadafal, R., Ezzahar, J., Hoedjes, J.C.B., and Kharrou, M.H. 2006. Monitoring wheat phenology and irrigation in Central Morocco: On the use of relationships between evapotranspiration, crops coefficients, leaf area index and remotely-sensed vegetation indices. *Agricultural Water Management* 79, 1–27.

El-Shikha, D.M., Waller, P., Hunsaker, D., Clarke, T., and Barnes, E. 2007. Ground-based remote sensing for assessing water and nitrogen status of broccoli. *Agricultural Water Management* 92, 183–193.

Engman, E.T. and Gurney, R.J. 1991. Recent advances and future implications of remote sensing for hydrologic modeling. In: *Recent Advances in the Modeling of Hydrologic Systems*, Bowles, D.S., (ed.), pp. 471–495. Dordrecht, the Netherlands: Kluwer Academic Publishers.

Er-Raki, S., Chehbouni, A., Hoedjes, J., Ezzahar, J., Duchemin, B., and Jacob, F. 2008. Improvement of FAO-56 method for olive orchards through sequential assimilation of thermal infrared-based estimates of ET. *Agricultural Water Management* 95, 309–321.

Ershadi, A., McCabe, M.F., Evans, J.P., Chaney, N.W., and Wood, E.F. 2014. Multi-site evaluation of terrestrial evaporation models using FLUXNET data. *Agricultural and Forest Meteorology* 187, 46–61. doi:http://dx.doi.org/10.1016/j.agrformet.2013.11.008.

Ershadi, A., McCabe, M.F., Evans, J.P., and Walker, J.P. 2013. Effects of spatial aggregation on the multi-scale estimation of evapotranspiration. *Remote Sensing of Environment* 131, 51–62. doi:http://dx.doi.org/10.1016/j.rse.2012.12.007.

Evett, S.R., Kustas, W.P., Gowda, P.H., Anderson, M.C., Prueger, J.H., and Howell, T.A. 2012. Overview of the bushland evapotranspiration and agricultural remote sensing experiment 2008 (BEAREX08): A field experiment evaluating methods for quantifying ET at multiple scales. *Advances in Water Resources* 50, 4–19.

Farah, H.O., Bastiaanssen, W.G.M., and Feddes, R.A. 2004. Evaluation of the temporal variability of the evaporative fraction in a tropical watershed. *International Journal of Applied Earth Observation and Geoinformation* 5, 129–140.

Fisher, J.B., Tu, K.P., and Baldocchi, D.D. 2008. Global estimates of the land–atmosphere water flux based on monthly AVHRR and ISLSCP-II data, validated at 16 FLUXNET sites. *Remote Sensing of Environment* 112, 901–919.

Foley, J.A., DeFries, R., Asner, G.P., Barford, C., Bonan, G., Carpenter, S.R., Chapin, F.S. et al. 2005. Global consequences of land use. *Science* 309, 570–574. doi:10.1126/science.1111772.

Foley, J.A., Ramankutty, N., Brauman, K.A., Cassidy, E.S., Gerber, J.S., Johnston, M., Mueller, N.D. et al. 2011. Solutions for a cultivated planet. *Nature* 478, 337–342. doi:10.1038/nature10452.

Franks, S.W., Beven, K.J., Quinn, P.F., and Wright, I.R. 1997. On the sensitivity of the soil-vegetation-atmosphere transfer (SVAT) schemes: Equifinality and the problem of robust calibration. *Agricultural and Forest Meteorology* 86, 63–75.

French, A.N., Alfieri, J.G., Kustas, W.P., Prueger, J.H., Hipps, L.E., Chávez, J.L., Evett, S.R. et al. 2012. Estimation of surface energy fluxes using surface renewal and flux variance techniques over an advective irrigated agricultural site. *Advances in Water Resources* 50, 91–105. doi:http://dx.doi.org/10.1016/j.advwatres.2012.07.007.

Galleguillos, M., Jacob, F., Prévot, L., French, A., and Lagacherie, P. 2011. Comparison of two temperature differencing methods to estimate daily evapotranspiration over a Mediterranean vineyard watershed from ASTER data. *Remote Sensing of Environment* 115, 1326–1340.

Gao, F., Kustas, W.P., and Anderson, M.C. 2012. A data mining approach for sharpening thermal satellite imagery over land. *Remote Sensing* 4, 3287–3319.

Gao, F., Masek, J., Schwaller, M., and Hall, F. 2006. On the blending of the Landsat and MODIS surface reflectance: Predicting daily Landsat surface reflectance. *Geoscience and Remote Sensing, IEEE Transactions on* 44, 2207–2218.

García, M., Villagarcía, L., Contreras, S., Domingo, F., and Puigdefábregas, J. 2007. Comparison of three operative models for estimating the surface water deficit using ASTER reflective and thermal data. *Sensors* 7, 860–883.

Gentine, P., Entekhabi, D., Chehbouni, A., Boulet, G., and Duchemin, B. 2007. Analysis of evaporative fraction diurnal behaviour. *Agricultural and Forest Meteorology* 143, 13–29. doi:http://dx.doi.org/10.1016/j.agrformet.2006.11.002.

Gillies, R.R. and Carlson, T.N. 1995. Thermal remote sensing of surface soil water content with partial vegetation cover for incorporation into climate models. *Journal of Applied Meteorology* 34, 745–756.

Gillies, R.R., Kustas, W.P., and Humes, K.S. 1997. A verification of the 'triangle' method for obtaining surface soil water content and energy fluxes from remote measurements of the Normalized Difference Vegetation Index (NDVI) and surface radiant temperature. *International Journal of Remote Sensing* 18, 3145–3166.

Glenn, E.P., Huete, A.R., Nagler, P.L., Hirschboeck, K.K., and Brown, P. 2007. Integrating remote sensing and ground methods to estimate evapotranspiration. *Critical Reviews in Plant Sciences* 26, 139–168.

Glenn, E.P., Huete, A.R., Nagler, P.L., and Nelson, S.G. 2008a. Relationship between remotely-sensed vegetation indices, canopy attributes and plant physiological processes: What vegetation indices can and cannot tell us about the landscape. *Sensors* 8, 2136–2160.

Glenn, E.P., Mexicano, L., Garcia-Hernandez, J., Nagler, P.L., Gomez-Sapiens, M.M., Tang, D., Lomeli, M.A., Ramirez-Hernandez, J., and Zamora-Arroyo, F. 2013. Evapotranspiration and water balance of an anthropogenic coastal desert wetland: Responses to fire, inflows and salinities. *Ecological Engineering* 59, 176–184.

Glenn, E.P., Morino, K., Didan, K., Jordan, F., Carroll, K., Nagler, P.L., Hultine, K., Sheader, L., and Waugh, J. 2008b. Scaling sap flux measurements of grazed and ungrazed shrub communities with fine and coarse-resolution remote sensing. *Ecohydrology* 1, 316–329.

Glenn, E.P., Nagler, P.L., and Huete, A.R. 2010. Vegetation index methods for estimating evapotranspiration by remote sensing. *Surveys in Geophysics* 31, 531–555.

AQ12 Glenn, E.P., Nagler, P.L., Morino, K., and Hultine, K.R. 2013. Phreatophytes under stress: transpiration and stomatal conductance of saltcedar (*Tamarix* spp.) in a high-salinity environment. *Plant and Soil* 371, 655–672.

Glenn, E.P., Neale, C.M.U., Hunsaker, D.J., and Nagler, P.L. 2011. Vegetation index-based crop coefficients to estimate evapotranspiration by remote sensing in agricultural and natural ecosystems. *Hydrological Processes* 25, 4050–4062. doi:10.1002/hyp.8392.

Gómez, M., Olioso, A., Sobrino, J.A., and Jacob, F. 2005. Retrieval of evapotranspiration over the Alpilles/ReSeDA experimental site using airborne POLDER sensor and a thermal camera. *Remote Sensing of Environment* 96, 399–408.

Gontia, N.K. and Tiwari, K.N. 2010. Estimation of crop coefficient and evapotranspiration of wheat (*Triticum aestivum*) in an irrigation command using remote sensing and GIS. *Water Resources Management* 24, 1399–1414.

González-Dugo, M.P., and Mateos, L. 2008. Spectral vegetation indices for benchmarking water productivity of irrigated cotton and sugarbeet crops. *Agricultural Water Management* 95, 48–58.

Gonzalez-Dugo, M.P., Neale, C.M.U., Mateos, L., Kustas, W.P., Prueger, J.H., Anderson, M.C., and Li, F. 2009. A comparison of operational remote sensing-based models for estimating crop evapotranspiration. *Agricultural and Forest Meteorology* 149, 1843–1853.

Gottschalck, J., Meng, J., Rodell, M., and Houser, P. 2005. Analysis of multiple precipitation products and preliminary assessment of their impact on global land data assimilation system land surface states. *Journal of Hydrometeorology* 6, 573–598. doi:10.1175/JHM437.1.

Gowda, P., Chavez, J., Colaizzi, P., Evett, S., Howell, T., and Tolk, J. 2008. ET mapping for agricultural water management: Present status and challenges. *Irrigation Science* 26, 223–237. doi:10.1007/s00271-007-0088-6.

Granger, R.J. and Gray, D.M. 1989. Evaporation from natural nonsaturated surfaces. *Journal of Hydrology* 111, 21–29.

Gui, S., Liang, S., and Li, L. 2010. Evaluation of satellite-estimated surface longwave radiation using ground-based observations. *Journal of Geophysical Research* 115, D18214. doi:10.1029/2009JD013635.

Gupta, S.K., Ritchey, N.A., Wilber, A.C., Whitlock, C.H., Gibson, G.G., and Stackhouse, P.W.J. 1999. A climatology of surface radiation budget derived from satellite data. *Journal of Climate* 12, 2691–2710.

Hall, F.G., Huemmrich, K.F., Goetz, S.J., Sellers, P.J., and Nickeson, J.E. 1992. Satellite remote sensing of surface energy balance: Success, failures, and unresolved issues in FIFE. *Journal of Geophysical Research: Atmospheres* 97, 19061–19089. doi:10.1029/92JD02189.

Hoekstra, A.Y. and Mekonnen, M.M. 2012. The water footprint of humanity. *Proceedings of the National Academy of Sciences of the United States of America* 109, 3232–3237. doi:10.1073/pnas.1109936109.

Hook, S.J. and Green, R.O. 2013. *2013 HyspIRI Science Workshop: Objectives, Overview and Update*. Pasadena, CA: Jet Propulsion Laboratory, California Institute of Technology.

Hunsaker, D.J., Fitzgerald, G.J., French, A.N., Clarke, T.R., Ottman, M.J., and Pinter Jr., P.J. 2007a. Wheat irrigation management using multispectral crop coefficients. I. Crop evapotranspiration prediction. *Transactions of the American Society of Agricultural and Biological Engineers* 50, 2017–2033.

Hunsaker, D.J., Fitzgerald, G.J., French, A.N., Clarke, T.R., Ottman, M.J., and Pinter Jr., P.J. 2007b. Wheat irrigation management using multispectral crop coefficients: II. Irrigation scheduling performance, grain yield, and water use efficiency. *Transactions of the American Society of Agricultural and Biological Engineers* 50, 2035–2050.

Hunsaker, D.J., French, A.N., Clarke, T.R., and El-Shikha, D.M. 2011. Water use, crop coefficients, and irrigation management criteria for camelina production in arid regions. *Irrigation Science* 29, 27–43. doi:10.1007/s00271-010-0213-9.

Hunsaker, D.J., Pinter Jr, P.J., and Kimball, B.A. 2005. Wheat basal crop coefficients determined by normalized difference vegetation index. *Irrigation Science* 24, 1–14.

Idso, S.B. 1981. A set of equations for full spectrum and 8-to 14-μm and 10.5-to 12.5-μm thermal radiation from cloudless skies. *Water Resources Research* 17, 295–304.

Jackson, R.D., Hatfield, J.L., Reginato, R.J., Idso, S.B., and Pinter Jr, P.J. 1983. Estimation of daily evapotranspiration from one time-of-day measurements. *Agricultural Water Management* 7, 351–362.

Jackson, R.D., Idso, S.B., Reginato, R.J., and Pinter, P.J. 1981. Canopy temperature as a crop water stress indicator. *Water Resources Research* 17, 1133–1138.

Jayanthi, H., Neale, C.M.U., and Wright, J.L. 2007. Development and validation of canopy reflectance-based crop coefficient for potato. *Agricultural Water Management* 88, 235–246. doi:10.1016/j.agwat.2006.10.020.

Jiang, L. and Islam, S. 1999. A methodology for estimation of surface evapotranspiration over large areas using remote sensing observations. *Geophysical Research Letters* 26, 2773–2776.

Jiang, L. and Islam, S. 2003. An intercomparison of regional latent heat flux estimation using remote sensing data. *International Journal of Remote Sensing* 24, 2221–2236. doi:10.1080/01431160210154821.

Jiang, L. and Islam, S. 2001. Estimation of surface evaporation map over southern great plains using remote sensing data. *Water Resources Research* 37, 329–340.

Jiang, L., Islam, S., and Carlson, T.N. 2004. Uncertainties in latent heat flux measurement and estimation: implications for using a simplified approach with remote sensing data. *Canadian Journal of Remote Sensing* 30, 769–787.

Johnson, L.F. and Trout, T.J. 2012. Satellite NDVI assisted monitoring of vegetable crop evapotranspiration in California's San Joaquin Valley. *Remote Sensing* 4, 439–455.

Jung, M., Reichstein, M., and Bondeau, A. 2009. Towards global empirical upscaling of FLUXNET eddy covariance observations: Validation of a model tree ensemble approach using a biosphere model. *Biogeosciences* 6, 2001–2013. doi:10.5194/bg-6-2001-2009.

Jung, M., Reichstein, M., Margolis, H.A., Cescatti, A., Richardson, A.D., Arain, M.A., Arneth, A. et al. 2011. Global patterns of land-atmosphere fluxes of carbon dioxide, latent heat, and sensible heat derived from eddy covariance, satellite, and meteorological observations. *Journal of Geophysical Research* 116, G00J07. doi:10.1029/2010JG001566.

Kalma, J.D., McVicar, T.R., and McCabe, M.F. 2008. Estimating land surface evaporation: A review of methods using remotely sensed surface temperature data. *Surveys in Geophysics* 29, 421–469.

Kalnay, E., Kanamitsu, M., Kistler, R., Collins, W., Deaven, D., Gandin, L., Iredell, M. et al. 1996. The NCEP/NCAR 40-year reanalysis project. *Bulletin of the American Meteorological Society* 77, 437–472.

Kjaersgaard, J., Allen, R., Garcia, M., Kramber, W., and Trezza, R. 2009. Automated selection of anchor pixels for landsat based evapotranspiration estimation. In: *World Environmental and Water Resources Congress 2009*, pp. 1–11. Reston, VA: American Society of Civil Engineers. doi:doi:10.1061/41036(342)442.

Kjaersgaard, J., Allen, R.G., and Irmak, A. 2011. Improved methods for estimating monthly and growing season ET using METRIC applied to moderate resolution satellite imagery. *Hydrological Processes* 25, 4028–4036. doi:10.1002/hyp.8394.

Koster, R.D. and Suarez, M.J. 1996. Energy and water balance calculations in the Mosaic LSM. *NASA Tech. Memo* 104606, 59.

Kustas, W.P. and Daughtry, C. 1990. Estimation of the soil heat flux/net radiation ratio from spectral data. *Agricultural and Forest Meteorology* 49, 205–223. doi:10.1016/0168-1923(90)90033-3.

Kustas, W.P., Hatfield, J.L., and Prueger, J.H. 2005. The soil moisture–atmosphere coupling experiment (SMACEX): Background, hydrometeorological conditions, and preliminary findings. *Journal of Hydrometeorology* 6, 791–804.

Kustas, W.P., Jackson, T.J., Schmugge, T.J., Parry, R., Goodrich, D.C., Amer, S.A., Bach, L.B., Keefer, T.O., Weltz, M.A., and Moran, M.S. 1991. An interdisciplinary field study of the energy and water fluxes in the atmospheric-biosphere system over semiarid rangelands: Description and some preliminary results. *Bulletin of the American Meteorological Society* 72, 1683–1705.

Kustas, W.P., Li, F., Jackson, T.J., Prueger, J.H., MacPherson, J.I., and Wolde, M. 2004. Effects of remote sensing pixel resolution on modeled energy flux variability of croplands in Iowa. *Remote Sensing of Environment* 92, 535–547.

Kustas, W.P. and Norman, J.M. 1999. Evaluation of soil and vegetation heat flux predictions using a simple two-source model with radiometric temperatures for partial canopy cover. *Agricultural and Forest Meteorology* 94, 13–29.

Kustas, W.P. and Norman, J.M. 1996. Use of remote sensing for evapotranspiration monitoring over land surfaces. *Hydrological Sciences Journal* 41, 495–516. doi:10.1080/02626669609491522.

Kustas, W.P., Norman, J.M., Anderson, M.C., and French, A.N. 2003. Estimating subpixel surface temperatures and energy fluxes from the vegetation index–radiometric temperature relationship. *Remote Sensing of Environment* 85, 429–440. doi:http://dx.doi.org/10.1016/S0034-4257(03)00036-1.

Lee, E., Chase, T.N., Rajagopalan, B., Barry, R.G., Biggs, T.W., and Lawrence, P.J. 2009. Effects of irrigation and vegetation activity on early Indian summer monsoon variability. *International Journal of Climatology* 29, 573–581.

Lee, E., Sacks, W.J., Chase, T.N., and Foley, J.A. 2011. Simulated impacts of irrigation on the atmospheric circulation over Asia. *Journal of Geophysical Research: Atmospheres* (1984–2012) 116, D08114. doi:10.1029/2010JD014740.

Leuning, R., Zhang, Y.Q., Rajaud, A., Cleugh, H., and Tu, K. 2008. A simple surface conductance model to estimate regional evaporation using MODIS leaf area index and the Penman–Monteith equation. *Water Resources Research* 44, W10419. doi:10.1029/2007WR006562.

Lhomme, J.-P. and Elguero, E. 1999. Examination of evaporative fraction diurnal behaviour using a soil-vegetation model coupled with a mixed-layer model. *Hydrology and Earth System Sciences* 3, 259–270.

Li, H., Zheng, L., Lei, Y., Li, C., Liu, Z., and Zhang, S. 2008. Estimation of water consumption and crop water productivity of winter wheat in North China Plain using remote sensing technology. *Agricultural Water Management* 95, 1271–1278.

Liang, S., Wang, K., Zhang, X., and Wild, M. 2010. Review on estimation of land surface radiation and energy budgets from ground measurement, remote sensing and model simulations. *IEEE Journal of Selected Topics in Applied Earth Observations and Remote Sensing* 3, 225–240.

Liang, S., Zhang, X., He, T., Cheng, J., and Wang, D. 2013. Remote sensing of the land surface radiation budget. In: *Remote Sensing of Energy Fluxes and Soil Moisture Content*, Petropoulos, G.P. (ed.), pp. 121–162. New York: Taylor and Francis.

Liang, X., Lettenmaier, D.P., Wood, E.F., and Burges, S.J. 1994. A simple hydrologically based model of land surface water and energy fluxes for general circulation models. *Journal of Geophysical Research* 99, 14, 414–415, 428.

Long, D. and Singh, V.P. 2010. Integration of the GG model with SEBAL to produce time series of evapotranspiration of high spatial resolution at watershed scales. *Journal of Geophysical Research* 115, D21128. doi:10.1029/2010jd014092.

Long, D., Singh, V.P., and Li, Z.-L. 2011. How sensitive is SEBAL to changes in input variables, domain size and satellite sensor? *Journal of Geophysical Research* 116, D21107. doi:10.1029/2011jd016542.

Ma, Y. and Pinker, R.T. 2012. Modeling shortwave radiative fluxes from satellites. *Journal of Geophysical Research* 117, D23202. doi:10.1029/2012JD018332.

Marshall, M., Tu, K., Funk, C., Michaelsen, J., Williams, P., Williams, C., Ardö, J. et al. 2013. Improving operational land surface model canopy evapotranspiration in Africa using a direct remote sensing approach. *Hydrology and Earth System Science* 17, 1079–1091. doi:10.5194/hess-17-1079-2013.

McCabe, M.F., Kalma, J.D., and Franks, S.W. 2005. Spatial and temporal patterns of land surface fluxes from remotely sensed surface temperatures within an uncertainty modelling framework. *Hydrology and Earth System Sciences* 9, 467–480.

McCabe, M.F. and Wood, E.F. 2006. Scale influences on the remote estimation of evapotranspiration using multiple satellite sensors. *Remote Sensing of Environment* 105, 271–285.

Medlyn, B.E., Robinson, A.P., Clement, R., and McMurtrie, R.E. 2005. On the validation of models of forest CO2 exchange using eddy covariance data: some perils and pitfalls. *Tree Physiology* 25, 839–857.

Melesse, A.M., Frank, A., Nangia, V., and Hanson, J. 2008. Analysis of energy fluxes and land surface parameters in a grassland ecosystem: A remote sensing perspective. *International Journal of Remote Sensing* 29, 3325–3341.

Messina, A. 2012. Mapping drought in the Krishna Basin with remote sensing. Mapping drought in the Krishna Basin with remote sensing, San Diego State University.

Meyers, T.P. and Hollinger, S.E. 2004. An assessment of storage terms in the surface energy balance of maize and soybean. *Agricultural and Forest Meteorology* 125, 105–115.

Moran, M.S., Clarke, T.R., Inoue, Y., and Vidal, A. 1994. Estimating crop water deficit using the relation between surface-air temperature and spectral vegetation index. *Remote Sensing of Environment* 49, 246–263.

Moran, M.S. and Jackson, R.D. 1991. Assessing the spatial distribution of evapotranspiration using remotely sensed inputs. *Journal of Environment Quality* 20, 725–737. doi:10.2134/jeq1991.00472425002000040003x.

Moran, M.S., Rahman, A.F., Washburne, J.C., Goodrich, D.C., Weltz, M.A., and Kustas, W.P. 1996. Combining the Penman–Monteith equation with measurements of surface temperature and reflectance to estimate evaporation rates of semiarid grassland. *Agricultural and Forest Meteorology* 80, 87–109.

Morcrette, J. 1991. Radiation and cloud radiative properties in the European Centre for Medium Range Weather Forecasts forecasting system. *Journal of Geophysical Research: Atmospheres* (1984–2012) 96, 9121–9132.

Morcrette, J.-J. 2002. The surface downward longwave radiation in the ECMWF forecast system. *Journal of Climate* 15, 1875–1892.

Morillas, L., Leuning, R., Villagarcía, L., García, M., Serrano-Ortiz, P., and Domingo, F. 2013. Improving evapotranspiration estimates in Mediterranean drylands: The role of soil evaporation. *Water Resources Research* 49, 6572–6586. doi:10.1002/wrcr.20468.

Morse, A., Tasumi, M., Allen, R.G., and Kramber, W.J. 2000. Application of the SEBAL methodology for estimating consumptive use of water and streamflow depletion in the Bear River Basin of Idaho through remote sensing.   AQ13

Mu, Q. 2013. MODIS 1-km^2 terrestrial evapotranspiration (ET) product for the Nile Basin algorithm theoretical basis document.

Mu, Q., Heinsch, F.A., Zhao, M., and Running, S.W. 2007. Development of a global evapotranspiration algorithm based on MODIS and global meteorology data. *Remote Sensing of Environment* 111, 519–536.

Mu, Q., Zhao, M., and Running, S.W. 2011. Improvements to a MODIS global terrestrial evapotranspiration algorithm. *Remote Sensing of Environment* 115, 1781–1800.

Murray, T. and Verhoef, A. 2007. Moving towards a more mechanistic approach in the determination of soil heat flux from remote measurements: I. A universal approach to calculate thermal inertia. *Agricultural and Forest Meteorology* 147, 80–87. doi:http://dx.doi.org/10.1016/j.agrformet.2007.07.004.

Nagler, P.L., Glenn, E.P., Nguyen, U., Scott, R.L., and Doody, T. 2013. Estimating riparian and agricultural actual evapotranspiration by reference evapotranspiration and MODIS enhanced vegetation index. *Remote Sensing* 5, 3849–3871. doi:10.3390/rs5083849.

Nagler, P.L., Morino, K., Murray, R.S., Osterberg, J., and Glenn, E.P. 2009. An empirical algorithm for estimating agricultural and riparian evapotranspiration using MODIS enhanced vegetation index and ground measurements of ET. I. Description of method. *Remote Sensing* 1, 1273–1297.

Neale, C.M.U., Bausch, W.C., and Heermann, D.F. 1989. Development of reflectance-based crop coefficients for corn. *Transactions of the American Society of Agricultural Engineers* 32, 1891–1899.

Nishida, K. 2003. An operational remote sensing algorithm of land surface evaporation. *Journal of Geophysical Research: Atmospheres (1984–2012)* 108, 4270. doi:10.1029/2002JD002062.   AQ14

Nishida, K. and Nemani, R. 2003. Development of an evapotranspiration index from Aqua/MODIS for monitoring surface moisture status. *IEEE Transactions on Geoscience and Remote Sensing* 41, 493–501.

Norman, J.M., Anderson, M.C., Kustas, W.P., French, A.N., Mecikalski, J., Torn, R., Diak, G.R., Schmugge, T.J., and Tanner, B.C.W. 2003. Remote sensing of surface energy fluxes at 10 1-m pixel resolutions. *Water Resources Research* 39, 1221. doi:10.1029/2002WR001775.

Norman, J.M., Kustas, W.P., and Humes, K.S. 1995. Source approach for estimating soil and vegetation energy fluxes in observations of directional radiometric surface temperature. *Agricultural and Forest Meteorology* 77, 263–293.

Petropoulos, G., Carlson, T.N., Wooster, M.J., and Islam, S. 2009. A review of Ts/VI remote sensing based methods for the retrieval of land surface energy fluxes and soil surface moisture. *Progress in Physical Geography* 33, 224–250.

AQ15   Petropoulos, G., Wooster, M.J., Carlson, T.N., and Drake, N. 2010. Synergy of the SimSphere land surface process model with ASTER imagery for the retrieval of spatially distributed estimates of surface turbulent heat fluxes and soil moisture content. In: *EGU General Assembly Conference Abstracts*, p. 906.

Petropoulos, G.P. 2013. Remote sensing of surface turbulent energy fluxes. In: *Remote Sensing of Energy Fluxes and Soil Moisture Content*, Petropoulos, G.P. (ed.), pp. 49–84. New York: Taylor and Francis.

Petropoulos, G.P. and Carlson, T.N. 2011. Retrievals of turbulent heat fluxes and surface soil water content by remote sensing. In: *Advances in Environmental Remote Sensing: Sensors, Algorithms, and Applications*, Weng, Q. (ed), p. 469. New York: CRC Press.

Petropoulos, G.P., Carlson, T.N., and Griffiths, H.M. 2013. Turbulent fluxes of heat and moisture at the Earth's land surfade: Importance, controlling parameters, and conventional measurement techniques. In: *Remote Sensing of Energy Fluxes and Soil Moisture Content*, Petropoulos, G.P. (ed.), pp. 3–28. New York: CRC Press.

Rafn, E.B., Contor, B., and Ames, D.P. 2008. Evaluation of a method for estimating irrigated crop-evapotranspiration coefficients from remotely sensed data in Idaho. *Journal of Irrigation and Drainage Engineering* 134, 722–729.

Rienecker, M.M., Suarez, M.J., Gelaro, R., Todling, R., Bacmeister, J., Liu, E., Bosilovich, M.G. et al. 2011. MERRA: NASA's modern-era retrospective analysis for research and applications. *Journal of Climate* 24, 3624–3648.

Rivas, R. and Caselles, V. 2004. A simplified equation to estimate spatial reference evaporation from remote sensing-based surface temperature and local meteorological data. *Remote Sensing of Environment* 93, 68–76.

Rodell, M., Houser, P.R., Jambor, U., Gottschalck, J., Mitchell, K., Meng, C.-J., Arsenault, K. et al. 2004. The global land data assimilation system. *Bulletin of the American Meteorological Society* 85, 381–394. doi:10.1175/BAMS-85-3-381.

Roerink, G., Su, Z., and Menenti, M. 2000. S-SEBI: A simple remote sensing algorithm to estimate the surface energy balance. *Physics and Chemistry of the Earth, Part B: Hydrology, Oceans and Atmosphere* 25, 147–157. doi:10.1016/S1464-1909(99)00128-8.

Romero, M.G. 2004. Daily evapotranspiration estimation by means of evaporative fraction and reference evapotranspiration fraction. Daily evapotranspiration estimation by means of evaporative fraction and reference evapotranspiration fraction, Utah State University, Department of Biological and Irrigation Engineering.

Rossow, W.B. and Schiffer, R.A. 1999. Advances in understanding clouds from ISCCP. *Bulletin of the American Meteorological Society* 80, 2261–2287.

Rossow, W.B. and Schiffer, R.A. 1991. ISCCP cloud data products. *Bulletin of the American Meteorological Society* 72, 2–20.

Samani, Z., Bawazir, a. S., Bleiweiss, M., Skaggs, R., Longworth, J., Tran, V.D., and Pinon, A. 2009. Using remote sensing to evaluate the spatial variability of evapotranspiration and crop coefficient in the lower Rio Grande Valley, New Mexico. *Irrigation Science* 28, 93–100. doi:10.1007/s00271-009-0178-8.

Schiffer, R.A. and Rossow, W.B. 1983. The international satellite cloud climatology project (ISCCP)—The first project of the World Climate Research Programme. *American Meteorological Society, Bulletin* 64, 779–784.

Scott, R.L. 2010. Using watershed water balance to evaluate the accuracy of eddy covariance evaporation measurements for three semiarid ecosystems. *Agricultural and Forest Meteorology* 150, 219–225.

Scott, R.L., Huxman, T.E., Cable, W.L., and Emmerich, W.E. 2006. Partitioning of evapotranspiration and its relation to carbon dioxide exchange in a Chihuahuan Desert shrubland. *Hydrological Processes* 20, 3227–3243.

Sellers, P.J., Randall, D.A., Collatz, G.J., Berry, J.A., Field, C.B., Dazlich, D.A., Zhang, C., Collelo, G.D., and Bounoua, L. 1996. A revised land surface parameterization (SiB2) for atmospheric GCMs. Part I: Model formulation. *Journal of Climate* 9, 676–705.

Senay, G., Budde, M., Verdin, J., and Melesse, A. 2007. A coupled remote sensing and simplified surface energy balance approach to estimate actual evapotranspiration from irrigated fields. *Sensors* 7, 979–1000.

Senay, G.B., Bohms, S., Singh, R.K., Gowda, P.H., Velpuri, N.M., Alemu, H., and Verdin, J.P. 2013. Operational evapotranspiration mapping using remote sensing and weather datasets: A new parameterization for the SSEB approach. *Journal of the American Water Resources Association* 49, 577–591. doi:10.1111/jawr.12057.

Senay, G.B., Budde, M.E., and Verdin, J.P. 2011. Enhancing the simplified surface energy balance (SSEB) approach for estimating landscape ET: Validation with the METRIC model. *Agricultural Water Management* 98, 606–618.

Shapiro, R. 1987. *A Simple Model for the Calculation of the Flux of Direct and Diffuse Solar Radiation through the Atmosphere*. MA: Hanscom Air Force Base.

Shiklomanov, I.A. 2000. Appraisal and assessment of world water resources. *Water International* 25, 11–32.

Shu, Y., Stisen, S., Jensen, K.H., and Sandholt, I. 2011. Estimation of regional evapotranspiration over the North China Plain using geostationary satellite data. *International Journal of Applied Earth Observation and Geoinformation* 13, 192–206.

Singh, R.K. and Irmak, A. 2009. Estimation of crop coefficients using satellite remote sensing. *Journal of Irrigation and Drainage Engineering* 135, 597–608.

Singh, R.K., Senay, G.B., Velpuri, N.M., Bohms, S., Scott, R.L., and Verdin, J.P. 2013. Actual evapotranspiration (water use) assessment of the Colorado River Basin at the Landsat resolution using the operational simplified surface energy balance model. *Remote Sensing* 6, 233–256.

Sobrino, J.A., Gómez, M., Jiménez-Muñoz, J.C., and Olioso, A. 2007. Application of a simple algorithm to estimate daily evapotranspiration from NOAA–AVHRR images for the Iberian Peninsula. *Remote Sensing of Environment* 110, 139–148.

Sobrino, J.A., Gómez, M., Jiménez-Muñoz, J.C., Olioso, A., and Chehbouni, G. 2005. A simple algorithm to estimate evapotranspiration from DAIS data: Application to the DAISEX campaigns. *Journal of Hydrology* 315, 117–125.

Sobrino, J.A., Jiménez-Muñoz, J.C., Sòria, G., Gómez, M., Ortiz, A.B., Romaguera, M., Zaragoza, M., Julien, Y., Cuenca, J., and Atitar, M. 2008. Thermal remote sensing in the framework of the SEN2FLEX project: Field measurements, airborne data and applications. *International Journal of Remote Sensing* 29, 4961–4991.

Stisen, S., Sandholt, I., Nørgaard, A., Fensholt, R., and Jensen, K.H. 2008. Combining the triangle method with thermal inertia to estimate regional evapotranspiration—Applied to MSG-SEVIRI data in the Senegal River basin. *Remote Sensing of Environment* 112, 1242–1255.

Stone, L.R. and Horton, M.L. 1974. Estimating evapotranspiration using canopy temperatures: Field evaluation. *Agronomy Journal* 66, 450–454.

Su, H., McCabe, M.F., Wood, E.F., Su, Z., and Prueger, J.H. 2005. Modeling evapotranspiration during SMACEX: Comparing two approaches for local- and regional-scale prediction. *Journal of Hydrometeorology* 6, 910–922.

Su, Z. 2002. The surface energy balance system (SEBS) for estimation of turbulent heat fluxes. *Hydrology and Earth System Sciences Discussions* 6, 85–100.

Sun, Z., Wang, Q., Matsushita, B., Fukushima, T., Ouyang, Z., and Watanabe, M. 2009. Development of a simple remote sensing evapotranspiration model (Sim-ReSET): Algorithm and model test. *Journal of Hydrology* 376, 476–485.

Swinbank, W.C. 1951. The measurement of vertical transfer of heat and water vapor by eddies in the lower atmosphere. *Journal of Meteorology* 8, 135–145.

Tang, B. and Li, Z.-L. 2008. Estimation of instantaneous net surface longwave radiation from MODIS cloud-free data. *Remote Sensing of Environment* 112, 3482–3492.

Tang, R., Li, Z.-L., and Tang, B. 2010. An application of the Ts-VI triangle method with enhanced edges determination for evapotranspiration estimation from MODIS data in arid and semi-arid regions: Implementation and validation. *Remote Sensing of Environment* 114, 540–551.

Teixeira, A.H. de C., Bastiaanssen, W.G.M., Ahmad, M.D., and Bos, M.G. 2009. Reviewing SEBAL input parameters for assessing evapotranspiration and water productivity for the Low-Middle São Francisco River basin, Brazil: Part A: Calibration and validation. *Agricultural and Forest Meteorology* 149, 462–476.

Timmermans, W.J., Kustas, W.P., Anderson, M.C., and French, A.N. 2007. An intercomparison of the surface energy balance algorithm for land (SEBAL) and the two-source energy balance (TSEB) modeling schemes. *Remote Sensing of Environment* 108, 369–384.

Tolk, J.A., Howell, T.A., and Evett, S.R. 2006. Nighttime evapotranspiration from alfalfa and cotton in a semiarid climate. *Agronomy Journal* 98, 730–736.

Townshend, J.R. and Justice, C.O. 1988. Selecting the spatial resolution of satellite sensors required for global monitoring of land transformations. *International Journal of Remote Sensing* 9, 187–236. doi:10.1080/01431168808954847.

Trout, T.J., Johnson, L.F., and Gartung, J. 2008. Remote sensing of canopy cover in horticultural crops. *Hortscience* 43, 333–337.

Twine, T.E., Kustas, W.P., Norman, J.M., Cook, D.R., Houser, Pr., Meyers, T.P., Prueger, J.H., Starks, P.J., and Wesely, M.L. 2000. Correcting eddy-covariance flux underestimates over a grassland. *Agricultural and Forest Meteorology* 103, 279–300.

Van de Griend, A.A., Camillo, P.J., and Gurney, R.J. 1985. Discrimination of soil physical parameters, thermal inertia, and soil moisture from diurnal surface temperature fluctuations. *Water Resources Research* 21, 997–1009.

Van Niel, T.G., McVicar, T.R., Roderick, M.L., van Dijk, A.I.J.M., Renzullo, L.J., and van Gorsel, E. 2011. Correcting for systematic error in satellite-derived latent heat flux due to assumptions in temporal scaling: Assessment from flux tower observations. *Journal of Hydrology* 409, 140–148. doi:http://dx.doi.org/10.1016/j.jhydrol.2011.08.011.

Van Oevelen, P.J. 1991. Determination of the available energy for evapotranspiration with remote sensing. *Determination of the Available Energy for Evapotranspiration with Remote Sensing*. the Netherlands: Wageningen University.

Velpuri, N.M., Senay, G.B., Singh, R.K., Bohms, S., and Verdin, J.P. 2013. A comprehensive evaluation of two MODIS evapotranspiration products over the conterminous United States: Using point and gridded FLUXNET and water balance ET. *Remote Sensing of Environment* 139, 35–49. doi:http://dx.doi.org/10.1016/j.rse.2013.07.013.

Venturini, V., Bisht, G., Islam, S., and Jiang, L. 2004. Comparison of evaporative fractions estimated from AVHRR and MODIS sensors over South Florida. *Remote Sensing of Environment* 93, 77–86. doi:http://dx.doi.org/10.1016/j.rse.2004.06.020.

Verma, S.B., Rosenberg, N.J., Blad, B.L., and Baradas, M.W. 1976. Resistance-energy balance method for predicting evapotranspiration: Determination of boundary layer resistance and evaluation of error effects. *Agronomy Journal* 68, 776–782. doi:10.2134/agronj1976.00021962006800050023x.

Vernekar, K.G., Sinha, S., Sadani, L.K., Sivaramakrishnan, S., Parasnis, S.S., Mohan, B., Dharmaraj, S. et al. 2003. An overview of the land surface processes experiment (*Laspex*) over a Semi-Arid Region of India. *Boundary-Layer Meteorology* 106, 561–572.

Verstraeten, W.W., Veroustraete, F., and Feyen, J. 2008. Assessment of evapotranspiration and soil moisture content across different scales of observation. *Sensors* 8, 70–117.

Vinukollu, R.K., Meynadier, R., Sheffield, J., and Wood, E.F. 2011. Multi-model, multi-sensor estimates of global evapotranspiration: climatology, uncertainties and trends. *Hydrological Processes* 25, 3993–4010. doi:10.1002/hyp.8393.

Vinukollu, R.K., Wood, E.F., Ferguson, C.R., and Fisher, J.B. 2011. Global estimates of evapotranspiration for climate studies using multi-sensor remote sensing data: Evaluation of three process-based approaches. *Remote Sensing of Environment* 115, 801–823.

Vorosmarty, C.J., Green, P., Salisbury, J., and Lammers, R.B. 2000. Global water resources: vulnerability from climate change and population growth. *Science* 289, 284–288. doi:10.1126/science.289.5477.284.

Wang, K., Li, Z., and Cribb, M. 2006. Estimation of evaporative fraction from a combination of day and night land surface temperatures and NDVI: A new method to determine the Priestley–Taylor parameter. *Remote Sensing of Environment* 102, 293–305.

Wever, L.A., Flanagan, L.B., and Carlson, P.J. 2002. Seasonal and interannual variation in evapotranspiration, energy balance and surface conductance in a northern temperate grassland. *Agricultural and Forest Meteorology* 112, 31–49.

Wilson, K.B., Hanson, P.J., Mulholland, P.J., Baldocchi, D.D., and Wullschleger, S.D. 2001. A comparison of methods for determining forest evapotranspiration and its components: sap-flow, soil water budget, eddy covariance and catchment water balance. *Agricultural and Forest Meteorology* 106, 153–168.

Yilmaz, M.T., Anderson, M.C., Zaitchik, B., Hain, C.R., Crow, W.T., Ozdogan, M., Chun, J.A., and Evans, J. 2014. Comparison of prognostic and diagnostic surface flux modeling approaches over the Nile River basin. *Water Resources Research* 50, 386–408. doi:10.1002/2013WR014194.

Zahira, S., Abderrahmane, H., Mederbal, K., and Frederic, D. 2009. Mapping latent heat flux in the western forest covered regions of Algeria using remote sensing data and a spatialized model. *Remote Sensing* 1, 795–817.

Zhang, Y., Liu, C., Lei, Y., Tang, Y., Yu, Q., Shen, Y., and Sun, H. 2006. An integrated algorithm for estimating regional latent heat flux and daily evapotranspiration. *International Journal of Remote Sensing* 27, 129–152.

Author Queries

[AQ1] All occurrences of "Net difference vegetation index" has been changed to "Normalized difference vegetation index" for consistency. Please check.

[AQ2] Please provide expansion for the acronym "MODIS."

[AQ3] Please provide complete details for website provided in this chapter.

[AQ4] The Section 3.2.3.1.1 has not been given in this chapter. Please provide appropriate section cross reference.

[AQ5] Please provide part label caption for Figure 3.5.

[AQ6] Reference Petropoulos (2009) is cited in the text but not provided in the reference list. Please check for correctness.

[AQ7] Reference Nishida et al. (2003a,b) is cited in the text but not provided in the list. Please check for correctness.

[AQ8] Please check the inserted closing parenthesis in Equation 3.3.

[AQ9] Reference Glenn, Morino et al. (2008) has been changed to Glenn et al. (2008b) as per the list. Please check for correctness.

[AQ10] Reference Glenn, Huete et al. (2008) has been changed to Glenn et al. (2008a) as per list. Please check for correctness.

[AQ11] Please update the reference Bosilovich (2008).

[AQ12] Please provide in text citation for reference Glenn, Nagler et al. (2013).

[AQ13] Please provide complete detail for references Morse et al. (2000) and Mu (2013).

[AQ14] Please provide in text citation for reference Nishida (2003).

[AQ15] Please provide conference location for reference Petropoulos et al. (2010).